Three dimensional X-ray Bragg ptychography of an extended semiconductor heterostructure

Anastasios I. Pateras

AIX–MARSEILLE UNIVERSITY

INSTITUT FRESNEL

KARLSRUHE INSTITUTE OF TECHNOLOGY

ANGSTRÖMQUELLE KARLSRUHE

PhD thesis

submitted in fulfilment of the requirements for the degree of
Docteur des Sciences, d'Aix-Marseille Université
and
Doktorand der Fakultät für Physik

PhD School: ED352 Physics and Sciences of Matter
Specialities: Optics, Photonics and Image processing

Anastasios Pateras

Three dimensional X-ray Bragg ptychography of an extended semiconductor heterostructure

Defended on the 7th of December 2015 in the presence of the PhD committee:

Anders Madsen
Professor at the European XFEL, Hamburg, Germany Member (President)
Sylvain Ravy
Directeur de Recherche CNRS, Université Paris-Sud, Paris, France (Reviewer)
Marc Verdier
Directeur de Recherche CNRS, SIMAP, Grenoble, France (Reviewer)
Tilo Baumbach
Professor Dr. at ANKA-KIT, Karlsruhe, Germany (PhD advisor)
Marc Allain
Maître des Conférences, Fresnel Institute, Marseille, France (PhD advisor)
Virginie Chamard
Chargé de Recherche CNRS, Fresnel Institute, Marseille, France (PhD advisor)

This document was typeset using LaTeX.

Contents

Abstract

Ptychography is a coherent diffraction imaging technique which aims in retrieving the lost phase from intensity-only far-field measurements. The possibility of solving the phase problem relies on the acquisition of redundant information from successive, partially overlapping illumination areas. During the past ten years, there has been a growing interest in X-ray ptychographic imaging, where lenses with typical numerical apertures in the order of 10^{-2} cannot provide a resolved image of the sample. The versatility of the approach has proved an important asset for 3D mapping of different physical quantities, like the electron density of micrometer-sized specimens with resolution in the 10 - 100nm range.

In the case of periodic crystals, ptychography performed in Bragg geometry is expected to reveal the inner structure of specimens which show interest for microelectronics applications and telecommunications. More specifically, the displacement field of periodic crystals is obtained from the 3D intensity distribution acquired in the vicinity of a Bragg peak with sub-beam resolution.

In this work, we explored the possibility to push further the current limits of 3D Bragg ptychography, by addressing the case of an extended InP/InGaAs nanostructured thin film, bonded on a silicon wafer. The experiment was performed at the ID13 beamline at ESRF, with a monochromatic beam focused down to 100nm. 2D intensity patterns were acquired at several incidence angles in the vicinity of the InP (004) Bragg peak, stacking up a three dimensional dataset. Numerical analysis of the given problem was performed beforehand in order to optimize the inversion strategy and study the possibility of introducing additional physical constraints through regularization approaches. Inversions of the dataset were done using a ptychographical gradient-based optimization phase retrieval algorithm.

The developed strategy was applied on the experimental data which led to the retrieval of a complex-valued 3D image. The result exhibits the high crystallinity quality of the sample with the expected values of thickness and lattice mismatch, nevertheless, small local lattice tilts have been observed - in the order of 0.02°- and confirmed by numerical modeling. This result demonstrates the high sensitivity of the technique, as well as its exciting perspectives for imaging complex organic and inorganic nanostructured materials.

Résumé

La ptychographie est une technique d'imagerie par diffraction cohérente qui vise à récupérer la phase perdue, uniquement par des mesures d'intensité en champ lointain. La possibilité de récupérer la phase est basé sur l'acquisition d'information redondant par des regions successives illuminées qui se recouvrent partiellement. Au cours des dix dernières années, il y a eu un intérêt croissant pour l'imagerie ptychographique. Surtout pour les rayons X ou les lentilles présentent des ouvertures numériques de l'ordre de 10^{-2} et ne peuvent pas fournir une image résolue de l'echantillon. La polyvalence de l'approche est prouvé un atout important pour la cartographie 3D de différentes quantités physiques, comme la densité électronique d'un échantillon micrometrique avec une resolution entre 10 et 100nm.

Dans le cas des cristaux périodiques, la ptychographie réalisée en géométrie de Bragg est capable de révéler la structure interne des échantillons notamment intérêssants pour des applications de la microélectronique et des télécommunications. Cette technique permet l'imagerie des champs de deformation dans des cristeaux périodiques avec des résolutions sous-faisceau.

Dans ce travail, la ptychographie de Bragg en 3D est utilisée pour étudier les propriétés d'une couche crystalline nanostructurée de InP/InGaAs collé sur un substrat de silicium. L'expérience a été réalisée sur la ligne ID13 de l'ESRF, avec un faisceau monochromatique concentré à 100nm. Les intensités 2D ont été acquises avec plusieurs angles d'incidence dans le voisinage du pic de Bragg InP (004), empilant un jeu de données tridimensionnel. L'analyse numérique du problème donné a été effectuée à l'avance afin d'optimiser la stratégie d'inversion et d'étudier la possibilité d'introduire des contraintes physiques supplémentaires basé sur des approches de régularisation. L'inversion de l'ensemble des données a été effectuée en utilisant un algorithm ptychographique de reconstruction de phase.

L'image 3D récupéré représente la haute qualité cristalline de l'échantillon, avec les valeurs de l'épaisseur et du désaccord de maille attendues en moyenne. Néanmoins, de petites inclinaisons locales de maille ont été observées - de l'ordre de 0.02°- et confirmées par modélisation numérique. Les résultats démontrent la sensibilité de la technique, ainsi que ses perspectives passionnantes pour l'imagerie des matériaux organiques et inorganiques nanostructurés complexes.

List of Figures

Acknowledgements

First of all I would like to thank my main supervisors in Marseille, Virginie Chamard and Marc Allain, for their constant support and for all the precious time they have spent working with me. They have always asked the right questions which allowed me to advance in my work, and their guidance has been invaluable during my entire doctoral journey.

I would also like to thank my second supervisor, prof. Tilo Baumbach, for his positive and constructive criticism toward my work during my stay in Karlsruhe. Our discussions have been very stimulating for the fulfillment of this work.

I would like to acknowledge Pierre Godard for his important contribution to my initiation in the field of 3D Bragg ptychography. His experience in the field was very precious to me, and the fact that we shared the office for more than a year led to an important exchange of scientific knowledge and many constructive conversations.

I'm particularly grateful to Manfred Burghammer for all the support he provided during the experiments at the ID13 beamline of the ESRF. His devotion to science and constant user support is something that I couldn't let pass unnoticed. His positive energy and humorous temperament - he diagnosed me with "synchrotron allergy" - have been really encouraging during the experiments.

I wouldn't forget Ludovic Largeau, Anne Talneau, Gilles Patriarche and Konstantinos Pantzas from LPN. The time I spent with them in Marcoussis was particularly productive. Interacting with them was inspiring and especially helpful for the evaluation and understanding of the experimental results.

For the unforgettable games, the excellent teamwork and the artistic culture in the football fields, I would like to thank Simon Labouesse and Alberto Lombardini. The games we played during the last months of my stay in Marseille were particularly refreshing for the spirit.

For their moral support, priceless discussions and the great time we had - and will continue having in the future - I thank my good friends Hilton De Aguiar, Thomas Cornelius, Stephan Hruszkewycz and Wiktor Walasik.

Most of all, I would like to thank my parents for all the years of support. My father for the happy childhood memories. My mother, for making the difficult times look easy.

This work has been supported by the European Commission through the Erasmus Mundus Joint Doctorate Programme Europhotonics (Grant No. 159224-1-2009-1-FR-ERA MUNDUS-EMJD).

Chapter 1

Introduction

Knowledge of the materials structure and composition at the nanoscale is essential for understanding their physical, chemical, or electronic properties. Being able of manipulating these properties holds an immense interest in modern microelectronics and telecommunication applications. For example, adjusting the strain levels of III-V semiconductor layers bonded on silicon, can lead to the precise design of the energy band structure of photo-emitting diodes [2]. Thus, measurement and visualization of strain fields inside such devices is of great importance for nanoelectronics [3].

The need of visualizing strain or defects inside crystal nanostructures, has led to the development of different microscopy techniques based on the diffraction of periodic objects by electrons or X-rays for decades [4, 5, 6, 7]. In the past few years, lensless Coherent Diffraction Imaging (CDI) techniques like ptychography have gained in popularity thanks to their comparative advantages with respect to other approaches, like their sensitivity to density contrast, unprecedented spatial resolutions even for radiation sensitive biological specimen [8], extended field of view (especially valid for ptychography) and their non-invasive nature - *e. g.* TEM demands sample thinning.

Nevertheless, lensless X-ray strain microscopy remains a challenging technique to probe matter at the nanoscale, and although that everyday more synchrotron sources are acquiring the capacity to perform, it hasn't yet become a routinely applied imaging technique. In this scope, this work is concentrated on the application of 3D X-ray Bragg ptychography for the characterization of an InP/InGaAs semiconducting layer, used for the design of integrated devices emitting at the $1.55\mu m$ wavelength domain [9].

In this chapter, we will briefly discuss the general principles of Bragg CDI, starting from the elemental phenomena that occur when X-rays interact with periodic objects - at wavelengths comparable to the interatomic distances as dictated by the Bragg law - and form peaks of constructive interference (Bragg peaks). We will see the basic concepts in reconstructing the lost phase from intensity-only measurements using a Phase Retrieval Algorithm (PRA) and close with a summary of the milestones achieved by CDI during the past fifteen years.

1.1 From XRD to Bragg CDI

1.1.1 X-ray Bragg diffraction

The principle effects occurring when X-ray radiation interacts with matter are *absorption* and *scattering*. The probability (cross-section) that a photon is absorbed by a material becomes important when the photon energy is equivalent to the quantum energy of an electronic transition (resonance scattering). When the photon energy approaches or exceeds the ionization threshold, absorption maximizes (absorption edge) and we have the photoelectric effect. X-ray scattering

happens when photons hit electrons and change their velocity while conserving their kinetic energy (elastic or Thompson scattering) or not (inelastic or Compton scattering). We are interested only in the elastic scattering of X-rays, since that is responsible for the constructive interference of the scattered X-rays and formation of bright spots in the far-field, known as Bragg peaks. The atomic level structure of the material can then be determined by analyzing the Bragg peaks.[1]

There are different models that describe the relationship between the Bragg peak and the materials structure, the first and simplest proposed by the Braggs in 1913 is called the Bragg's Law. For a crystalline solid, the incident at angle θ X-rays are scattered from lattice planes which are separated by the interplanar distance d [See d-spacing in Fig. 1.1a]. When the scattered rays interfere constructively, they remain in phase since the path-length-difference ($\mathcal{PLD}$) is equal to an integer multiple of the wavelength λ, which leads to the next formula:

$$2d \sin\theta = n\lambda \tag{1.1.1}$$

The d-spacing that one can measure using Bragg's law is related to the lattice parameter α of a particular crystallographic system (Bravais lattice) according to specific formulas [10]. For the simple cubic system is given by

$$\frac{1}{d^2} = \frac{1}{d_{hk\ell}^2} = \frac{h^2 + k^2 + \ell^2}{\alpha^2} \tag{1.1.2}$$

where $(hk\ell)$ are the Miller indices that define the crystallographic planes. The (001) direction of Figure 1.1b for example, is corresponding to all the perpendicular to that direction planes and the (110) is shown with gray. There are 14 different crystal systems in three-dimensional space known as Bravais lattices, so one has to know the crystallographic group of the material in order to relate the distance of two lattice points with its real lattice parameter α. The importance of all that knowledge has to do with the fact that through Bragg diffraction one can finally measure the displacement and ultimately the strain inside crystals.

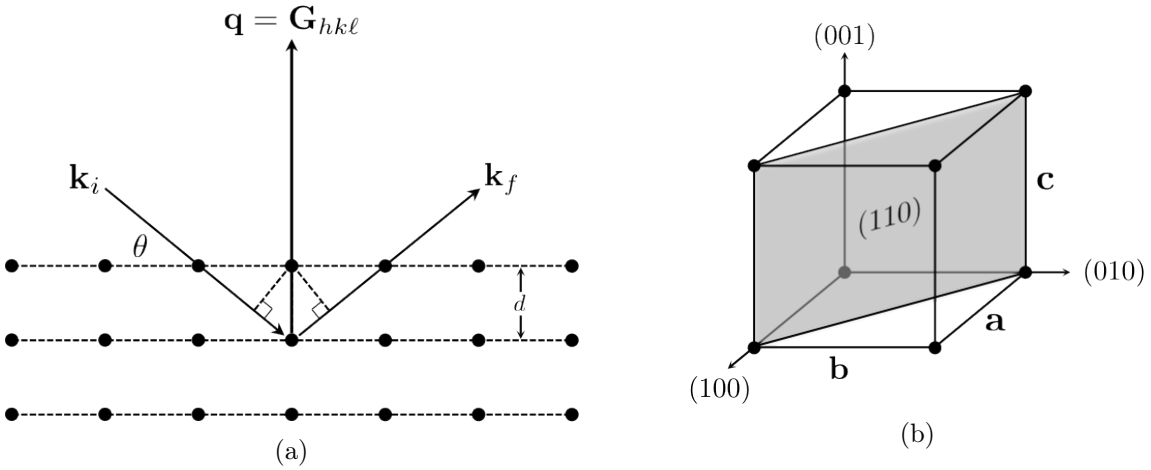

Figure 1.1: (a) X-rays interacting with a crystal lattice at Bragg condition. Scattering only from the (001) planes. (b) Graphical representation of the (110) crystallographic planes in a cubic crystal.

[1] Diffraction can also be perceived using the wave-like nature of light. Since X-rays have wavelengths which are comparable to the inter-atomic distances they will give rise to diffraction phenomena. When passing through a crystal they will force the electronic cloud of atoms to vibrate with their frequency and according to Maxwell's equations, the accelerating electrons located in the vicinity of atoms act as scatterers, re-emitting spherical waves of radiation that finally interfere in the far-field. There are also other effects of secondary radiation emission like *fluorescence* which happens in the ionized atoms when electrons re-occupy empty orbitals and *Auger* electrons.

Macroscopically, strain (ϵ) can be expressed for an elemental volume under various stresses σ_{ij} as schematically shown on Fig. 1.2. The axial strain is directly proportional to the applied stress in the elastic deformation area of the medium as described by *Hooke's law* and can also be calculated from the change in the length of the volume along the direction of the applied stress ($\delta\ell_{zz}$) [11]. If we take the direction of σ_{zz} for example, the strain component will be:

$$\epsilon_{zz} = \frac{\sigma_{zz}}{E} = \frac{\ell_{zz} - \ell^0_{zz}}{\ell^0_{zz}} = \frac{\delta\ell_{zz}}{\ell^0_{zz}} = \frac{u_{zz}}{\ell^0_{zz}} \tag{1.1.3}$$

where ℓ_{zz} is the length of the volume in the given direction under applied stress, ℓ^0_{zz} the physical length of the volume when no external loads are applied and u_{zz} the displacement. Having all

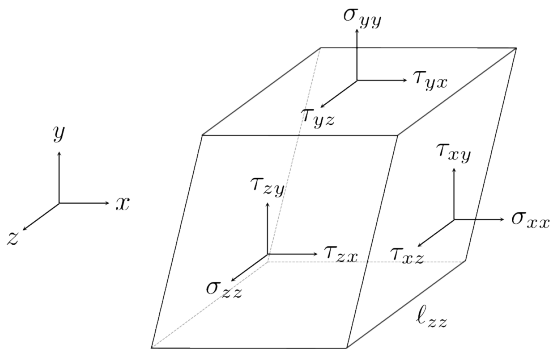

Figure 1.2: General state of stress.

three orthogonal components of the three-dimensional displacement vector $\mathbf{u}$ one can construct the generalized tensor which contains the axial ($i = j$) and shearing ($i \neq j$) strain components (ϵ_{ij}) given by the following formula [12]:

$$\epsilon_{ij} = \frac{1}{2}\left(\frac{\partial u_j}{\partial i} + \frac{\partial u_i}{\partial j}\right), \quad \text{where } i,j = x,y,z, \quad \Rightarrow \quad \epsilon_{ij} = \begin{pmatrix} \epsilon_{xx} & \epsilon_{xy} & \epsilon_{xz} \\ \epsilon_{yx} & \epsilon_{yy} & \epsilon_{yz} \\ \epsilon_{zx} & \epsilon_{zy} & \epsilon_{zz} \end{pmatrix} \tag{1.1.4}$$

Similarly to the macroscopic definition of strain we can define the deformation inside a periodic crystal, and as we can see, from the knowledge of $\mathbf{u}$ one can access the relevant parameters for the characterization of the sample mechanical behavior under stress. In the case of crystalline structures, atoms are distributed in a periodic lattice described by a vector basis $(\mathbf{a}, \mathbf{b}, \mathbf{c})$ which is able to reproduce the entity of the crystal structure starting from the unit cell. If $\mathbf{r'_n}$ is the position vector of an atom in the deformed lattice, then crystal strain can be seen as the relative displacement amount of each atom with respect to its expected position in the perfect lattice.

$$\mathbf{u} = \mathbf{r'_n} - \mathbf{r_n} = \mathbf{r'_n} - (n_1\mathbf{a} + n_2\mathbf{b} + n_3\mathbf{c}) \tag{1.1.5}$$

The way the crystal displacement is measured, is usually described using the diffraction vector $\mathbf{q} = \mathbf{k}_f - \mathbf{k}_i$, which at Bragg condition corresponds to probing only one set of $(hk\ell)$ planes ($\mathbf{q} = \mathbf{G}_{hk\ell}$), with $\mathbf{k}_i$ the incident wave propagation vector, λ its wavelength and $\mathbf{k}_f$ the scattered wave propagation vector and $|\mathbf{k}_i| = |\mathbf{k}_f| = 2\pi/\lambda$. The schematic representation of Fig. 1.1a, describes the geometry of a Bragg diffraction experiment.

With traditional X-ray diffraction (XRD) techniques ($\theta - 2\theta$ scan, rocking curve [13]) one can obtain the average value of the lattice displacement in an area of the crystal defined by the size of the beam. But in order to obtain the spatially dependent strain field in direct space - the entire information about the atomic arrangements as a function of the three-dimensional space - other approaches are needed.

1.1.2 Coherent X-ray Bragg diffraction imaging

The technological advent of microelectronics and nano-engineering necessitated over the years the development of new characterization techniques, whose materialization became feasible with the advent of highly *brilliant* and *coherent* third generation synchrotron sources. Now the needs of modern nanotechnology for manufacturing materials with specific characteristics (*e.g.* tailoring the structure of electronic energy bands for semiconducting photo-emission diodes and optical amplifiers [14]) have driven the development of non-destructive, quantitative, three-dimensional XRD imaging techniques. In this section, we will develop the main principles of CDI which was first demonstrated in non-periodic objects [15] and later for crystals [16] (Bragg CDI).

As briefly discussed in the previous section, when a crystal is illuminated by X-rays in Bragg condition - at a specific incident θ angle which can be calculated by Eqns.(1.1.1) and (1.1.2) - a Bragg peak is formed in the far-field. The logical question that arises here, is how can we make use of the measured intensity information of the Bragg peak in reciprocal space (RC) to reconstruct the image of the object in direct space (DS)?

Let $\rho(\mathbf{r})$ be the complex-valued *object function* that describes the crystal, known as the *crystal electron density* [17]. For an unstrained crystal, the atomic arrangement is periodic, thus the electron density can be expressed as a discrete summation of Dirac δ functions

$$\rho(\mathbf{r}) = s(\mathbf{r}) \sum_{n=1}^{N} \delta(\mathbf{r} - \mathbf{r_n}) \tag{1.1.6}$$

where $s(\mathbf{r})$ is a binary function that describes the volume occupied by the N cells of the crystal [18]. For a strained crystal, if we consider Eqn.(1.1.5) the density becomes

$$\rho'(\mathbf{r}) = s(\mathbf{r}) \sum_{n=1}^{N} \delta(\mathbf{r} - \mathbf{r_n} - \mathbf{u}(\mathbf{r_n})) \tag{1.1.7}$$

which assumes that the shape of the crystal $s(\mathbf{r})$ is not affected by the displacements. In the kinematical limit and under the *Born approximation*, the scattered *exit-field* $\psi(\mathbf{r})$ is the product of the object function times the incident beam $p(\mathbf{r})$, which in the case of Bragg CDI is considered to be a plane wave, thus $p(\mathbf{r}) = 1$. In a distance adequately far from the object where a photon detector is placed, in the frame of Fraunhofer diffraction, the scattered far-field from a strained crystal can be written as the *Fourier transform* of the exit-field.

$$\Psi(\mathbf{q}) = \int_{-\infty}^{+\infty} \rho'(\mathbf{r}) e^{i\mathbf{qr}} d\mathbf{r} = \int_{-\infty}^{+\infty} s(\mathbf{r}) \sum_{n=1}^{N} \delta(\mathbf{r} - \mathbf{r_n} - \mathbf{u}(\mathbf{r_n})) e^{i\mathbf{qr}} d\mathbf{r}$$

Having in mind the *sifting* (or *sampling*) property of the Delta function $\int_{-\infty}^{+\infty} f(\mathbf{r})\delta(\mathbf{r} - \mathbf{r_n})d\mathbf{r} = f(\mathbf{r_n})$ for every f continuous at $\mathbf{r} = \mathbf{r_n}$, we can write

$$\Rightarrow \quad \Psi(\mathbf{q}) = \sum_{n=1}^{N} s(\mathbf{r_n} + \mathbf{u}(\mathbf{r_n}))\ e^{i\mathbf{q}(\mathbf{r_n} + \mathbf{u}(\mathbf{r_n}))} \tag{1.1.8}$$

If we additionally consider the exploration of the RS in the vicinity of the Bragg peak as $\mathbf{q} = \mathbf{G}_{hk\ell} + \mathbf{q}'$ with $\mathbf{q}'$ so small that $\mathbf{q}'\mathbf{u}(\mathbf{r_n}) \approx 0$, while $\mathbf{G}_{hk\ell}\mathbf{r_n} = n \times 2\pi$ we have

$$\begin{aligned}
\Psi(\mathbf{q}') &= \sum_{n=1}^{N} s(\mathbf{r_n} + \mathbf{u}(\mathbf{r_n}))\ e^{i(\mathbf{G}_{hk\ell}+\mathbf{q}')(\mathbf{r_n}+\mathbf{u}(\mathbf{r_n}))} \\
&= \sum_{n=1}^{N} s(\mathbf{r_n} + \mathbf{u}(\mathbf{r_n}))\ e^{i[\cancelto{2\pi}{\mathbf{G}_{hk\ell}\mathbf{r_n}}+\mathbf{G}_{hk\ell}\mathbf{u}(\mathbf{r_n})+\mathbf{q}'\mathbf{r_n}+\cancelto{0}{\mathbf{q}'\mathbf{u}(\mathbf{r_n})}]} \\
&= \sum_{n=1}^{N} s(\mathbf{r_n} + \mathbf{u}(\mathbf{r_n}))\ e^{i\mathbf{G}_{hk\ell}\mathbf{u}(\mathbf{r_n})}\ e^{i\mathbf{q}'\mathbf{r_n}}
\end{aligned} \tag{1.1.9}$$

Thus, the expected photon counts on a diffraction pattern are given by the square modulus of the far-field $\Psi(\mathbf{q}')$, related with the *effective electron density* $\rho_L(\mathbf{r}) = |\rho(\mathbf{r})|\ e^{i\mathbf{G}_{hk\ell}\mathbf{u}(\mathbf{r_n})}$ by

$$I(\mathbf{q}') = |\Psi(\mathbf{q}')|^2 \equiv |\mathcal{F}\{|\rho(\mathbf{r})|\ e^{i\mathbf{G}_{hk\ell}\mathbf{u}(\mathbf{r_n})}\}|^2 \tag{1.1.10}$$

As the previous formula suggests, since *only* magnitudes are available from the diffraction experiment, the phase components of $\Psi(\mathbf{q}')$ and in particular the information of the strain which is contained in the first phase component of Eqn.(1.1.9) as the displacement projection $\mathbf{u}(\mathbf{r_n})$ on the scattering vector $\mathbf{G}_{hk\ell}$ cannot be recovered. This pathological problem can be expressed mathematically by Eqn.(1.1.10), and it is known as the *phase problem* [19].

Unfortunately there's no analytical solution to the phase problem, but thanks to a series of revolutionary ideas published from 1952 to 1972 by D. Sayre [20], W. Hoppe [21], Gerchberg and Saxton [1], it has been shown that the lost phase components of the scattered illumination are encoded in the diffraction pattern and can be retrieved numerically using iterative phase-retrieval algorithms that include the application of a constraint in the object size (*support constraint*), if the scattering process is coherent [See Appendix A] and if sampling the diffracted signal with at least twice the *Nyquist frequency*, so that the *Shannon theorem* is satisfied [20, 22].

In the case of coherent scattering, the numerical approaches that have been developed, are based in the idea of reconstructing the original complex function $\rho(\mathbf{r})$ by fitting the measured intensity pattern, according to the model we have described above [23]. One of the proposed algorithms is presented in Fig. 1.3. An initial estimate of $\rho(\mathbf{r})$, namely $g_0(\mathbf{r})$ is given as input to

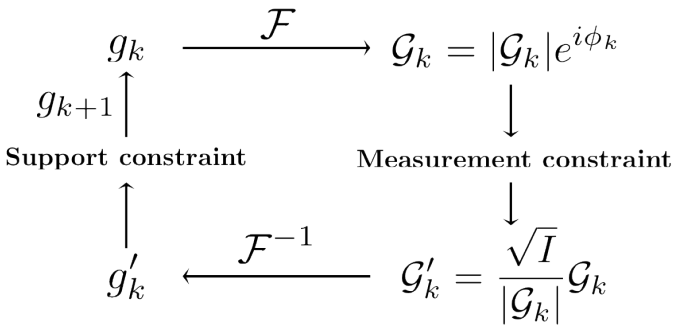

Figure 1.3: Schematic of the Gerchberg-Saxton algorithm [1].

the algorithm, which calculates its Fourier transform $\mathcal{G}_0(\mathbf{q})$. Then, after replacing the amplitude of $\mathcal{G}_0(\mathbf{q})$ with the square root of the measured intensity ($\sqrt{I}$), the inverse Fourier transform will give a new estimate, namely $g'_1(\mathbf{r})$, which after the application of the support constraint will give $g_1(\mathbf{r})$. After k iterations, the updated $g_k(\mathbf{r})$ is expected to converge to $\rho(\mathbf{r})$. The process was first described and numerically demonstrated by Gerchberg and Saxton in 1972 [1], and since then has been significantly improved and extended by J. Fienup [24].

Phase retrieval algorithms first appeared in studying non-periodic micrometer-sized specimen using synchrotron radiation in 1999, when demonstrated experimentally by Miao et *al.* [15] in two dimensions. In 2002, the first 3D experimental reconstruction was obtained with a 50nm resolution [25], and it was based on the tomographic approach. [See Subsection 2.2.2 for more information]

In Bragg geometry, the procedure for accessing the three-dimensional information of a crystal is based on acquiring several diffraction patterns at different incident angles in the vicinity of a Bragg reflection [17], allowing multiple slices to be obtained. The entire stack of the two-dimensional acquisitions is then inverted with an iterative algorithm based on the use of the 3D inverse Fourier transform. The measured stack of data forms the RS constraining information for the algorithm, and by knowing the dimensions of the DS object, a good initial estimate can be constructed.

In 2001, CDI was demonstrated in Bragg geometry, on Au nanocrystals in 2D [16] and two more years later in 3D [17]. In each case, only the amplitude of the electron density was evaluated, with no clear notion about the retrieved phase profile and thus, the displacement field. In 2006, one deformation component of a Pb nanocrystal is successfully reconstructed for the first time in three dimensions [26], and in 2010 the full strain tensor of a ZnO nanorod is reconstructed by measuring diffraction patterns of six different Bragg reflections [12].

Other remarkable results have been the 3D reconstruction of strain evolution in a single crystal under applied pressures up to 6.4GPa [27] with 30nm resolution, and the *in-situ* strain evolution of a single $LiNi_{0.5}Mn_{1.5}O_4$ nanoparticle in a coin cell battery during charge/discharge cycles [28]. Finally, the reconstruction of displacement fields induced by coherent lattice vibrations (phonons) of a single Au nanocrystal in three dimensions by X-ray free-electron laser pulses [29], has been maybe one of the most impressive accomplishments of Bragg CDI until today. An optical laser was used as a pump of the sample, generating the phonons, while the X-ray pulses were illuminating the nanocrystal and diffraction pattens were recorded.

One of the first limitations of CDI though, is the fact that it restricts the size of the object. For an extended sample CDI becomes inadequate, and for the study of nanocrystals, focused beams have to be used in order to obtain an exploitable signal (patterns with a sufficient number of measured photons). In addition to that, very strong strain fields usually cannot be resolved by the PRA due to stagnation issues [23]. In several attempts *tight* constraints on the retrieved phase profile are imposed [30, 31, 32], but even then, the presence of local minima lead to ambiguous solutions [33]. In order to overcome the above limitations, coherent X-ray Bragg ptychography has been proposed.

Chapter 2

3D Bragg ptychography

Contents

As it was previously discussed, CDI for non-periodic and periodic objects that emerged during the past fifteen years thanks to the technological progress of third generation coherent light sources, the evolution of microelectronics and the implementation of the fast Fourier transform (FFT) algorithm for the computation of the discrete Fourier transform (DFT) which considerably accelerated the speed of numerical calculations[1], provided solutions to many nanoscience imaging problems [35, 36]. Though, the restrictions that CDI posed to the sample size, to the complexity of the crystal deformation fields and the ultimate achievable resolution, requested the development of new approaches.

The new technique that was used in order to overcome the previous limitations, named *ptychography*, was based on scanning an extended sample with a much smaller illumination at different, but overlapping areas and collecting the far-field diffraction patterns [37]. The ensemble of the individual intensity patterns is going to contain redundant information, which is considered as the key-point for successfully retrieving the lost phase components of the scattered field [38]. This new approach allows increasing the field of view and investigating objects that are much larger than the beam size. Especially in the case of periodic objects, the redundant information in *Bragg ptychography* could allow the study of highly-complex strain fields which were not possible to retrieve with the CDI approach.

In this chapter, we will develop the analytical formalism of Bragg ptychography. We will start with the *ideal* case of studying a 2D object and see the forward-problem model and the discretization process for obtaining its numerical solution using two different classes of PRAs. We

[1] In 1994, Gilbert Strang described the fast Fourier transform as "the most important numerical algorithm of our lifetime." [34]

will describe some of the main concepts of modeling and reconstructing objects (with aperiodic and periodic structures) with 3D ptychographic imaging approaches and discuss in short their most recent progress, especially for the measurement of three-dimensional crystal strain fields, along with their current experimental limitations and future perspectives.

2.1 Principles of 2D ptychographic imaging

2.1.1 Direct problem modeling and numerical discretization

In the case of an amorphous, infinitely thin specimen, we can see the geometry of the experiment on Figure 2.1b. The sample is illuminated in transmission and the detector is located downstream the sample. On Fig.2.1a, the dashed circles represent the illuminated regions of the sample (a Fresnel zone plate) that are illuminated by the beam. For one given position of the scan, we can see the detected far-field intensity pattern when using a completely homogeneous circular beam.

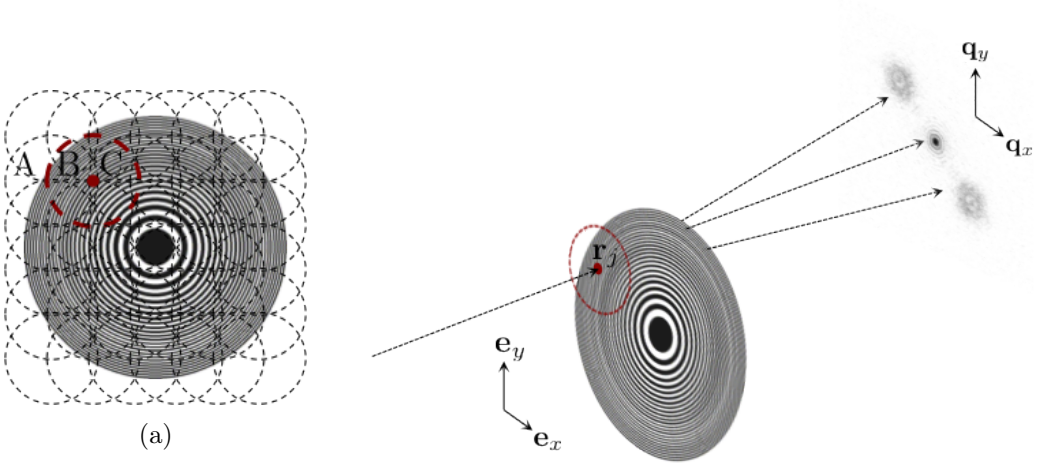

Figure 2.1: (a) The beam imprints on the FZP at every position of the ptychography scan. (b) Transmission geometry X-ray imaging experiment of a two-dimensional FZP. We can see the far-field intensity pattern for position B of the ptychography scan.

Again, the model that describes the scattering from the object is the same as in CDI, but now the exit-field is also dependent of the probe position vector $\mathbf{r}_j$, since the sample is scanned at multiple positions j. Then the exit-field $\psi_j : \mathbb{R}^2 \to \mathbb{C}$ can be defined as follows:

$$\psi_j(\mathbf{r}) = p(\mathbf{r} - \mathbf{r}_j)\rho(\mathbf{r}) = (p_j\rho)(\mathbf{r}) \tag{2.1.1}$$

where

$$\mathbf{r} = r_x\mathbf{e}_x + r_y\mathbf{e}_y \tag{2.1.2}$$

with $(\mathbf{e}_x, \mathbf{e}_y)$ the DS unitary vectors of the laboratory frame, which can be seen on Fig.2.1b. For the j-th position of the scan, the far-field is the Fourier transform of the exit-field ψ_j and the *expected* intensity $h_j : \mathbb{R}^2 \to \mathbb{R}_+$ at a RS point $\mathbf{q}$ reads

$$h_j(\mathbf{q}) = |\mathcal{F}\psi_j|^2(\mathbf{q}) + b_j(\mathbf{q}) = |\Psi_j(\mathbf{q})|^2 + b_j(\mathbf{q}) \tag{2.1.3}$$

where

$$\mathbf{q} = q_x\mathbf{q}_x + q_y\mathbf{q}_y \tag{2.1.4}$$

with $(\mathbf{q}_x, \mathbf{q}_y)$ the RS orthonormal vectors on the detection plane, which can be also seen on Fig.2.1b. The quantity $b_j(\mathbf{q})$ represents the intensity generated by the *background events* at each of the scan positions $j \leqslant J$. One notes that the far-field of Eqn.(2.1.3) is a function of continuous values, which is going to be measured by a pixel array detector[2] with M_2 rows and M_1 columns. Thus, one has to take into account the discretization of the far-field, as well as of the exit-field and ultimately of the reconstructed object in DS, as we will see later. The discretization of the far-field leads to the construction of the matrix $\mathbf{\Psi}_j \in \mathbb{C}^{M_2 \times M_1}$ which is defined below:

$$\mathbf{\Psi}_j \triangleq \{\Psi_j(m_1\delta q_x, m_2\delta q_y)\} \tag{2.1.5}$$

with $(m_1, m_2) \in \mathbb{Z}^2$ such that $-M_1/2 \leqslant m_1 \leqslant M_1/2 - 1$ and $-M_2/2 \leqslant m_2 \leqslant M_2/2 - 1$ and $(\delta q_x, \delta q_y)$ the discretization step along q_x and q_y respectively. The discretized *expected* intensity on the detector array $\mathbf{h}_j \in \mathbb{N}^{M_2 \times M_1}$ is readily deduced

$$\mathbf{h}_j \triangleq \left\{|\Psi_j(m_1\delta q_x, m_2\delta q_y)|^2 + b_j(m_1\delta q_x, m_2\delta q_y)\right\}. \tag{2.1.6}$$

The link between the above quantity and the object is given by Eqn.(2.1.3), but in order to materialize it in a reconstruction algorithm, the exit-field has to be discretized accordingly. For that reason we introduce a new set of indices (n_x, n_y) that correspond to the DS discretized object and probe [See Fig.2.2b]. For each of the individual scan positions, we also define an area centered around the scan position vector $\mathbf{r}_j$, to which we will refer as the *beam support* $\mathcal{S}_j$.

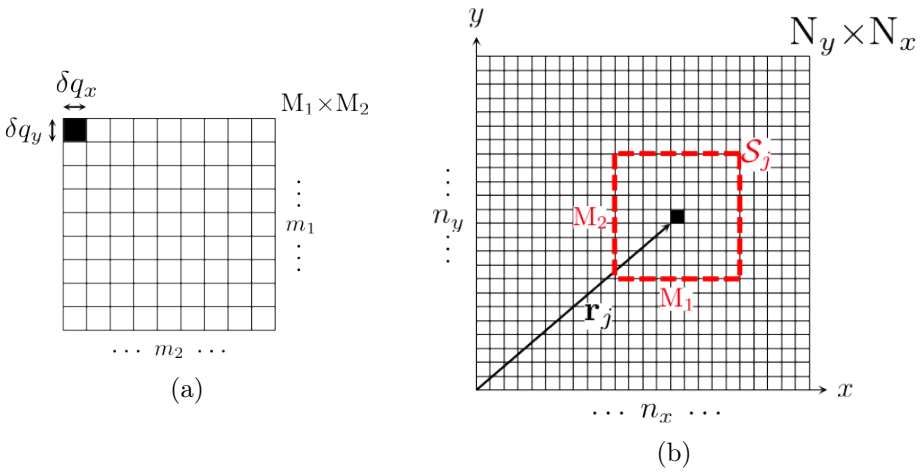

Figure 2.2: Schematic of the problem discretization. (a) The $M_2 \times M_1$ detector pixel array used for the measurement of the RS intensity patterns. (b) Representation of the DS grid where the object is contained. The beam support $\mathcal{S}_j$ can be only defined inside this area, thus $1 \leqslant M_1 \leqslant N_y$ and $1 \leqslant M_2 \leqslant N_x$.

Using the (n_x, n_y) indices we have defined above and the pixel size in DS $(\delta x, \delta y)$, we consider the probe, the object and the exit-field in a *discretized* form as respectively:

$$\mathbf{p}_j \triangleq \{p_j(n_x\delta x, n_y\delta y)\} \in \mathbb{C}^{N_y \times N_x}, \tag{2.1.7}$$

$$\boldsymbol{\rho} \triangleq \{\rho(n_x\delta x, n_y\delta y)\} \in \mathbb{C}^{N_y \times N_x} \tag{2.1.8}$$

and

$$\boldsymbol{\psi}_j \triangleq \{p_j(n_x\delta x, n_y\delta y)\rho(n_x\delta x, n_y\delta y) : (n_y, n_x) \in \mathcal{S}_j\} \in \mathbb{C}^{M_2 \times M_1} \tag{2.1.9}$$

[2]With no loss of generality, we will consider hereafter that the number of pixels (in DS and RS) is an even number.

with $(n_x, n_y) \in \mathbb{Z}^2$ such that[2] $-N_x/2 \leqslant n_x \leqslant N_x/2 - 1$ and $-N_y/2 \leqslant n_y \leqslant N_y/2 - 1$. The final step before going into details about the ptychographic algorithms that we used for the image reconstruction is to define the operation that allows the numerical calculation of the far-field from the exit-field *via* a discrete Fourier transform (DFT):

$$\boldsymbol{\Psi}_j = \mathrm{DFT}_{2\mathrm{D}}(\boldsymbol{\psi}_j). \tag{2.1.10}$$

We note that this equation demands that the sampling between DS and RS satisfies

$$\delta q_x = \frac{1}{M_1\ \delta x} \quad \text{and} \quad \delta q_y = \frac{1}{M_2\ \delta y} \tag{2.1.11}$$

which relate the intensity pattern sampling in RS, defined by the detector pixel dimensions $\delta q_x, \delta q_y$, with their reciprocal quantities $\delta x, \delta y$. On the next subsection, we will see how we proceed to the estimation of the unknown object $\boldsymbol{\rho}$ from a noisy dataset.

2.1.2 Phase-retrieval algorithms for ptychographic datasets

The previous subsection describes the forward modeling, *i.e.* given the object $\boldsymbol{\rho}$, Eqn. (2.1.6) gives the expected intensity on the camera for the jth position. In practice, however, one deals with the *inverse problem* of retrieving the object consistent with the measurement for all the considered positions. Hence, in the following, let $\mathbf{Y}_j \in \mathbb{R}_+^{M_2 \times M_1}$ denote the noisy dataset provided by the camera for the jth position. Then, following standard statistical estimation techniques (See for instance [39, 40]), the object is estimated through the following optimization problem:

$$\widehat{\boldsymbol{\rho}} = \arg\min_{\boldsymbol{\rho}} \mathcal{L}(\boldsymbol{\rho}) \tag{2.1.12}$$

where the fitting function which we will refer to as the *criterion*, reads:

$$\mathcal{L}(\boldsymbol{\rho}) = \sum_j \mathcal{L}_j(\boldsymbol{\rho}) \qquad \text{with} \qquad \mathcal{L}_j(\boldsymbol{\rho}) := \sum_{\mathbf{m}} \left[\mathbf{Y}_{j;\mathbf{m}}^{1/2} - \mathbf{h}_{j;\mathbf{m}}^{1/2}(\boldsymbol{\rho}) \right]^2 \tag{2.1.13}$$

where $\mathbf{h}_{j;\mathbf{m}}$ (resp. $\mathbf{Y}_{j;\mathbf{m}}$) stands for the element with coordinate $\mathbf{m} := (m_1, m_2)$ in the matrix $\mathbf{h}_j$ (resp. $\mathbf{Y}_j$). In Eq. (2.1.13), we made explicit the formal dependency of $\mathbf{h}_{j;\mathbf{m}}$ with respect to the object to retrieve $\boldsymbol{\rho}$. From a practical viewpoint, however, a closed-form expression of a minimizer $\widehat{\boldsymbol{\rho}}$ is not available and the minimization of the criterion $\mathcal{L}$ should be performed by numerical means. Gradient-based algorithms are widely used for this task, in particular because of their relatively low computational burden. As a result, the gradient of Equation (2.1.13) is of interest and reads

$$\partial\mathcal{L}(\boldsymbol{\rho}) = \sum_j \partial\mathcal{L}_j(\boldsymbol{\rho}) \tag{2.1.14}$$

where the gradient associated to the j-th probe is

$$\partial\mathcal{L}_{j;\mathbf{n}}(\boldsymbol{\rho}) = \begin{cases} 2\,\mathbf{p}_{j;\mathbf{n}}^* \times \left[\mathrm{DFT}_{2\mathrm{D}}^{-1} \left(\boldsymbol{\Psi}_j(\boldsymbol{\rho}) - \hat{\boldsymbol{\Psi}}_j(\boldsymbol{\rho}) \right) \right]_{\mathbf{n}} & \forall \mathbf{n} \in \mathcal{S}_j \\ 0 \quad \text{otherwise} \end{cases} \tag{2.1.15}$$

where $[\boldsymbol{A}]_{\mathbf{n}}$ (resp. $\mathbf{p}_{j;\mathbf{n}}$ and $\partial\mathcal{L}_{j;\mathbf{n}}$) stands for the element with coordinate $\mathbf{n} := (n_x, n_y)$ in the matrix $\boldsymbol{A} \in \mathbb{C}^{N_y \times N_x}$ (resp. $\mathbf{p}_{j;\mathbf{n}}$ and $\partial\mathcal{L}_j$), and "$*$" is the complex conjugate. The matrix $\hat{\boldsymbol{\Psi}}_j \in \mathbb{C}^{M_2 \times M_1}$ that appears in this expression is the *corrected* far-field defined by

$$\hat{\boldsymbol{\Psi}}_{j;\boldsymbol{m}} \mathrel{\hat{=}} \boldsymbol{\Psi}_{j;\boldsymbol{m}} \left(\frac{\mathbf{Y}_{j;\boldsymbol{m}}}{\mathbf{h}_{j;\boldsymbol{m}}} \right)^{1/2} \tag{2.1.16}$$

where $\boldsymbol{\Psi}_{j;\mathbf{m}}$ (resp. $\hat{\boldsymbol{\Psi}}_{j;\mathbf{m}}$) stands for the element with coordinate $\mathbf{m} := (m_1, m_2)$ in the matrix $\boldsymbol{\Psi}_j$ (resp. $\hat{\boldsymbol{\Psi}}_j$). Below, we consider two different classes of algorithms, depending on the way the optimization process takes place.

A direct extension of the ptychographical iterative engine

In this first approach, the object is successively updated using the measured intensity pattern from the current position of the ptychography scan. As a result, the algorithm consists in a two loops numerical scheme, one for the positions of the ptychography scan (index j) and one for the number of iterations (index k). More precisely, we consider the following conventions: let $\boldsymbol{\rho}_{0,0} \equiv \boldsymbol{\rho}_0$ with $\boldsymbol{\rho}_0$ the *initial* estimate, $\boldsymbol{\rho}_{k,0} \equiv \boldsymbol{\rho}_{k,J}$ and $\boldsymbol{\rho}_{k,J+1} \equiv \boldsymbol{\rho}_{k+1,1}$. Then, the object updating strategy for $k = 0, 1 \cdots$ is defined by

$$j = 1 \cdots J+1, \qquad \boldsymbol{\rho}_{k,j} = \boldsymbol{\rho}_{k,j-1} - \beta \, (\partial \mathcal{L}_{k,j-1}) \doteq \boldsymbol{\Lambda} \tag{2.1.17}$$

with $\partial \mathcal{L}_{k,j} \hat{=} \partial \mathcal{L}_j(\boldsymbol{\rho}_{k,j})$ and where *e. g.* "$\boldsymbol{A} \doteq \boldsymbol{B}$" stands for the component-wise division of matrix $\boldsymbol{A}$ by matrix $\boldsymbol{B}$. The constant step-length $\beta > 0$ should be adjusted so that the criterion Eq. (2.1.13) decreases to reach a minimum. Finally, the matrix $\boldsymbol{\Lambda}$ is defined by

$$\boldsymbol{\Lambda} = \alpha + \sum_j \left(\boldsymbol{p}_j^* \dot{\times} \ \boldsymbol{p}_j \right) \qquad \alpha > 0 \tag{2.1.18}$$

with "$\dot{\times}$" the component-wise multiplication.

With the gradient expression (2.1.15) in mind, the algorithm Eq. (2.1.17) can be recognized as a direct generalization of the *ptychographical iterative engine* (PIE), the first algorithm to be used for ptychographic imaging [38]. Indeed, the main difference between Eq. (2.1.17) and the standard PIE is the matrix $\boldsymbol{\Lambda}$ that "scales"[3] the gradient so that the convergence rate is homogeneous over the whole object. Without this preconditioning (*i.e.*, with the standard PIE), the areas with the highest photon counts would converge much faster during the inversion process [40].

From an optimization perspective, though, such an iterative scheme can be recognized as an *ordered-subset* (OS) strategy [40]. All the OS iteration share the salient feature that the update stems from a natural *splitting* in the dataset. In the case of the PIE-like iteration (2.1.17), this splitting is dictated by the spatial positioning of the probe function. These strategies usually converge much faster in the early iterations than the standard gradient or conjugate gradient algorithm. Nevertheless, with noisy datasets, after a certain number of iterations the OS algorithm becomes unable to improve the updated object, because the diffraction patterns of adjacent positions are inconsistent due to the presence of noise. Hence, strictly speaking, all the PIE strategies, including Eqn. (2.1.17) should *not* be considered as *convergent* algorithm in the long-run [40]. In the next subsection, we will present the conjugate gradient strategy that is proven to be convergent for noisy datasets.

The nonlinear conjugate-gradient algorithm

The second class of algorithms is the *nonlinear conjugate-gradient* (NCG) for the minimization of general nonlinear functions [41]. It was introduced by Fletcher and Reeves in the 1960s and it is one of the earliest known techniques for solving large-scale nonlinear optimization problems [42].

[3] In the optimization literature, this scaling strategy is a known *preconditioning*, see for instance [41] for more details.

Contrary to the PIE, the NCG algorithm requires the complete gradient of the fitting function $\mathcal{L}$ for the current iteration k. This gradient reads

$$\partial\mathcal{L}_k = \sum_j \partial\mathcal{L}_{k,j}. \tag{2.1.19}$$

Beginning with an initial estimate $\boldsymbol{\rho}_0$, the NCG algorithm generates a *sequence* of iterates $\{\boldsymbol{\rho}_k\}_{k=0}^{\infty}$ decreasing the criterion $\mathcal{L}(\rho)$ in a monotonic fashion, and which is stopped when the iterate is sufficiently close to a minimizer. This sequence can be expressed as a function of the previous iterate, plus a correction term:

$$\boldsymbol{\rho}_{k+1} = \boldsymbol{\rho}_k + \beta_k \boldsymbol{d}_k \tag{2.1.20}$$

The correction term is the product of the step-length β_k with a direction $\boldsymbol{d}_k$, which is a strictly decreasing direction for the cost-function $\mathcal{L}$:

$$\boldsymbol{d}_k = \begin{cases} -\partial\mathcal{L}_k \doteq \boldsymbol{\Lambda} & \text{for } k = 0 \\ -\partial\mathcal{L}_k \doteq \boldsymbol{\Lambda} + \gamma \boldsymbol{d}_{k-1} & \text{otherwise} \end{cases} \tag{2.1.21}$$

The scalar parameter γ is given by the Fletcher-Reeves formula

$$\gamma = \frac{\sum_{\mathbf{n}} \partial\mathcal{L}^*_{k;\mathbf{n}} \times \boldsymbol{d}_{k;\mathbf{n}}}{\sum_{\mathbf{n}} \partial\mathcal{L}^*_{k-1;\mathbf{n}} \times \boldsymbol{d}_{k-1;\mathbf{n}}} \tag{2.1.22}$$

where $\boldsymbol{d}_{k;\mathbf{n}}$ stands for the scalar element with coordinate $\mathbf{n} := (n_x, n_y)$ in the matrix $\boldsymbol{d}_k$. It is also worth mentioning that the step-length β_k is iteration-dependent so that the criterion decreases significantly for the current step. While the exact calculation of a minimizer in β value would be extremely computationally costly, an *inexact* line-search routine can be implemented so that the step-length allows a sufficient decrease of the criterion along the chosen direction with a very small cost. More precisely, β is chosen for the current iteration k so that the *Armijo* condition holds [40, 41]:

$$\Delta\mathcal{L} + c\beta_k \sum_{\boldsymbol{n}} \partial\mathcal{L}^*_{k;\boldsymbol{n}} \times \boldsymbol{d}_{k;\boldsymbol{n}} \geqslant 0 \tag{2.1.23}$$

with $c \in (0,1)$ and $\Delta\mathcal{L} \hat{=} \mathcal{L}(\boldsymbol{\rho}_k + \beta_k \boldsymbol{d}_k) - \mathcal{L}(\boldsymbol{\rho}_k)$. In practice, a β_k meeting the condition (2.1.23) is found with a standard *backtracking* technique[4].

Contrary to the PIE/OS strategy, the NCG algorithm is proven to converge to a minimizer of the criterion in the asymptotic limit. However, its convergence is slower in the early iterations in comparison to the PIE/OS iteration. Hence, NCG can be used as a complementary strategy to refine the inversion result of the OS algorithm, when the OS algorithm is unable to improve the object any further.

[4]Let α be a positive constant such that $\alpha < 1$: the backtracking technique is the successive test of the relation (2.1.23) with $\beta \in \{\alpha\overline{\beta}, \alpha^2\overline{\beta}, \alpha^3\overline{\beta}, \cdots\}$, the first integer l leading to Eq. (2.1.23) is then selected as $\beta_k = \alpha^l\overline{\beta}$.

2.2 Principles of 3D ptychographic imaging

In the previous section, we talked about the physical model that describes the acquired intensity data at each scan position, in the notional case of a two-dimensional object. We talked as well, about how the reconstructed image is obtained with the use of phase-retrieval gradient-based optimization algorithms. Imaging of a three-dimensional object though, demands a different modeling and data acquisition in order to retrieve the complete 3D electron density. There are mainly two different approaches that can be used, depending on the structural features that one aims to study:

- Ptychographic X-ray computed tomography (CT) for phase-contrast imaging [43]
- 3D X-Ray Bragg ptychography for strain imaging [44]

The first technique allows the reconstruction of the object's complex-valued transmission function, which is then converted to electron density. The retrieved phase represents the refractive index of the object [43, 45]. It exploits the fact that different materials have different refractive indices, in order to distinguish complex structures. On the other hand in Bragg ptychography, the retrieved phase corresponds to the projection of the crystal lattice displacement on the scattering vector as derived from Eqn.(1.1.9).

In this section, we will discuss about modeling the forward problem in the practical case of a three-dimensional object and retrieving of 3D samples. We are going to address the problem of imaging different properties and structural features in two contexts. Namely the case of phase-contrast imaging that can be applied on both periodic and non-periodic specimen, and the case of 3D strain imaging which has sense only on crystalline objects with a periodic lattice.

2.2.1 3D ptycho-tomography: The forward modeling

The basic problem of tomography is how to reconstruct the electron density of a 3D object, given a set of 2D projections originating from various angles. The mathematical basis for tomographic imaging was developed by Johann Radon [46]. The next figure illustrates the problem, not in the case of traditional CT where the complete object is illuminated for different values of the angle ϕ, but in the particular case of ptychographic CT.

In ptychographic CT the object is laterally scanned as it is depicted on Fig.2.1a, but additionally for several angles of incidence, as seen on Fig.2.3. As a result, the forward modeling for that modality requires that we consider the probe $p_{j;\phi}$ shifted in $\boldsymbol{r}_j$ with angle of incidence ϕ, so that the exit-field $\psi_{j;\phi} : \mathbb{R}^3 \to \mathbb{C}$ now reads

$$\psi_{j;\phi} \hat{=} p_{j;\phi}\, \rho. \tag{2.2.1}$$

The tomographic experiment implies that a projection of the 3D exit-field is performed along the direction x' (*i.e.* with angle ϕ). This results in a *projected* exit-field $\xi_{j;\phi} : \mathbb{R}^2 \to \mathbb{C}$ that reads

$$\xi_{j;\phi} \hat{=} \mathcal{P}_{\phi_n} \psi_{j;\phi} \tag{2.2.2}$$

with $\mathcal{P}_\phi$ the projection operator along x' [47]. Hence, the corresponding (bi-dimensional) diffracted far-field $\Psi_{j;\phi} : \mathbb{R}^2 \to \mathbb{C}$ reads

$$\Psi_{j,\phi}(\mathbf{q}') = (\mathcal{F}_{2D}\xi_{j;\phi})(\mathbf{q}') \tag{2.2.3}$$

with $\mathcal{F}_{2D}$ the 2D Fourier transform operator. The *expected* intensity on the detection plane is then deduced:

$$h_{j;\phi}(\mathbf{q}') = |\Psi_{j,\phi}|^2(\mathbf{q}') + b_{j;\phi}(\mathbf{q}') \tag{2.2.4}$$

where $b_{j;\phi}$ is the expected background intensity and $\mathbf{q}'$ is the vector on the detection plane —*i.e.*, the reciprocal frame associated to the $y'Oz$ plane, as seen on Fig.2.3

$$\mathbf{q}' = q_{y'}\ \mathbf{q}_{y'} + q_z\ \mathbf{q}_z. \tag{2.2.5}$$

The above relation (2.2.4) gives the formal dependency between the expected intensity on the detection plane and the sample to retrieve.

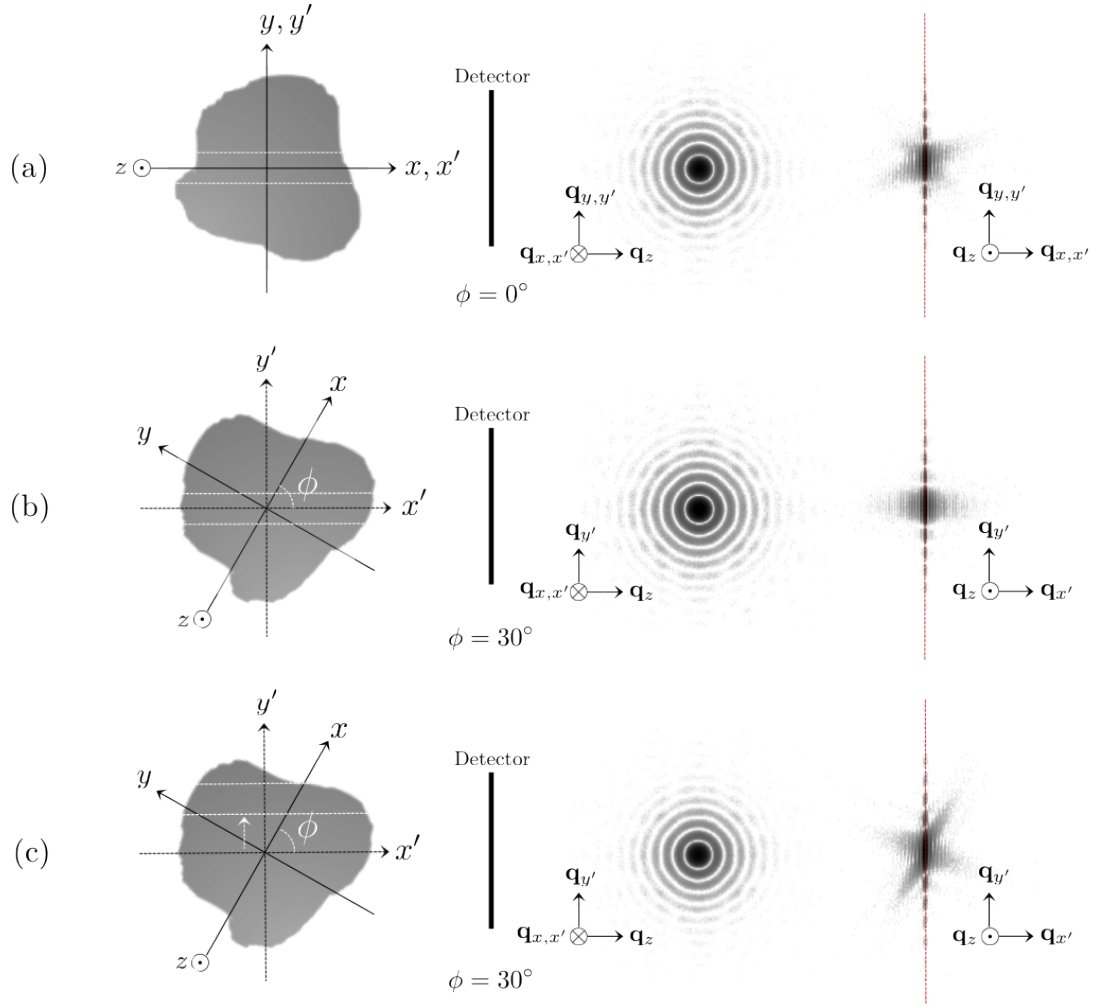

Figure 2.3: Two-dimensional slices of an homogeneous in the direction of z object and the far-field of the projections of the object to the beam. With the white dashed lines we see the intersections of the object with the beam. (a) For an angle of incidence $\phi = 0°$ (b) For $\phi = 30°$ and (c) For $\phi = 30°$ but in another lateral position of the scan on the $y'Oz$ plane.

2.2.2 3D ptycho-tomography: The reconstruction strategy

The reconstruction of a non-periodic 3D object is done in two steps [43]. In the first step, the 2D projections of the *entire* object in DS are retrieved using phase-retrieval algorithms (See Sec. 2.1.2 for an infinitely thin FZP object) for every angle of incidence ϕ spanning $[0\ \pi]$. In the second step, using the set of phased 2D projections, a 3D reconstruction is performed by the standard *filtered back-projection* tomographic algorithm [48, 49].

Indeed, the validity of such a two-step strategy relies on a few assumptions concerning the probe that are rarely discussed in the literature. Let us express the probe $p_{j;\phi}$ and the object ρ

in the *rotated* coordinate system $\boldsymbol{r}' \equiv (x', y', z')^t$, both these quantities being denoted hereafter $p'_{j;\phi}$ and ρ'. The projection (2.2.2) within this new system is easily obtained by

$$\xi'_{j;\phi}(y', z') \;=\; \int_{x'} p'_{j;\phi}(x', y', z')\, \rho(x', y', z')\mathrm{d}x'. \tag{2.2.6}$$

Now, let us consider the following simplifications: $p'_{j;\phi}$ is invariant of (i) the angle ϕ, and (ii) the propagation direction, *i.e.* along x'. These two assumptions are mathematically equivalent to

$$p'_{j;\phi}(x', y', z) \equiv p'_j(y', z), \quad \forall x', \phi \tag{2.2.7}$$

and lead to a simplification of the integral (2.2.6)

$$\xi'_{j,\phi}(y', z') \;=\; p'_j(y', z') \times \xi'_\phi(y', z') \tag{2.2.8}$$

with

$$\xi'_\phi(y', z') \;\hat{=}\; \int_{x'} \rho'(\mathbf{r}')\mathrm{d}x'.$$

the 2D projection of the *entire* object for the angle ϕ. This projection ξ'_ϕ is precisely the quantity that one aims at retrieving in the "first step" of the standard approach described in the literature [49]. In the X-ray regime, the above assumptions (i) and (ii) are met, provided that the temporal stability of the probe is granted, and the $\mathcal{PLD}$ of the incident beam inside the object, not larger than the coherence lengths of the beam.

In order to retrieve the 2D projection of the object ξ_ϕ using a ptychographic inversion algorithm (PIE, Difference-Map [50] etc.), is important having good knowledge of the probe, which can be reconstructed independently either using the inversion approaches demonstrated in Refs.[51, 52], or by performing a ptychography experiment of a perfectly known sample and inverting the diffraction data with output the illumination function [53].

2.2.3 3D ptycho-tomography: Comments

Ptychography was numerically shown in 2004 [54] and experimentally demonstrated in 2007 in two dimensions, using coherent X-rays [55] and visible laser light [56]. Soon after, many research groups around the world turned over the development of ptychographical lensless imaging. The following efforts, concentrated in the improvement of the technique's resolution by treating different issues as the presence of noise, the need of having good knowledge of the illumination function, improving algorithms convergence by adding extra *a priori* information with the form of different constraints *etc.*

In 2009, the implementation for the additional parallel refinement of the probe, showed that the reconstructed image quality could be further improved [57, 58]. In addition to that, the realization that the beam and sample position uncertainties due to experimental setup instabilities during a ptychography experiment, could be corrected, gave birth to new algorithmic processes that aimed to correct the illumination positions errors [59, 60].

In 2010, the development of 3D ptychographic computed tomographic imaging in transmission geometry has been shown, with the reconstruction of a micrometer-sized bone specimen along with its *lacuno-canalicular* network with a resolution of about 150 nm [43]. In this approach, a ptychography scan is performed and coherent diffraction patterns are collected from the sample at each of the scan positions.

2.2.4 X-ray 3D Bragg ptychography: The forward modeling

For strain imaging, the experimental geometry makes the 3D sampling process different, compared to the tomographic approach. Instead of the 0-π angular scanning of the sample for the collection of different projections, the sample is "rocked" in the vicinity of a Bragg reflection. This is usually done by rotating the sample in very small angular steps, changing the angle of incidence θ_B in the vicinity of the Bragg peak, with range of 0.5°and results in a translation of the detection frame through the diffraction peak. The modeling that links the unknown object to this measurement in the Bragg geometry is now stated.

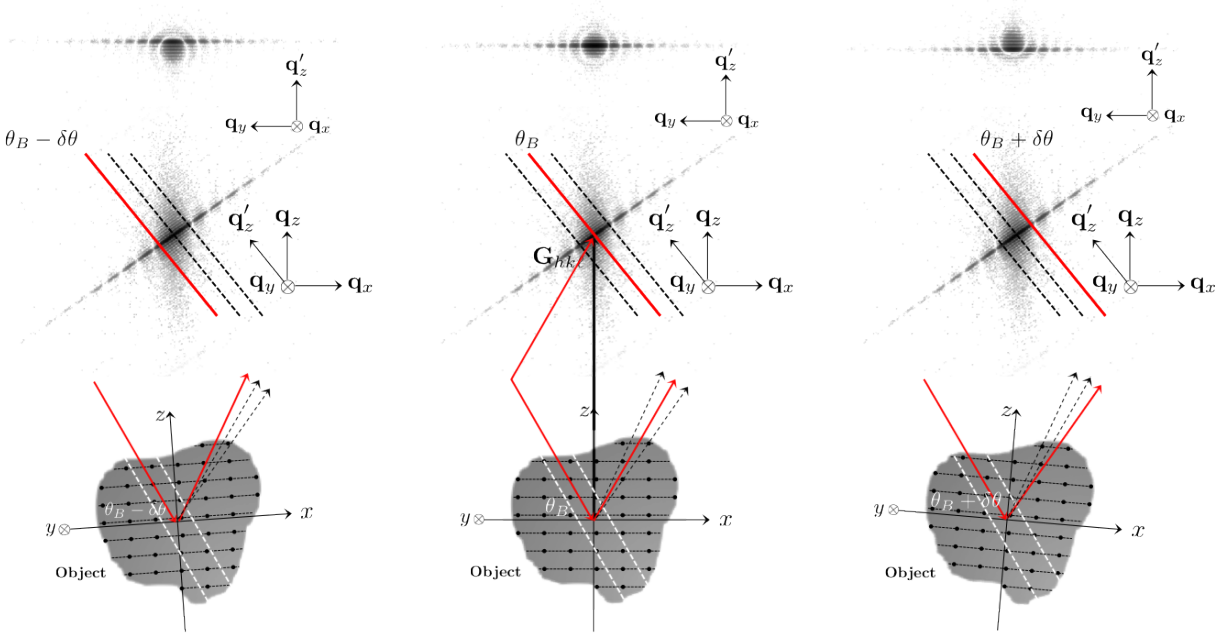

Figure 2.4: Intensity patterns measured during a Bragg ptychography experiment, along the *rocking curve* direction. Slices of the 3D Fourier transform in the vicinity of the Bragg peak at (a) $\theta_n = \theta_B - \delta\theta$, (b) $\theta_n = \theta_B$ and (c) $\theta_n = \theta_B + \delta\theta$. The dashed red lines represent the relative positions of the $\mathbf{k}_f$ vectors for each value of θ_n.

The reciprocal space sustained by the measurement. Let $\Psi_j(\mathbf{q})$ be the far-field expressed in the RS orthonormal basis $(\mathbf{q}_x, \mathbf{q}_y, \mathbf{q}_z)$ which is conjugate of the DS "laboratory" orthonormal basis $(\mathbf{e}_x, \mathbf{e}_y, \mathbf{e}_z)$. As usual[5], we consider the relation

$$\Psi_j(\mathbf{q}) = (\mathcal{F}_{3D}\psi_j)(\mathbf{q}) \qquad \text{with} \qquad \psi_j(\mathbf{r}) \hat{=} (p_j\rho)(\mathbf{r})$$

where $\mathcal{F}_{3D}$ is the 3D Fourier transform. In Bragg geometry, the diffraction pattern is detected along the $(\mathbf{q}'_y, \mathbf{q}'_z)$ plane, whereas the rocking-curve consists in shifting this inclined detection along $\mathbf{q}'_x$ [See Fig. 2.4], thus, it is more convenient to derive the relevant quantities in the nonorthogonal, *natural* system $(\mathbf{q}'_x, \mathbf{q}'_y, \mathbf{q}'_z)$.

[5]The use of the 3D Fourier transform is based on the concept of the *Fourier synthesis* of a signal. Since assembling all the 2D intensity measurements will lead to a 3D numerical window in RS as depicted in Fig. 2.4 by the sampling process, the inverse Fourier transform will relate the 3D RS natural frame with the 3D DS natural frame [17, 26].

Hereafter, the frame $(\mathbf{q}_x, \mathbf{q}_y, \mathbf{q}_z)$ is called the "*RS laboratory system*" since it is conjugated to the laboratory frame $(\mathbf{e}_x, \mathbf{e}_y, \mathbf{e}_z)$. In contrast, $(\mathbf{q}'_x, \mathbf{q}'_y, \mathbf{q}'_z)$ is adapted to the representation of the measurement: it is called hereafter the "*RS natural system*".

Obviously, any RS function can be represented in both coordinate systems according to the following relation

$$\mathbf{q} = \boldsymbol{B}\mathbf{q}', \quad \text{with} \quad \boldsymbol{B} = \begin{pmatrix} 1 & 0 & -\sin\theta_B \\ 0 & 1 & 0 \\ 0 & 0 & \cos\theta_B \end{pmatrix} \tag{2.2.9}$$

where $\boldsymbol{q} = (q_x, q_y, q_z)^t$ and $\boldsymbol{q}' = (q'_x, q'_y, q'_z)^t$ represent the same RS point in the $(\mathbf{q}_x, \mathbf{q}_y, \mathbf{q}_z)$ and $(\mathbf{q}'_x, \mathbf{q}'_y, \mathbf{q}'_z)$ frames. In particular, the far-field $\Psi_j(\mathbf{q})$ also reads

$$\Psi_j(\boldsymbol{B}\mathbf{q}') \mathrel{\hat{=}} \Psi'_j(\mathbf{q}') \tag{2.2.10}$$

hence expressing the far-field in the new coordinate system. The *detected* intensity on the detector plane $y'_j(\mathbf{q}')$ is then related to the *expected* intensity by the usual model

$$h'_j(\mathbf{q}') \mathrel{\hat{=}} |\Psi'_j|^2(\mathbf{q}') + b_j(\mathbf{q}') \tag{2.2.11}$$

where b_j is the expected intensity of the background component. It should be stressed, however, that working within this "natural" system *implicitly* defines the exit-field in a new (DS) coordinate system.

The direct-space system: "natural" vs. "laboratory". An important point to keep in mind is that the inverse Fourier transform of a function in $(\mathbf{q}'_x, \mathbf{q}'_y, \mathbf{q}'_z)$ is consistent with a DS system that is *no longer* the original laboratory frame $(\mathbf{e}_x, \mathbf{e}_y, \mathbf{e}_z)$. For instance, the inverse Fourier transform of the far-field Ψ'_j (2.2.10) defines the exit-field

$$\psi'_j(\mathbf{r}') = \left(\mathcal{F}_{3\mathrm{D}}^{-1}\Psi'_j\right)(\mathbf{r}')$$

with $\mathbf{r}' = (r'_x, r'_y, r'_z)$ a point in a coordinate system $(\mathbf{e}'_x, \mathbf{e}'_y, \mathbf{e}'_z)$ conjugated to the one spanned by the measurement. In opposition to the "laboratory" coordinate system, this new system is called hereafter "*DS natural system*". Both these DS systems are related by [See appendix B]

$$\boldsymbol{r} = \mathbf{A}\boldsymbol{r}' \qquad \text{with} \qquad \mathbf{A} \equiv (\mathbf{B}^{-1})^t \tag{2.2.12}$$

with $\mathbf{r} = (r_x, r_y, r_z)$ a point in the $(\mathbf{e}_x, \mathbf{e}_y, \mathbf{e}_z)$ DS laboratory system. In addition, we still have

$$\psi'_j \mathrel{\hat{=}} p'_j \times \rho'$$

with the DS quantities

$$\begin{cases} p'_j(\mathbf{r}') = \det(\boldsymbol{A}) \times p_j(\mathbf{A}\boldsymbol{r}') \\ \\ \rho'(\mathbf{r}') = \rho(\mathbf{A}\boldsymbol{r}'). \end{cases} \tag{2.2.13}$$

Finally, before we proceed to the definition of the reconstruction algorithm, the RS and DS quantities need to be sampled within their natural coordinate systems.

Sampling with "natural" coordinates in the reciprocal and direct spaces. The natural coordinate system in RS was introduced so that the sampling in this space follows the detection scheme. More specifically, for a fixed q'_x, the measured intensity on the detection plane corresponds to a point of the rocking curve. The sampling in the detector plane is regular and reads

$$q'_y = m'_2 \delta q'_y \qquad \text{with} \qquad -\frac{M_2}{2} \leqslant m'_2 \leqslant +\frac{M_2}{2} - 1 \tag{2.2.14}$$

$$q'_z = m'_3 \delta q'_z \qquad \text{with} \qquad -\frac{M_3}{2} \leqslant m'_3 \leqslant +\frac{M_3}{2} - 1 \tag{2.2.15}$$

where $\delta q'_y$ and $\delta q'_z$ are the discretization step along $\boldsymbol{q}'_y$ and $\boldsymbol{q}'_z$, respectively. Along the rocking-curve, one usually proceeds to *regular angular step* δ_θ leading to the following sampling along $\boldsymbol{q}'_x$ [See Appendix B]

$$q'_x = \frac{4\pi\sqrt{2}}{\lambda}\left(1 - \cos(m'_1\delta_\theta)\right)^{1/2} \sin\theta_B \qquad \text{with} \qquad -\frac{M_1}{2} \leqslant m'_1 \leqslant +\frac{M_1}{2} - 1 \tag{2.2.16}$$

which, thanks to the very small angular excursion $m'_1\delta_\theta$ about θ_B, is equivalent within a good approximation to the regular sampling

$$q'_x = m'_1 \delta q'_x \qquad \text{with} \qquad -\frac{M_1}{2} \leqslant m'_1 \leqslant +\frac{M_1}{2} - 1 \tag{2.2.17}$$

where

$$\delta q'_x \mathrel{\hat{=}} \frac{4\pi\delta_\theta}{\lambda} \sin\theta_B.$$

As a result, the sampling in RS can be considered as *regular*[6] along all three directions (q'_x, q'_y, q'_z), and we define the discretized measurements

$$\boldsymbol{Y}'_j \;\mathrel{\hat{=}}\; \left\{ y'_j(m'_1\delta q'_x, m'_2\delta q'_y, m'_3\delta q'_z) \right\} \tag{2.2.18}$$

related to the discretized version of the far-field and the expected intensity (respectively)

$$\begin{aligned} \boldsymbol{\Psi}'_j &\;\mathrel{\hat{=}}\; \left\{ \Psi'_j(m'_1\delta q'_x, m'_2\delta q'_y, m'_3\delta q'_z) \right\} \\ \mathbf{h}'_j &\;\mathrel{\hat{=}}\; \left\{ h'_j(m'_1\delta q'_x, m'_2\delta q'_y, m'_3\delta q'_z) \right\}. \end{aligned} \tag{2.2.19}$$

The DS quantities needs also to be discretized in their *natural* (i.e., not laboratory) coordinate system. Let us consider a voxel in this DS space $(\delta x', \delta y', \delta z')$. The *discretized* form of the object and the probe reads

$$\boldsymbol{\rho}' \;\mathrel{\hat{=}}\; \left\{ \rho'(n'_x\delta x', n'_y\delta y', n'_z\delta z') \right\} \tag{2.2.20}$$

$$\mathbf{p}'_j \;\mathrel{\hat{=}}\; \left\{ p'_j(n'_x\delta x', n'_y\delta y', n'_z\delta z') \right\} \tag{2.2.21}$$

with $\mathbf{n}' \equiv (n'_x, n'_y, n'_z) \in \mathbb{Z}^3$ the index triplet such that

$$-N_x/2 \leqslant n'_x \leqslant +N_x/2 - 1,$$

$$-N_y/2 \leqslant n'_y \leqslant +N_y/2 - 1$$

$$-N_z/2 \leqslant n'_z \leqslant +N_z/2 - 1.$$

[6] The regular sampling allows the direct computation of the exit-field from the far-field (and *vice versa*) with the DFT. On the contrary, an irregular sampling would have required either the interpolation of the dataset or the interpolation of the far-field.

Let us also introduce $\mathcal{S}'_j$ the *support of the beam* in the natural DS, *i.e.,* $\mathcal{S}'_j$ gathers the index triplets where the probe $\mathbf{p}'_j$ is not uniformly zero. The discretized exit-field is then defined by

$$\boldsymbol{\psi}'_j \,\hat{=}\, \left\{p'_j(n'_x\delta x', n'_y\delta y', n'_z\delta z') \times \rho'_j(n'_x\delta x', n'_y\delta y', n'_z\delta z') : (n'_x, n'_y, n'_z) \in \mathcal{S}'_j\right\}. \tag{2.2.22}$$

The numerical calculation of the far-field from the exit-field is then obtained *via* a discrete Fourier transform (DFT):

$$\boldsymbol{\Psi}_j = \mathrm{DFT}_{3\mathrm{D}}(\boldsymbol{\psi}_j). \tag{2.2.23}$$

We note that this equation demands that the sampling between DS and RS satisfies the next relations

$$\delta q'_x = \frac{1}{M_1\ \delta x'}, \quad \delta q'_y = \frac{1}{M_2\ \delta y'}, \quad \text{and} \quad \delta q'_z = \frac{1}{M_3\ \delta z'}. \tag{2.2.24}$$

All the key ingredients are now available to derive the reconstruction algorithm.

2.2.5 X-ray 3D Bragg ptychography: The reconstruction strategy

We now can consider the reconstruction strategy following a similar line to the one adopted in Sec. 2.1.2. It will be instructing, though, to derive first some expressions in the continuous domain. So let us define the reconstructed object as a minimizer of the following least-square criterion

$$\mathcal{L}'(\rho') \,\hat{=}\, \sum_j \|\mathrm{y}_j^{1/2}(\mathbf{q}') - h_j'^{1/2}(\mathbf{q}')\|^2 \tag{2.2.25}$$

where $\mathrm{y}_j(\mathbf{q}')$ the intensity at $\mathbf{q}'$ on the detection plane and $||\cdot||$ is the Euclidian distance in the measurement space. From this expression, a gradient-based algorithm can be built by iteratively updating the object in the basis $(\mathbf{e}'_x, \mathbf{e}'_y, \mathbf{e}'_z)$: for the j-th probe position, this gradient reads

$$\partial\mathcal{L}'_j(\mathbf{r}') = 2\, p'^*_j(\mathbf{r}') \left[\psi'_j(\mathbf{r}') - \hat{\psi}'_j(\mathbf{r}')\right] \tag{2.2.26}$$

where

$$\psi'_j \,\hat{=}\, \mathcal{F}_{3D}^{-1}\Psi'_j \qquad \text{and} \qquad \hat{\psi}'_j \,\hat{=}\, \mathcal{F}_{3D}^{-1}\hat{\Psi}'_j \tag{2.2.27}$$

with

$$\hat{\Psi}'_j \,\hat{=}\, \Psi'_j \left(\frac{\mathrm{y}_j}{h_j}\right)^{1/2}. \tag{2.2.28}$$

If the probe was beforehand provided in the DS laboratory system, p'_j (2.2.13) needs to be computed only once *via* an interpolation step, then it can be used in Eqn. (2.2.26) during the whole iterative minimization process. When the iterative minimization is completed, an additional interpolation step is needed to bring back the reconstruction $\hat{\rho}'$ in the laboratory frame. Therefore, updating the object in the "natural" $(\mathbf{e}'_x, \mathbf{e}'_y, \mathbf{e}'_z)$ DS basis [*i.e.,* with Eqn. (2.2.26)] requires only two interpolation steps. In comparison, an iterative minimization designed in the original laboratory system $(\mathbf{e}_x, \mathbf{e}_y, \mathbf{e}_z)$ would be much more expensive. For that purpose, let us express the gradient (2.2.26) in the original basis thanks to the relation (2.2.12)

$$\partial\mathcal{L}_j(\mathbf{r}) = 2\, p^*_j(\mathbf{r}) \left[\psi'_j(\boldsymbol{A}^{-1}\mathbf{r}) - \hat{\psi}'_j(\boldsymbol{A}^{-1}\mathbf{r})\right]. \tag{2.2.29}$$

Clearly, this expression can be used to devise an iterative algorithm working in the original system. However, the computation of $\psi'_j(\boldsymbol{A}^{-1}\mathbf{r})$ and $\hat{\psi}'_j(\boldsymbol{A}^{-1}\mathbf{r})$ would require an interpolation step each time the object is updated, hence increasing significantly the computational burden in each iteration.

The numerical implementation of the 3D Bragg ptychographic reconstruction algorithm requires the discretized version of both the criterion (2.2.25) and the gradient (2.2.26). The least-square criterion reads

$$\mathcal{L}'(\boldsymbol{\rho}') = \sum_j \sum_{\mathbf{m}'} \left[(\boldsymbol{Y}'_{j;\mathbf{m}'})^{1/2} - (\boldsymbol{h}'_{j;\mathbf{m}'})^{1/2} \right]^2 \tag{2.2.30}$$

where the triplet $\mathbf{m}' \hat{=} (m'_1, m'_2, m'_3)$ locates an element in the matrices $\boldsymbol{Y}'_j$ and $\mathbf{h}'_j$ according to the definitions (2.2.18) and (2.2.19). For the j-th probe position, the gradient with respect to the unknown object $\boldsymbol{\rho}'$ reads

$$\partial\mathcal{L}'_{j;\mathbf{n}'}(\boldsymbol{\rho}') = \begin{cases} 2\boldsymbol{p}'^{*}_{j;\mathbf{n}'} \times \left[\mathrm{DFT}_{3\mathrm{D}}^{-1} \left(\boldsymbol{\Psi}'_j(\boldsymbol{\rho}') - \hat{\boldsymbol{\Psi}}'_j(\boldsymbol{\rho}') \right) \right]_{\mathbf{n}'} & \forall \mathbf{n}' \in \mathcal{S}'_j \\ 0 \quad \text{otherwise} \end{cases} \tag{2.2.31}$$

with $\hat{\boldsymbol{\Psi}}'_j$ the discrete versions of the corrected far-field (2.2.28). With this later relation, gradient-based 3D Bragg reconstruction algorithms are obtained straightforwardly from the 2D case presented in Sec. 2.1.2.

2.3 Developments of 3D Bragg X-ray ptychography

The feasibility of Bragg ptychography was numerically investigated [61], implemented and experimentally demonstrated in 3D on a test object composed by two (110) oriented Si lines etched on top of a SOI line [44]. Multiple 2D diffraction patterns were recorded at different incident θ angles in the vicinity of the (220) Bragg reflection, and assembled as a 3D volume in RS for each of the scan positions. The entire dataset was then inverted using the PIE algorithm along with a regularized support constraint, and the probe was retrieved as well. The numerical demonstration of regularization in 2D Bragg ptychography was shown from Godard *et al.* [61] in 2011.

Another noteworthy achievement which allowed the considerable decrease of the exposure time for a crystal in Bragg geometry was shown by Berenguer *et al.* [62], using an undersampled ptychographical dataset. The development of different criteria for the evaluation of the reconstruction quality and the incorporation of Bayesian statistics in gradient optimization algorithms [40] can be considered as the finest "paint strokes" for the state of the art of Bragg ptychographical imaging.

Nevertheless, despite the above advancements there are important experimental difficulties that hinder the broad and successful application of the technique. For example, the needed deconvolution of the illumination in order to retrieve the crystal electron density, requires the good knowledge of the illumination function. In addition to that, redundancy in the encoded information of the diffraction patterns is the key element for the success of the ptychographic approach [38]. So, in order to achieve data redundancy, an important amount of overlapping at each of the scan positions is needed. That means, diffraction patterns have to be recorded at several positions and for several incident angles, something which makes the total time of the measurement and the difficulty to achieve good sample stability important. The need for very local measurements, demands the use of a beam with diameter of the order of a few tens of nanometers, and in order to achieve a sufficient overlapping amount, one needs to move the piezostage where the sample is placed, by a few nanometers, reaching the limits of the device's capabilities.

Another issue is radiation damage. As the technique demands multiple exposures of the sample to hard X-rays repeatedly, it makes difficult the study of radiation-sensitive or weakly scattering specimen. Finally, photon shot noise is an everlasting problem generally in CDI techniques, since its presence deteriorates the quality of the reconstructed image [40]. Thus, depending on the sample, the exposure times have to be optimized in order to collect a sufficient number of photons, without tampering the sample's structure [63].

Due to the experimental difficulties that we discussed previously (radiation damage, experimental setup stability, presence of noise), and the inversion related issues, there exist only few successful applications of 3D Bragg ptychography, with the most recent being Ref. [64]. We could not omit though, significant achievements of 2D Bragg ptychography (or Bragg Projection Ptychography), in imaging the strain of a multilayer semiconductor prototype device with an unprecedented resolution of 7nm [3], or the visualization of a dislocation strain field inside a Si crystal at a region of approximately $10 \times 10 \mu m^2$ [65].

Nevertheless, until today, all experimental demonstrations of 3D strain imaging have been applied on finite-size periodic objects, resistant to radiation damage, with important scattering powers like Au, and with quite mere deformation fields. Thus, the successful demonstration of the technique on more complex systems that present actual interest for materials science, microelectronics devices or biology is still pending.

Chapter 3

InP/InGaAs system and experimental setup

Contents

3.1 Motivations and strategies

As it was stated in the description of the state of the art for 3D strain imaging of crystalline objects in Section 2.3, studies of micrometer and nanometer-sized crystals have started since the beginning of the past decade [16, 17]. These studies were performed on highly scattering objects with finite-size and intermediate strain values using the CDI approach of Section 1.1.2. In order to overcome the restrictions that CDI imposed, 3D Bragg ptychography was proposed and demonstrated [44]. It has allowed the 3D imaging of strain in an extended object, whose size can be larger than the X-rays transverse coherence lengths. However, it is interesting to note that a support constraint along the thickness direction was still needed, introduced through a regularization approach.

The aim of this PhD thesis is to further extend this technique, in order to apply it on a highly strained and extended nanostructured thin film. In other words, we would like to image the crystalline displacements inside a multilayer thin film and ideally achieve nanometer spatial resolution. This step is mandatory to demonstrate the potential applications of Bragg ptychography, as many structures of this kind are encountered in material science. To this aim, we have

applied Bragg ptychography on a well calibrated though complex sample, an InP/InGaAs nanostructured thin film bonded on a *Si* substrate. This chapter presents the experimental elements needed for this work.

In Section 3.2, we will present the sample, including the interest it presents for microelectronics applications, the fabrication process, the structure design and a set of preliminary structural characterizations.

In Section 3.3, we will describe the Bragg ptychography experimental setup and the Bragg ptychography scan modality.

In the last section, we will detail the main features exhibited by the Bragg ptychography experimental data.

3.2 The InP/InGaAs thin film

3.2.1 III-V semiconductor compound integration on Si

The constant need for fast data transmission demands fast telecommunications and has resulted in an extremely active research field. The versatility of Si, as well as its abundance and low production costs, have made it the dominant material for many electronic and optical devices [66]. However, there are other semiconductors that have certain advantages over silicon. For example, III-V semiconductor compounds, such as gallium arsenide (GaAs) and indium phosphide (InP), have a direct bandgap, allowing them to efficiently emit and absorb photons with energies in their respective bandgaps. Furthermore, they have a much higher electron mobility than silicon and have been used to make high-power and high-frequency electronics [67]. These are the principal reasons why GaAs-, InP- and GaN-based materials have been the dominant material systems for semiconductor diode lasers [68] since their first demonstration in 1962.

In order to benefit from their properties, these materials need to be integrated on Si-based circuits, something which is usually not done with epitaxial growth techniques. The reason is that the lattice deviation between Si and III-V semiconductor compounds is large enough to induce important stresses, which in turn lead to the generation of several defects at the interface, like dislocations that can spread through the layer and make the material unsuitable for device fabrication [69]. Numerous approaches have been used to reduce the dislocation density to around 10^5-10^6 cm^{-2} [70, 71, 72, 73, 74, 75, 76], but this is still around two orders of magnitude higher than in InP- or GaAs-based epitaxial wafers for room-temperature lasers.

The solution to this problem was given by growing independently the III-V compound, and then bonding it onto a Si substrate using an intermediate layer of oxide [68, 77]. [1] This approach allows the fabrication of almost defect-free, high-speed, low-power-consumption and low-cost photonic devices like photo-emission diodes [79]. In this context, one of the key questions is the preservation of the III-V compound structure through the bonding process.

3.2.2 Sample structure design and fabrication

For this thesis, which aimed at testing the limits of Bragg ptychography, a specific sample had to be designed. Ideally, the sample fabrication had to satisfy two main conditions: (*i*) the sample fabrication had to be versatile enough in order to allow for the design of accurately chosen structural parameters and (*ii*) had to be highly controlled in order to guarantee that the desired structural features were still present in the final sample structure. These two conditions were met in the elaboration process developed by A. Talneau and co-workers at the Laboratory for Photonics and Nanostructures (LPN) of the Centre National de la Recherche Scientifique (CNRS)

[1] It is shown that direct-fusion bonding without the intermediation of a metal or oxide layer (*oxide-free bonding*) leads to the fabrication of highly-conductive heterojunctions [78], and thus, it is preferable.

in Marcoussis, Paris. The lab is composed of several scientific teams, developing fundamental and applied research in the fields of photonics, nano-electronics, materials, microfluidics and nano-biotechnology. It is specialized in the integration of III-V semiconductors for optoelectronics on Si, fabrication of III-V nanowires, planar heterostructures for wave engineering. Their expertise go along with highly developed competences in the analysis, characterization and modeling of semiconducting nanostructures.

The fabrication involves first the growth of the desired III-V structure by metal-organic vapor phase epitaxy onto an InP substrate. The material which presents the zinc-blende crystal structure [80] can be used as a substrate for the epitaxial growth of other III-V semiconductors. [81]. All the grown layers are lattice-matched on the InP substrate. The grown structure includes a 300nm thick InGaAs sacrificial layer, which will be chemically remove to separate the structured layer from the InP substrate by selective etching. Then, the Si substrate and the grown structure surfaces are both cleaned and desoxidized and both re-oxidized, with a dedicated and controlled process: the Si surface is thermally oxidized at 1050°C during 20s, while the InP surface is oxidized during a 4min inductive coupled plasma reactive ion etching operated at zero bias. Both oxides are then activated by ozone during 30s, put in contact and annealed at 300°C during 3h [82]. The InP substrate is then chemically removed, followed by the InGaAs selective layer removal. The nanostructured InP stack is then adhesively bonded on Si.[2] The thickness of the Si oxide bonding layer is $\sim$ 5nm.
For our study, the final structure had to verify a few conditions.

- The thickness of the total layer has to be large enough in order to ensure that our Bragg diffraction intensity will present a large signal-to-noise ratio during the ptychography scan, but small enough in order to guarantee that the beam path length difference will remain smaller than the longitudinal coherence length of the beam. This upper thickness limit is estimated to about 370nm [See Appendix A]. According to previous measurements [64] and taking into account that InP is a strong scattering material with respect to Si, values of thickness in the 300-350nm range are found to fully satisfy these conditions.

- All the Bragg diffraction peaks produced by the structured InP layer have to be reachable during the so-called rocking curve measurement, *i. e.*, which is obtained while keeping the detector fixed in one single position [More details in Section 3.3]. This restricts the angular distance between the InP and other compounds Bragg peaks and hence the maximum value of the lattice mismatch. The typical numerical aperture of the detector, which results from the detector dimension and the detector-to-sample distance, leads to lattice mismatches that have to be smaller than 3%.

- Symmetry is often a problem in a CDI experiment. Indeed, an object and its complex-conjugate centro-symmetric one are ambiguous solutions of the inverse problem because they produce the same diffraction intensity distributions. Hence, the design of the structured InP was made in order to avoid any vertical symmetry in the stack.

All those conditions drove the design of the ideal sample structure. We choose a stack structure composed by three (001) epitaxially grown layers, as schematically shown on Figure 3.1. The bottom InP layer is 100 nm thick and is in contact with the Si substrate. Just above, there is a 40 nm-thick $In_{0.57}Ga_{0.43}As$ layer, lattice-matched to InP. On top of them, there is a 200 nm thick InP layer. As bulk materials, the lattice parameters of the InP and InGaAs compound are 5.8687Å and 5.8858Å respectively. It corresponds to a lattice mismatch of about 0.29%. However, the InGaAs being lattice-matched to the InP layer, the accumulated strain in the

[2] Adhesive bonding (also referred to as gluing or glue bonding) is a wafer bonding technology which consists in applying an intermediate layer of metal or oxide to connect substrates of different materials.

InGaAs develops solely along the vertical axis, resulting in a vertical lattice mismatch of 0.56%, as measured with high-resolution X-ray diffraction using a laboratory source.

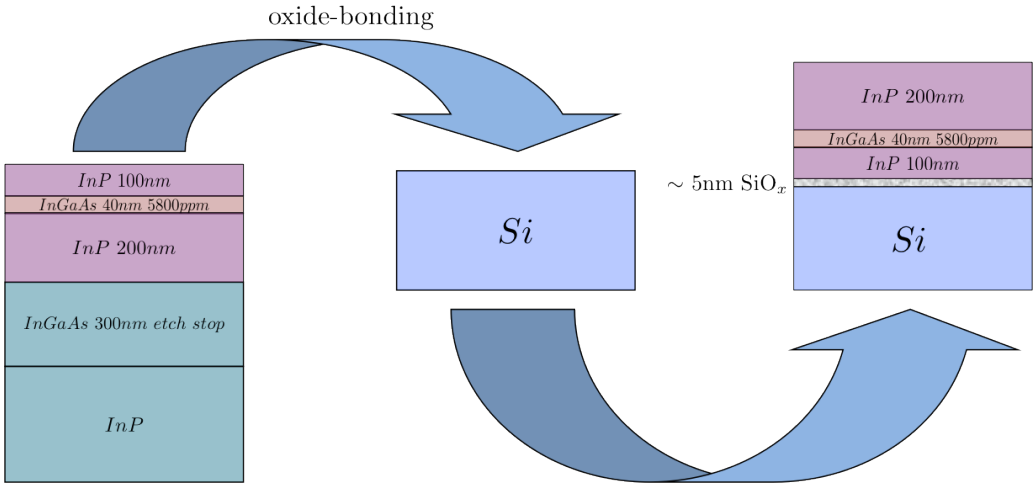

Figure 3.1: Oxide-bonding of the InP multilayer on Si and final structure of the thin film.

3.2.3 Preliminary characterization

The preliminary characterization aims at verifying the structural properties after the oxide-bonding procedure. High-resolution X-ray diffraction (XRD), scanning electron microscopy (SEM), atomic force microscopy (AFM), and transmission electron microscopy (TEM) investigations were performed to provide as much structural information as possible.

XRD measurements using a laboratory source

After its fabrication, the sample was characterized by X-ray diffraction using a laboratory source at the Cu K_α-edge and a Rigaku Smartlab diffractometer, delivering a beam size of $1.5 \times 3\text{mm}^2$. On Fig. 3.2 we can see the intensity distributions of the (004) Bragg reflection of the InP thin film, from an experimental (blue) and a distorted wave Born approximation model [83, 84] simulated (red) $\theta - 2\theta$ scan. The superposition of the two curves is showing the good agreement between the theoretical and measured values of the thickness and strain profile. Additionally, we can see that the removal of the indium phosphide substrate [See Fig. 3.1] didn't cause the relaxation of the strained InGaAs layer, which has maintained the deformation after the oxide-bonding - the peak positions along the $\theta/2\theta$ direction shows that the lattice parameters of the two layers did not change. It is given by

$$\text{lattice mismatch} \equiv \epsilon_{zz} = \frac{a_{InGaAs} - a_{InP}}{a_{InP}} \tag{3.2.1}$$

where a_{InGaAs} and a_{InP} are the lattice parameters along the 001 direction, extracted from the measurement and corresponding to the InGaAs and InP peak positions respectively.

Two dimensional cartographies of the reciprocal space in the vicinity of the (004) InP and Si Bragg reflections can be seen on Figs. 3.3a-3.3b on the next page. The small spreadings of the InP and InGaAs peaks with respect to the (004) Si peak, which as it can be seen on Fig. 3.4 (the two figures aren't scaled), are twice the value of spreading for Si in the θ direction - the perpendicular to the (004) crystal direction - reveal that the bonded layers are of relatively good quality, meaning that only a few defects or dislocations are expected in the InP/InGaAs stack.

Additional measurements allowed to measure the misorientation between the InP and InGaAs layers and the Si substrate which is expressed by the *twist* (γ) and *tilt* (β) angles [See Fig. 3.4].The

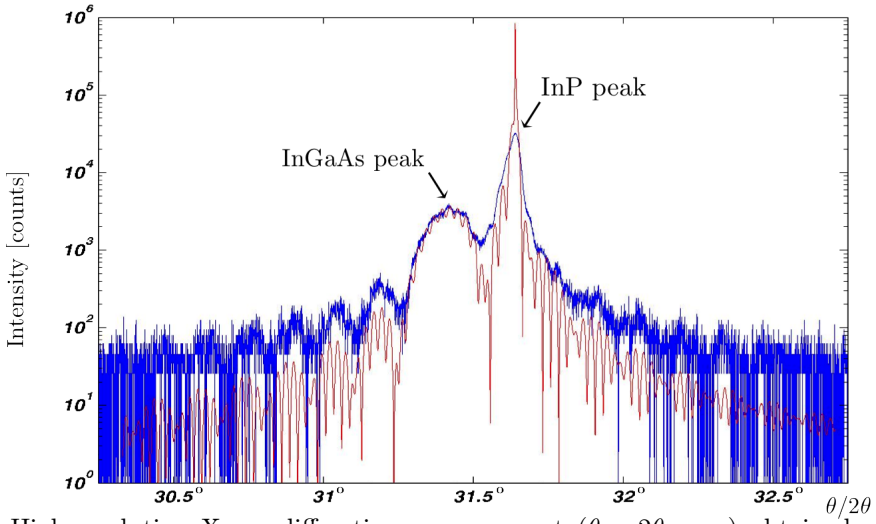

Figure 3.2: High-resolution X-ray diffraction measurement ($\theta - 2\theta$ scan) obtained at the (004) InP reflection.

tilt angle between the (004) latices planes of the film and the substrate, was found to be $\beta = 0.07°$, indicating that there is a very small inhomogeneity in the distribution of the SiO_x thin oxide layer, while the twist angle between the (220) planes was determined at $\gamma = 2.54°$.

SEM and AFM measurements

Further studying of the sample with SEM and AFM, supports some of the conclusions of the preliminary XRD analysis results. We can see on Fig 3.5a a SEM image of the sample surface in an area of $100\times130\mu m^2$, which contains four emerging dislocations, giving us an estimation of their density. It is believed that the dislocations start to appear inside the InP substrate and continue propagating into the InP and InGaAs layers until they reach the surface. After bonding the InP superlattice along with its substrate on silicon, remainders of the chemical removal of the InP substrate and InGaAs etch stop are left on the top of the 200nm-thick layer, forming a surface defect with the shape of a "chimney". That is what we see on the AFM image of Fig. 3.5b, taken around the emerging dislocation, which bulges approximately 230nm over the sample surface. In practice, these emerging dislocations will be encountered by a nano-sized beam quite rarely.

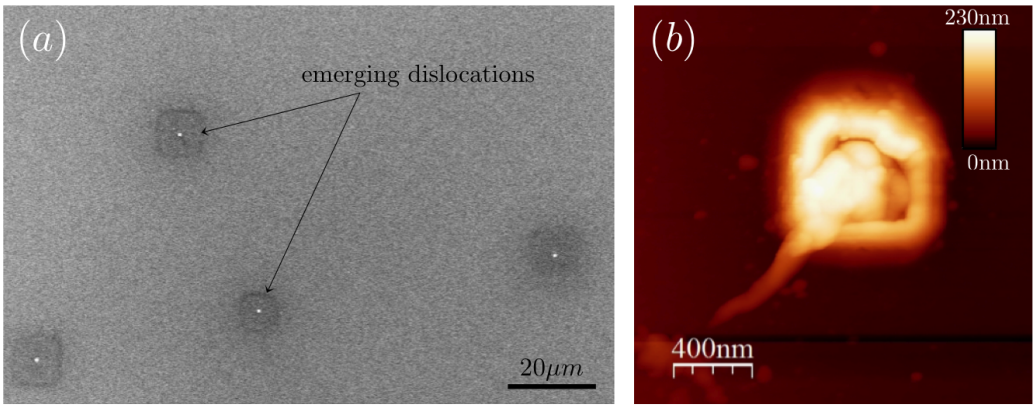

Figure 3.5: (a) Emerging dislocations on the surface of the thin film (SEM image). (b) One of the "chimey" shaped dislocations. We can see that the defect reaches 230 nm over the surface of the sample (AFM image).

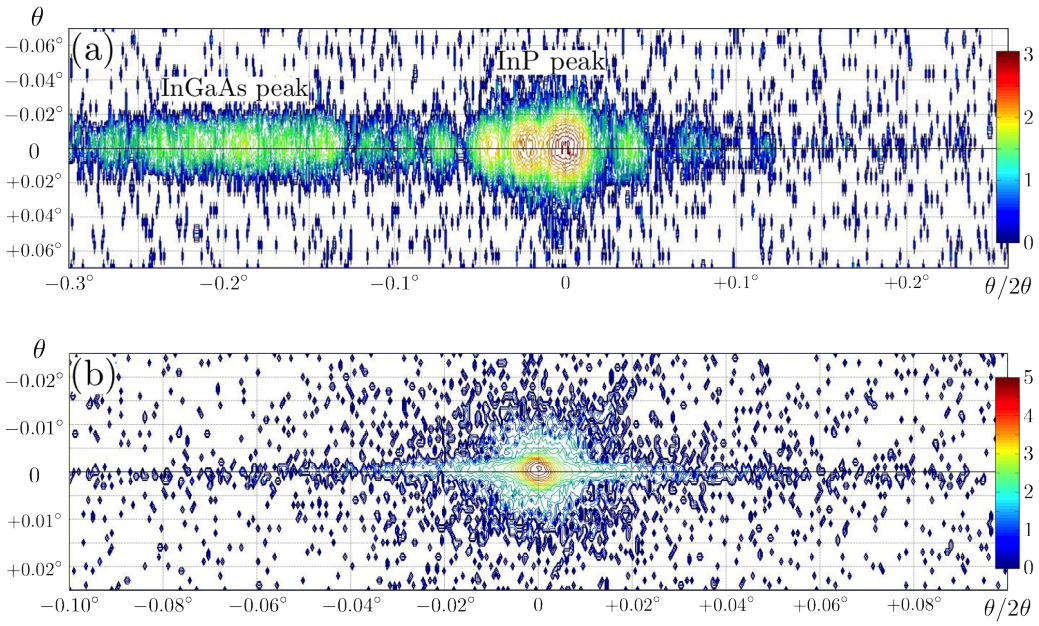

Figure 3.3: Two dimensional maps (a) In the vicinity of the (004) InP (right) and (004) InGaAs (left) Bragg reflections. The map is centered at zero with respect to the InP peak (logarithmic scale). (b) The Si substrate (004) Bragg reflection. The horizontal axis corresponds to the $\theta/2\theta$ direction and the vertical axis to the angle of incidence θ. The intensity scale is logarithmic in arbitrary units.

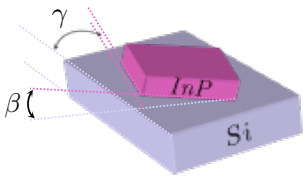

Figure 3.4: Representation of the misorientation angles (β and γ) of the oxide-bonded layer with respect to the Si substrate.

TEM-HAADF

Scanning TEM measurements were performed using a TEM/STEM FEI Titan Themis device in the HAADF mode. This mode allows to get sensitivity to the chemistry of the imaged crystalline material. For the TEM investigation, one requires the thinning down of the sample to a few hundreds of nanometers. Hence, this destructive characterization was performed after the Bragg ptychography experiment, on the sample part corresponding to the one investigated with Bragg ptychography. The InP/InGaAs interface, as well as the InP/Si interface can be seen on Figures 3.6b and 3.6c respectively, and they demonstrate a certain degree of roughness. (0.03Å of displacement over a period of 5nm-10nm). Some chemical inhomogeneities are observed in the oxide layer (Fig. 3.6c).

In TEM, the electron beam undergoes Bragg scattering in the case of crystalline materials, therefore TEM is sensitive to the structural properties of crystals and can be used as a relevant comparison tool to Bragg ptychography. For this purpose, the sensitivity of this TEM measurement with respect to the crystalline properties has to be carefully evaluated. We are particularly interested by lattice mismatch and tilts, physical parameters that can be obtained with geometric phase analysis [85].

With this approach, the tilt map r_{xz} is extracted (Fig. 3.7b). It presents visible undulations, mainly induced by the movements during the STEM scan. From the amplitude of the undula-

tions, the sensitivity of the STEM-HAADF experiment to the lattice tilts was estimated to be approximately $\pm 0.5°$. Thus, any inferior value cannot be detected with the current setup.

In Fig. 3.7a, the lattice mismatch ϵ_{zz} at the InP/Si interface is shown. It demonstrates the complete relaxation of the bonded layer with respect to Si, which is supported by the fact that there is no gradient appearing close to the bonding interface. The expected lattice-mismatch value of 8.1% along the (001) direction is found, together with some fluctuations. These latter ones allow to estimate the lattice mismatch uncertainty to about $\pm 0.3\%$.

In conclusion, the oxide-bonded InP/InGaAs thin film shows the expected crystalline quality in terms of structure, thickness and lattice mismatch values. Moreover, small inhomogeneities in the distribution of the Si oxide layer were observed while the entire film does not contain many defects or dislocations. Furthermore, the uncertainty of the preliminary characterization experiments was carefully evaluated, in order to allow for a relevant comparison between the features, the Bragg ptychography measurements and the obtained reconstructions.

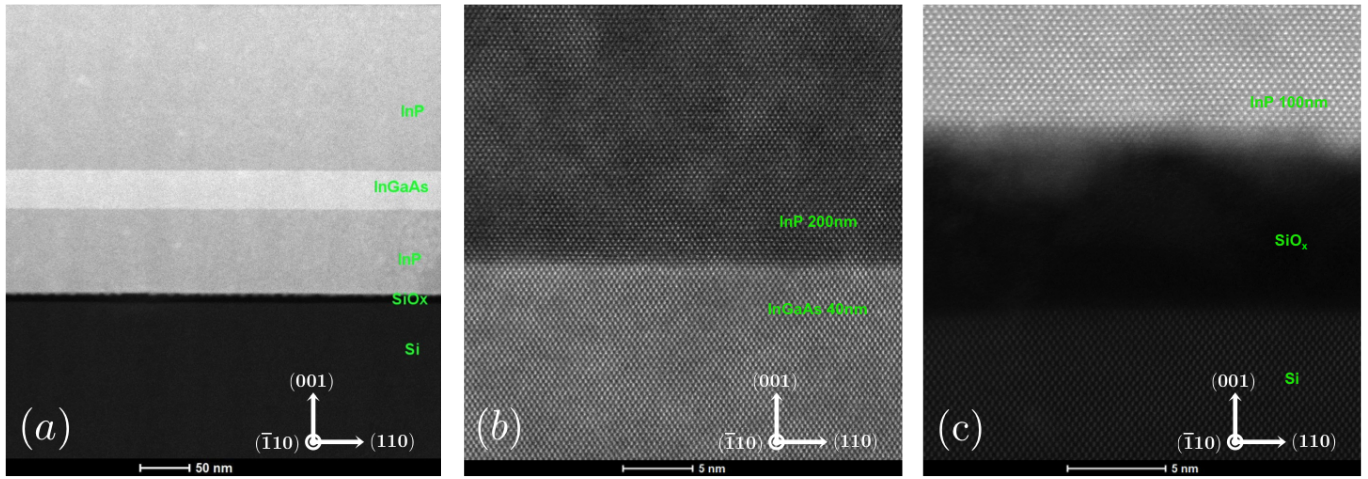

Figure 3.6: (a) Cross-section along the thickness direction, which coincides with the (001) crystal growth direction. (STEM/HAADF image, chemical contrast) (b) The top InP/InGaAs interface layers as seen with TEM. (c) The 100nm-thick InP bonding interface with Si (TEM). The dark intermediate area corresponds to the amorphous Si oxide.

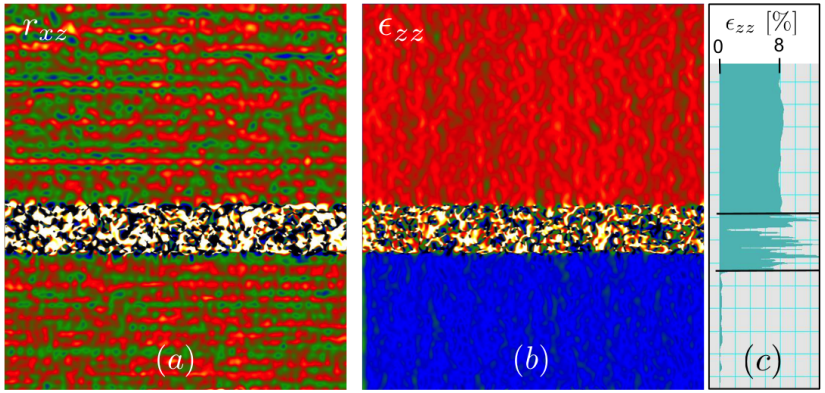

Figure 3.7: Quantifying STEM sensitivity. (a) HAADF mode view of the InP/Si interface. (b) Rotation r_{xz} and (c) strain ϵ_{zz} maps obtained from (a) using geometrical phase analysis. The color scale in (b) goes from -0.5° to $+0.5^\circ$, while in the inset of (c), the 1D cross section of ϵ_{zz} along z exhibits fluctuations of about ± 0.3 %.

3.3 Bragg ptychography experiment

3.3.1 Experimental setup

The coherent X-ray diffraction experiment was performed at the ID13 beamline of the European Synchrotron Radiation Facility (ESRF). The hard X-ray undulator beam is monochromatized by a channel-cut Si (111) monochromator to a photon energy of 14.9keV (λ=0.83Å, $\delta\lambda/\lambda \approx 10^{-4}$). The beam is pre-focused by a set of refractive Be lenses. The experimental setup geometry is schematically represented on Figure 3.8. For the characterization, the beam is focused down to a sub-micrometric size with dedicated focusing optics placed on the same granite table as the sample stage. The detector is on a separate stage, decoupled from the sample motions for maximal stability. More details about the experimental setup can be found in Ref. [86]. The details of the Bragg ptychography experimental setup elements are described below.

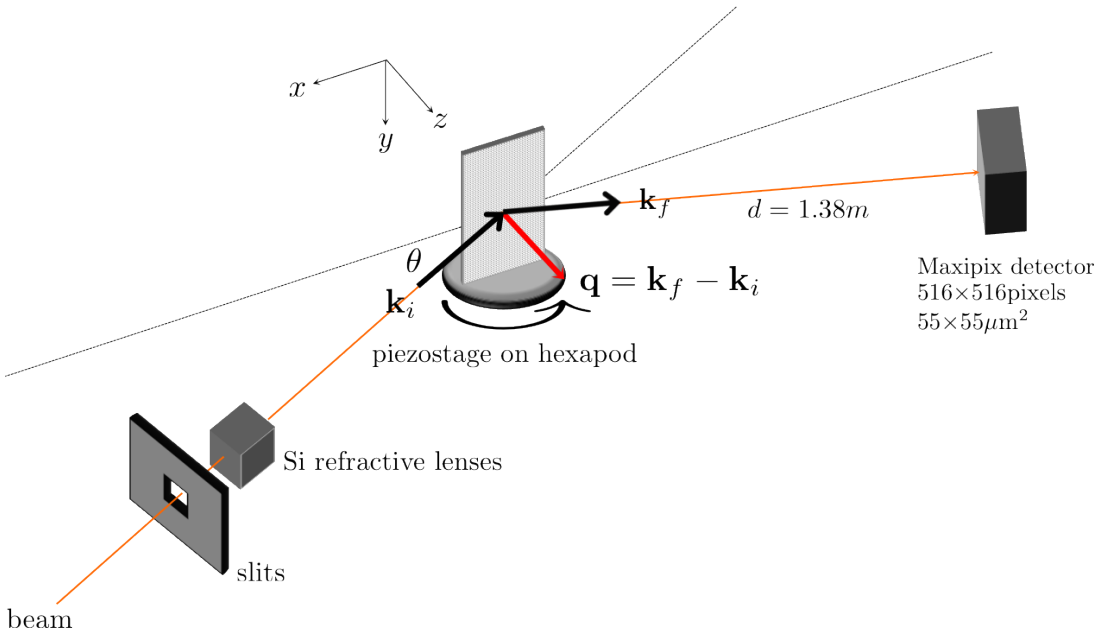

Figure 3.8: Experimental setup, focusing optics, sample holder and positioning, 2D detection.

The sub-micrometric beam: the finite beam-sized is produced by a set of focusing refractive Si lenses, with a focal length of about 1cm. The entrance aperture was reduced with a set of slits to 60x64μm^2 in the vertical (V) and horizontal (H) directions, so that the illumination area matched approximately the beam transverse coherence lengths.

Prior to the Bragg ptychography experiment, a detailed characterization of the beam profile was performed. In order to obtain the complex-valued illumination function at the focal plane, a lensless microscopy method was used inspired by Ref. [51] and discussed in Ref. [64]. It is based on the simple and fast measurement of the over-focused direct beam intensity pattern performed with a high resolution camera. This allows a high oversampling of the diffraction pattern, which exhibits fine features such as interference fringes resulting from the Fresnel propagation of the coherent wavefront truncated by the slits defining the lens aperture (Fig. 3.9a). To this aim, a PCO camera with pixel size of approximately 1.9μm was used, located at a distance of 1.81m from the focal plane. The measured intensity data was inverted with our phasing routine before the beam was back-propagated down to the plane corresponding to the sample position. As expected from the Gaussian absorption profile of the refractive lenses, the beam profile behaves closely to a Gaussian function with however some weak secondary maxima visible on both horizontal and vertical sides of the central spot (Fig. 3.9b).

The size of the amplitude main lobe was estimated to be $270 \times 240nm^2$ (VxH) for a corresponding full-width-at-half max (FWHM) of the spot intensity of $60 \times 55nm^2$ (VxH). However, in the Bragg diffraction geometry the sample is inclined with respect to the incoming beam direction, leading to a beam footprint of about 950×270 nm^2 along the projection and perpendicular directions, respectively. It corresponds to a FWHM spot intensity of $220 \times 60nm^2$. The knowledge of those values is of major importance for defining the ptychography step-size.

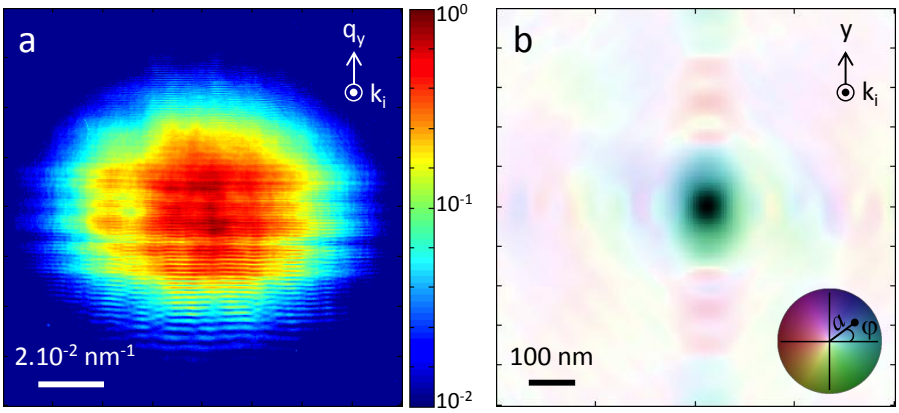

Figure 3.9: Retrieved beam profile. (a) Coherent intensity pattern of the overfocused beam (arbitrary units) measured with a Frelon camera. (b) Color rendition of the complex-valued beam profile, retrieved from the inversion of (a) and shown in the plane corresponding to the sample position. The brightness and color correspond to the beam linear scale amplitude and to its phase ϕ respectively.

The sample stage: the sample stage has to be stable at the nanometer scale and over the duration of the data acquisition and has to allow for the investigation of both reciprocal and direct spaces. The ID13 stage is composed by a three-axis piezoelectric nanostage, allowing for the translations along the x, y and z directions as seen on Figs. 3.8 and 3.11. It is mounted on the top of an hexapod, which ensures the rotation of the sample with accuracy in the 10^{-3} degree range. The center of rotation of the stage is first aligned with the focal plane using a gold cross pattern. Once it is found, the sample is brought to that position with the help of of an optical microscope, whose focal depth is about $1\mu m$.

For our experiment, which involves a planar sample to be placed vertically with respect to the diffraction horizontal scattering plane, a specific glass-made sample holder was made. It has to fit in the given space dimensions and was fixed on the piezostage with wax. This sample holder was found to present excellent stability.

The detection stage: In the ID13 beamline the detector is placed in the horizontal plane onto a homemade rotation-translation trail [See Fig. 3.10]. This original setup allows to investigate a large range of diffraction angles (between $\approx 15°$ and $50°$), for a detector-to-sample distance varying from 1 to 3.5m. The coherently scattered far-field intensity patterns are collected with a Maxipix pixel array of 516×516 pixels, with pixel size of $55 \times 55\mu m^2$ [87].

3.3.2 Data acquisition

For the acquisition of the Bragg ptychography dataset, the sample was oriented so that the InP (004) Bragg condition was met (Bragg angle $\theta_B = 16.38°$), successive acquisitions of 2D intensity patterns were measured by scanning the sample over an 11×9 position grid along x and y, and repeating this raster scan at each angle along the rocking curve (180 frames with angular step of $\delta\theta = 0.003°$). The desired redundancy in the dataset was obtained thanks to the important

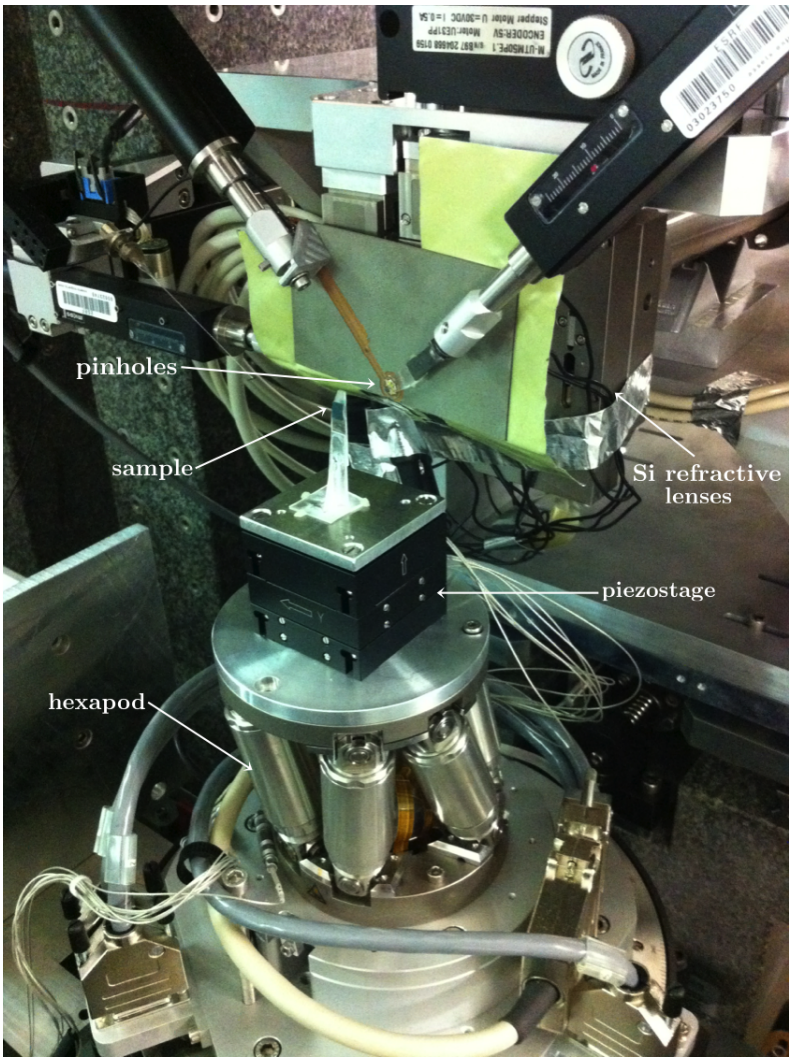

Figure 3.10: Experimental setup at the ID13 beamline. Photograph of the sample on the glass holder, fixed on the piezostage on the top of the hexapod.

overlapping amount of the successive beam positions ($\approx 80\%$), which was ensured by using step sizes of 150nm and 50nm along the x and y directions respectively.

The detector was located 1.38m away from the sample to ensure the oversampling of the signal. In order to avoid saturation of the detector at the highly intense InP Bragg peak, the exposure time was set to 0.2 s per frame, taking three frames at each position for increasing the intensity dynamical range.

As derived in Chapter 2, the detection modality results in a nonorthogonal measurement reference frame [See Fig. 3.11], which is kept in order to preserve the photon shot noise statistics. With the given scanning parameters, the following elemental reciprocal space values are found: $\delta q'_x = 2.2293 \times 10^6 m^{-1}, \delta q'_y = 2.9300 \times 10^6 m^{-1}, \delta q'_z = 3.0538 \times 10^6 m^{-1}$. While the detector frame corresponds to a $516 \times 516 \times 180$ matrix, the relevant volume, into which we observe a useful signal, can be restricted to a $516 \times 100 \times 180$ matrix. According to the Fourier conjugation relations, this reciprocal space volume corresponds to a certain DS pixel size. However, as the corresponding pixel size is not commensurable with the illumination function scanning steps, we encountered visible artifacts on the amplitude of the reconstructed object, which we managed to considerably reduce by appropriately adjusting the size of the illumination matrix. The latter was chosen so that the illumination function scanning steps correspond to an integer number

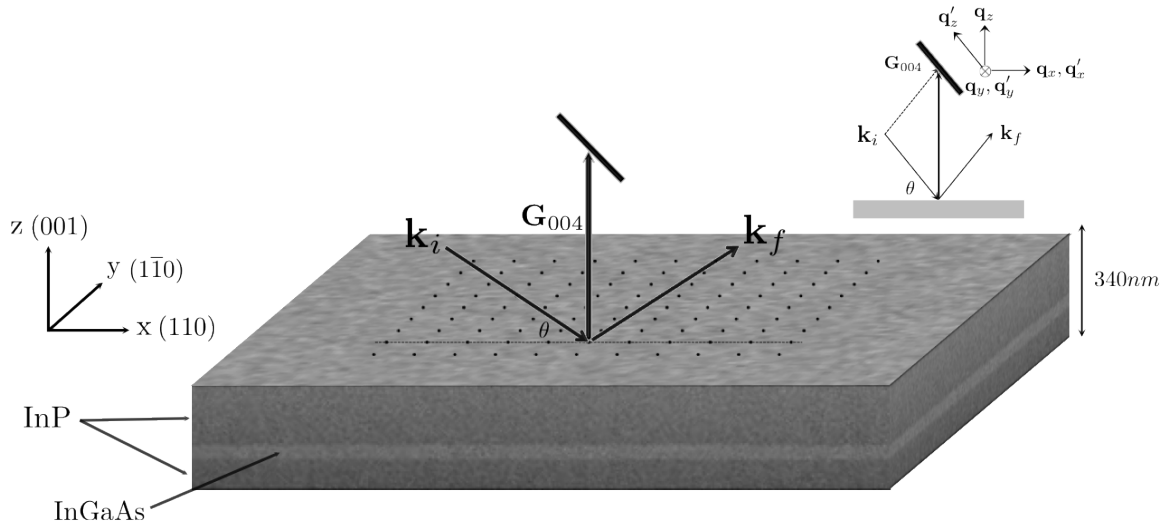

Figure 3.11: Sample and data collection geometry. The different DS and RS reference frames are depicted as well.

of pixels in DS. The smallest matrix volume that meets this requirement has size of 542 × 130 × 190 pixels. It leads to a tilted associated conjugate direct space, which is considered for the inversion ["natural" and "laboratory" frame as explained in Subsection 2.2.4]. Here the sampling in reciprocal space yields to an non-orthogonal direct space, whose pixel size is $\delta x' = 1.5462 \times 10^{-8} m, \delta y' = 1.6496 \times 10^{-8} m, \delta z' = 3.9566 \times 10^{-9} m$, resulting to an orthonormal space pixel size of $\delta x = 1.5462 \times 10^{-8} m, \delta y = 1.6496 \times 10^{-8} m, \delta z = 8.6673 \times 10^{-9} m$.

After the measurement the data was manually imported. The background was quantified after acquiring several measurements of the dark, but not subtracted from the raw data, and the hot or damaged pixels of the CCD detector were masked [See Fig. 3.12].

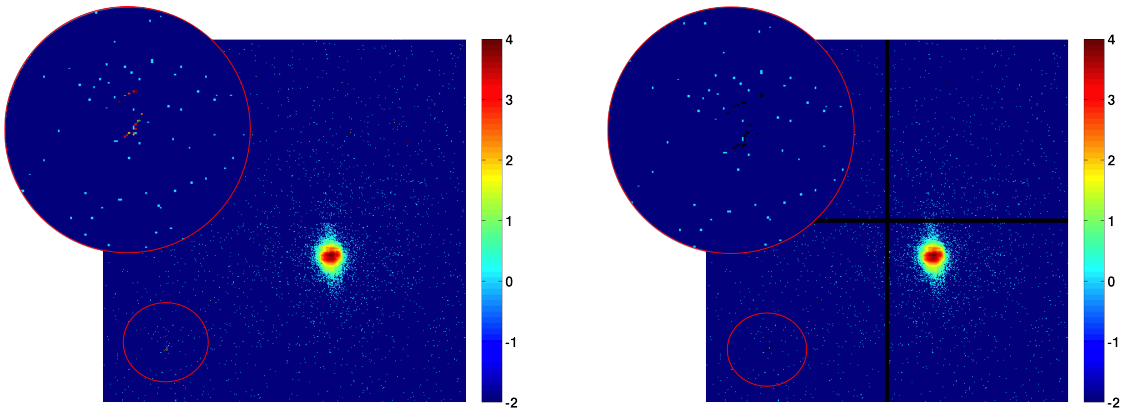

(a) (b)

Figure 3.12: (a) Raw data from the Maxipix CCD. (b) The masked data. The *black* cross is a result of the distance between adjacent chips (4 in total) and which contains no pixels. The *black* colored pixels correspond to hot pixels and have been manually removed. The captured frame corresponds to the (004) InP peak measured the *rocking curve* for the 3D spanning of RS.

3.3.3 Experimental set-up stability

As previously discussed, the quality of the ptychography dataset highly depends on the stability of the experimental setup, which directly affects the beam-to-sample positioning accuracy. For this reason, we have carefully checked the stability of the setup on short and long time scales. Figures 3.13a to 3.13c correspond to three frames acquired at the very same sample position and for the same incidence angle, corresponding to the InP (004) peak. The only visible differences are limited to the low count intensity pixels, as expected from the photon shot noise process, and even if we calculate the centroids of the intensity distribution (x_c, y_c), we can see that all three values correspond to the exact same pixel on the detector [See Table 3.1].

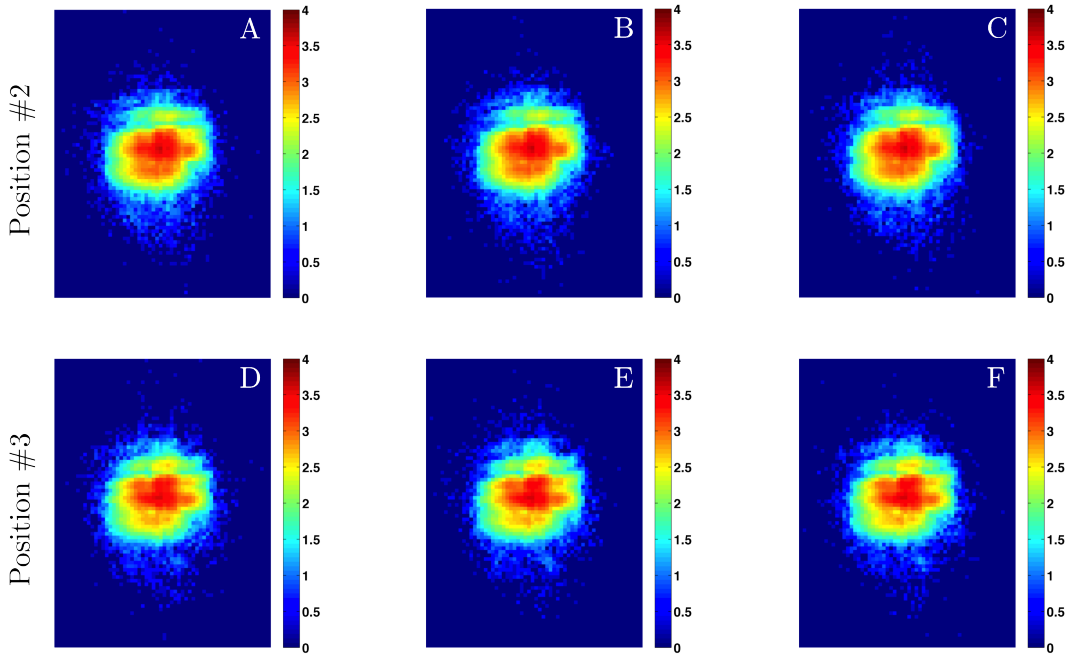

Figure 3.13: Diffraction patterns at two adjacent scan positions. From A to C, three acquisitions at a fixed beam-to-sample and incident angle position. From D to F, same measurements performed at the next beam-to-sample position. The incident angle corresponds to the Bragg condition for the (004) InP planes.

The frames 3.13d to 3.13f which are again very similar one to the other, correspond to the next scan position. They have been measured right after the three ones above. Clear differences between these two data groups are observed, even in the high count intensity pixels. The same information is valid when examining the InGaAs peak at the same positions [See Figs. 3.14a-3.14f]. The comparison of these diffraction patterns gives us two major pieces of information: the stability of the setup and the existence of structural fluctuations within the sample from one beam position to the other. Finally, the smooth evolution of the 3D diffraction patterns, which is observed as a function of the beam-to-sample position while the 3D patterns result from the stacking of 2D data obtained at very different times, demonstrate the high stability of the setup during the total time of the experiment. [See Fig. 3.18]

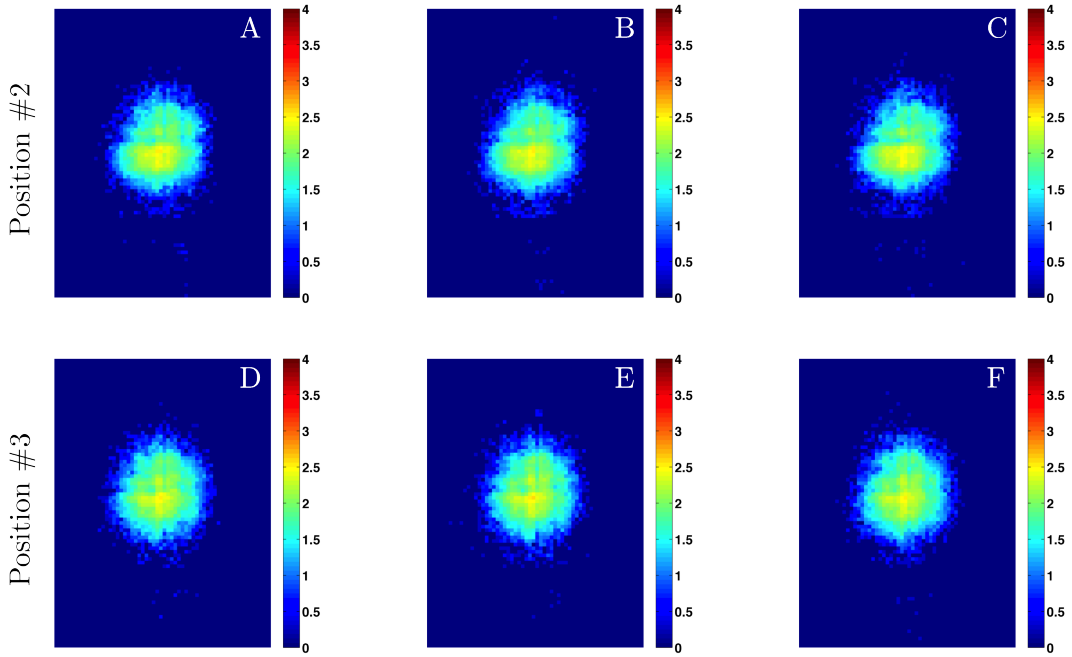

Figure 3.14: Diffraction patterns at two adjacent scan positions. From A to C, three acquisitions at a fixed beam-to-sample and incident angle position. From D to F, same measurements performed at the next beam-to-sample position. The incident angle corresponds to the Bragg condition for the (004) InGaAs planes.

	Position #2			*Position #3*		
	Frame	x_c	y_c	*Frame*	x_c	y_c
InP peak						
	A	49.63	59.95	D	49.60	58.66
	B	49.63	59.96	E	49.61	58.57
	C	49.64	59.88	F	49.59	58.55
InGaAs peak						
	A	50.67	59.60	D	50.65	58.25
	B	50.75	59.39	E	50.61	58.15
	C	50.66	59.56	F	50.64	58.21

Table 3.1: Centroids (coordinates x_c, y_c) of the diffraction patterns at two adjacent scan positions [See Fig. 3.18], extracted for the InP and InGaAs peaks.

3.3.4 Radiation damage

The onset of eventual radiation damage was tracked by monitoring the diffraction signal at a fixed illumination position for a total acquisition time of 50 min. This duration corresponds

approximately to the total illumination time of a single position in the Bragg ptychography experiment. To this aim, a Frelon camera was used, located at a few 0.1 m from the sample. In Fig. 3.15a, we can see the integrated intensity over the different angles of incidence of the X-ray beam. Whenever the Bragg condition is met a peak appears on the detector, and summing up all the collected frames results to the final image.

The detection frame exhibits some of the neighboring (004) Bragg peaks for the InP and InGaAs layers, as well as the Si substrate. The first order harmonics of the forward beam are also visible, while the central spot is blocked by a beam stop, to avoid signal saturation. The intensity corresponding to the InP and InGaAs Bragg peak (red rectangle in Fig. 3.15a) was integrated and plotted as a function of time in Fig. 3.15b while we rotate the sample for each 1sec-frame along the rocking curve. We can see that except from the fluctuations of the Bragg peak maximum, there is no visible decrease of the signal, and thus radiation damage can be considered negligible.

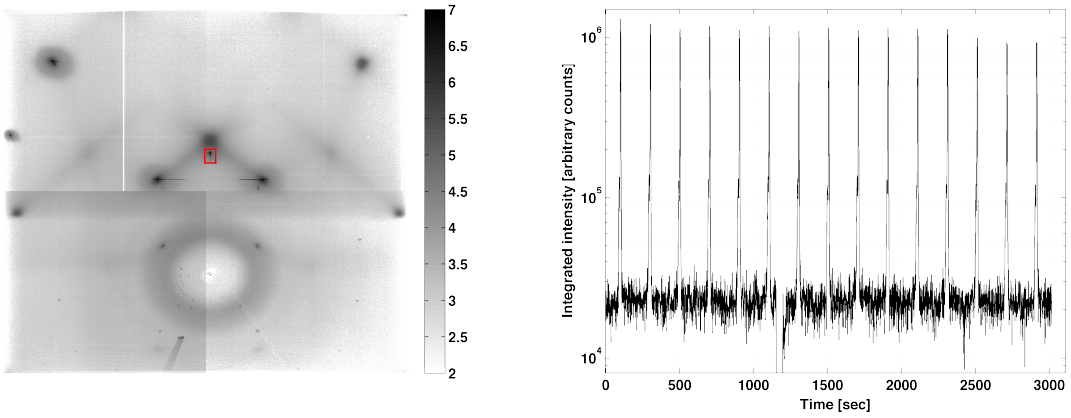

(a) (b)

Figure 3.15: (a) Intensity pattern resulting from the integration of the large and small angle scattering signals observed during successive scans of the incident angle [log scale]. (b) Evolution of the intensity during the same scan, integrated inside the red dashed area of the detector (both InP and InGaAs peaks). We can see that the intensity has the shape of a $\theta-2\theta$ scan, since we rotate the sample for each 1sec-frame.

3.4 Bragg ptychography data analysis

Before attempting the inversion of the data for the 3D imaging of the sample crystalline structure, a careful analysis of the collected data is performed. As we will see, this step already allows to evidence some structural features, that are contained in the dataset.

3.4.1 The measured diffraction pattern at a fixed illumination position

Figure 3.16a presents the 3D intensity distribution corresponding to the signal acquired along the rocking curve for a fixed beam-to-sample position. This is represented in an orthogonal space for sake of clarity, the q_x axis being parallel to the sample surface, q_y being on the surface plane as well but perpendicular to q_x, and q_z being parallel to the sample's (001) crystalographic direction [See Fig. 3.11]. Both InP and InGaAs peaks are well visible with their reciprocal space separation corresponding to the expected 0.56 % of lattice mismatch. Along q_z, thickness oscillation fringes are observed related to the different layer thicknesses. The high-frequency fringes are associated to the InP layers while the low-frequency ones are associated to the much thinner InGaAs layer. Along the thickness direction $\mathbf{q}_z$, the InGaAs peak is broader than the InP peak as an expression

of the expected peak broadening resulting from size effects. We point out that all reciprocal space features look tilted in the (q_x, q_z) plane. This shape is a consequence of the shape of the illuminated volume which contributes to the diffraction pattern and is inclined by θ_B with respect to the laboratory frame.

On the 2D cut shown in Fig. 3.16b, we can see the intensity distribution in the vicinity of the InP and InGaAs Bragg peaks. This representation confirms that all features are sufficiently oversampled, as the high-frequency interference fringes can be clearly separated. At the maximum intensity level, which is at the InP Bragg peak, the intensity reaches $\sim 10^4$ photons/pixels. Finally, it is interesting to note that the shown 3D and 2D patterns present a regular behavior, underlining once more the good quality of the data with respect to experimental instabilities.

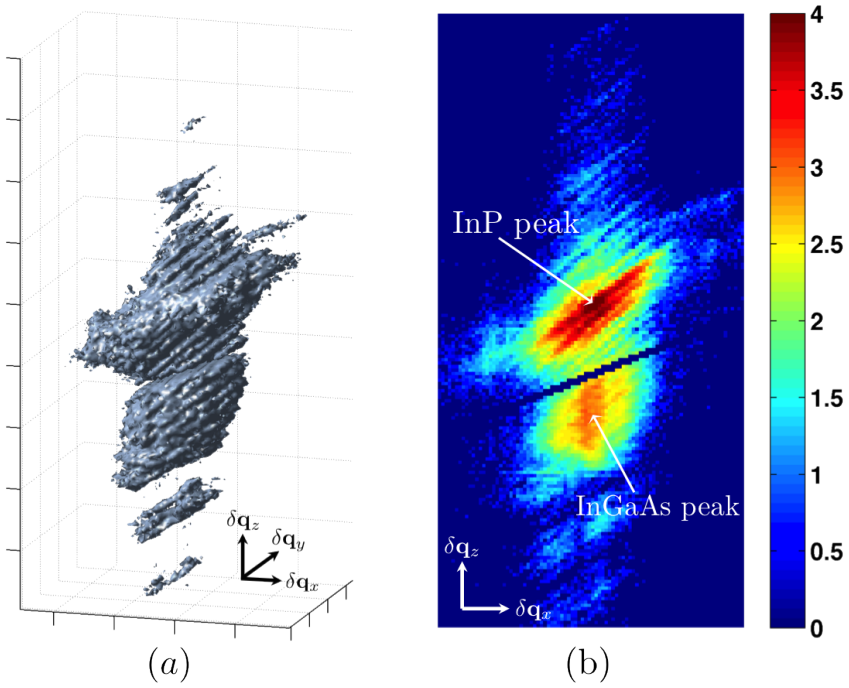

Figure 3.16: (a) Measured 3D pattern of the (004) Bragg reflection. (b) Slice of the 3D pattern. ($\delta q_x = 0.1022nm^{-1}, \delta q_y = 0.0120nm^{-1}, \delta q_z = 0.1055nm^{-1}$)

3.4.2 Comparison with the expected structural model

As a first step in our analysis, we compare this experimental 3D pattern with the expected one. The 3D intensity calculation is performed using structural parameters according to the nominal values of the sample structure. The 3D illumination function is derived from the experimentally retrieved one, presented previously in Fig. 3.9b. The physical models used for the describing the sample/beam interaction and the propagation of the resulting wavefront up to the detector plane were already described in Subsection 2.2.4. As a result, the measured diffraction pattern is the square modulus of the Fourier transform of the product of the crystal electron density and the illumination function. As this calculation is straightforward to perform, we decided to give all the related details in the next chapter, along with the description of the numerical analysis works.

However, we like to underline that the comparison between the experimental intensity patterns and the expected ones is of great importance for understanding the nature of the observed features on the diffraction patterns. This should be systematically attempted, when a relevant structural model exists.

The result of this simulation is shown in Fig. 3.17. On the whole, the obtained intensity distribution agrees well with the previously shown experimental measurements. The two Bragg peaks are obtained at their expected relative positions, the thickness fringes and the inclined shape of the patterns are reproduced as well. However, while the simulated InGaAs peak shape agrees well with its experimental counterpart, strong discrepancies are observed on the InP peak extent. They necessarily arise from structural distortions whose presence is further confirmed.

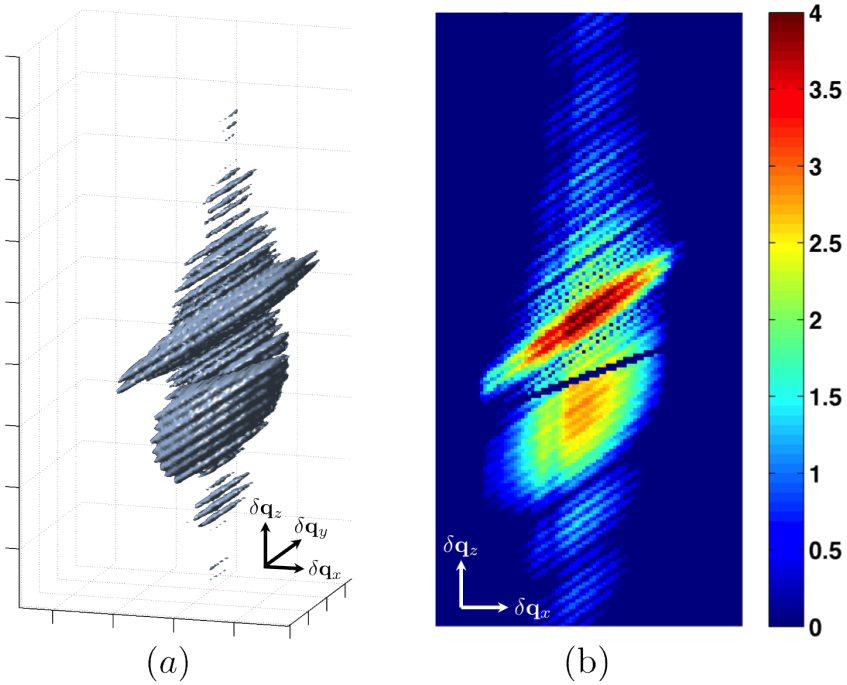

Figure 3.17: (a) Simulated 3D pattern of the (004) Bragg reflection. (b) Slice of the 3D pattern. ($\delta q_x = 0.1022nm^{-1}, \delta q_y = 0.0120nm^{-1}, \delta q_z = 0.1055nm^{-1}$)

3.4.3 Spatial fluctuations in the structural properties

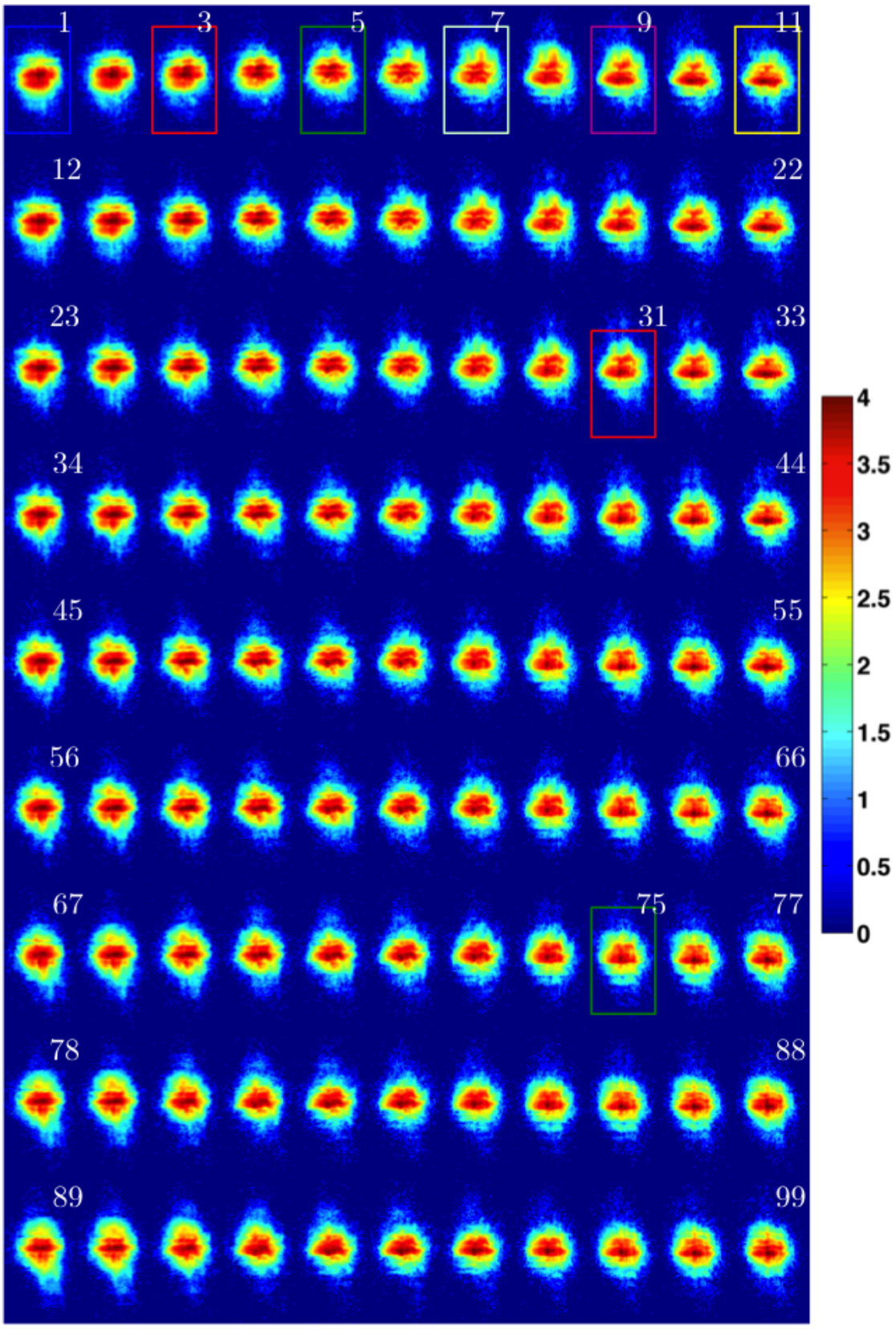

Figure 3.18: Measured diffraction patterns at Bragg condition for the (004) InP crystallographic planes.

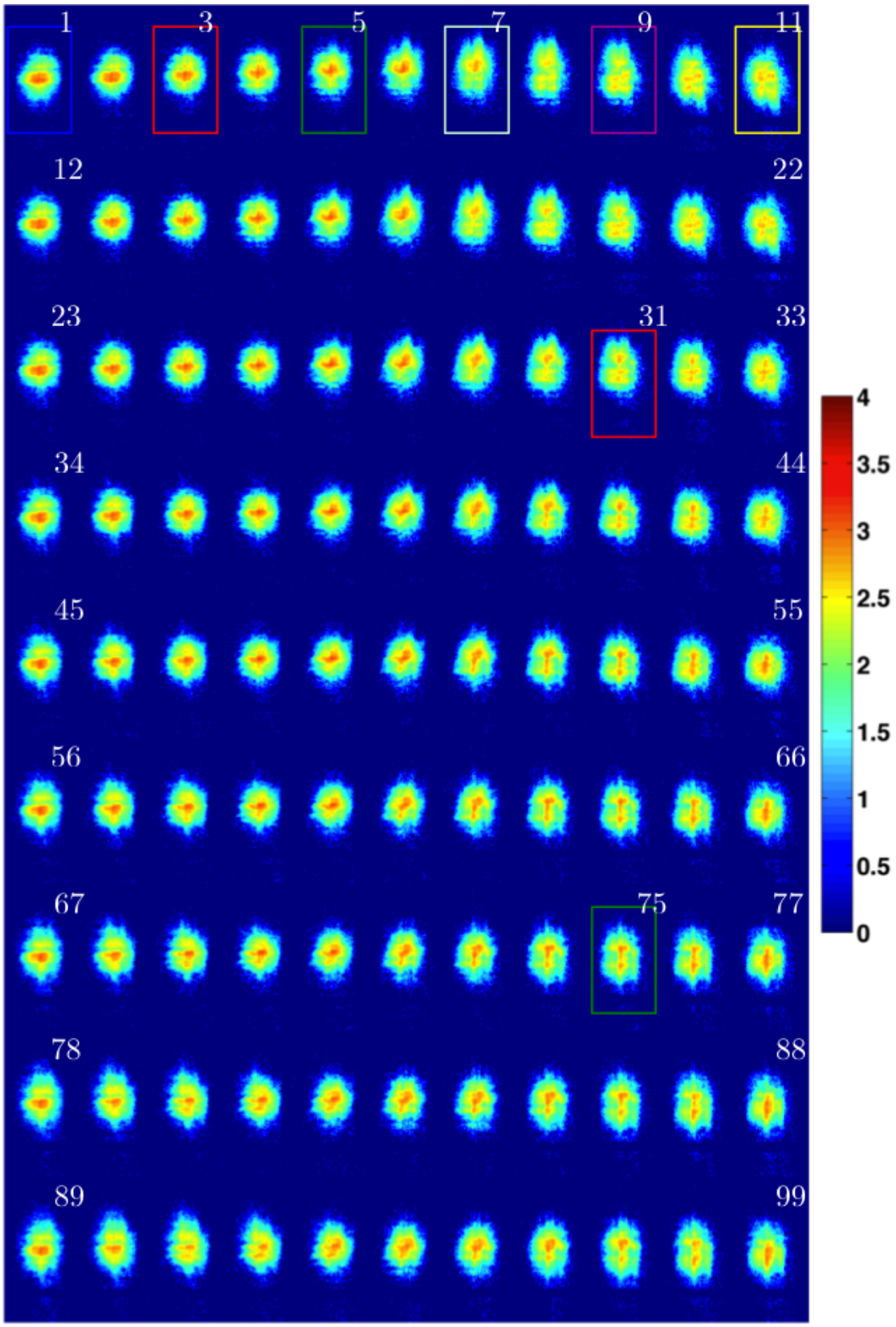

Figure 3.19: Measured diffraction patterns at Bragg condition for the (004) InGaAs crystallographic planes.

We now look at the spatial dependency of the intensity patterns. Fig.3.18 and Fig.3.19 present the intensity distributions measured in the vicinity of the InP and InGaAs Bragg peaks respectively, shown in the detector plane and as a function of the beam-to-sample positions. The horizontal axis corresponds to scanning the sample along x, that is on the plane of incidence, while the vertical axis corresponds to the direction parallel to y that is perpendicular to the plane of incidence. As we can see, the shape, position and main characteristics seen on the diffraction patterns, change smoothly along the line of the scan, as the sample is moved in the direction of the beam footprint. The vertical position of the peak is visibly changing as we scan the sample with respect to the beam. The calculation of the centroid for each of the diffraction patterns clearly emphasizes those fluctuations [Figs. 3.20].

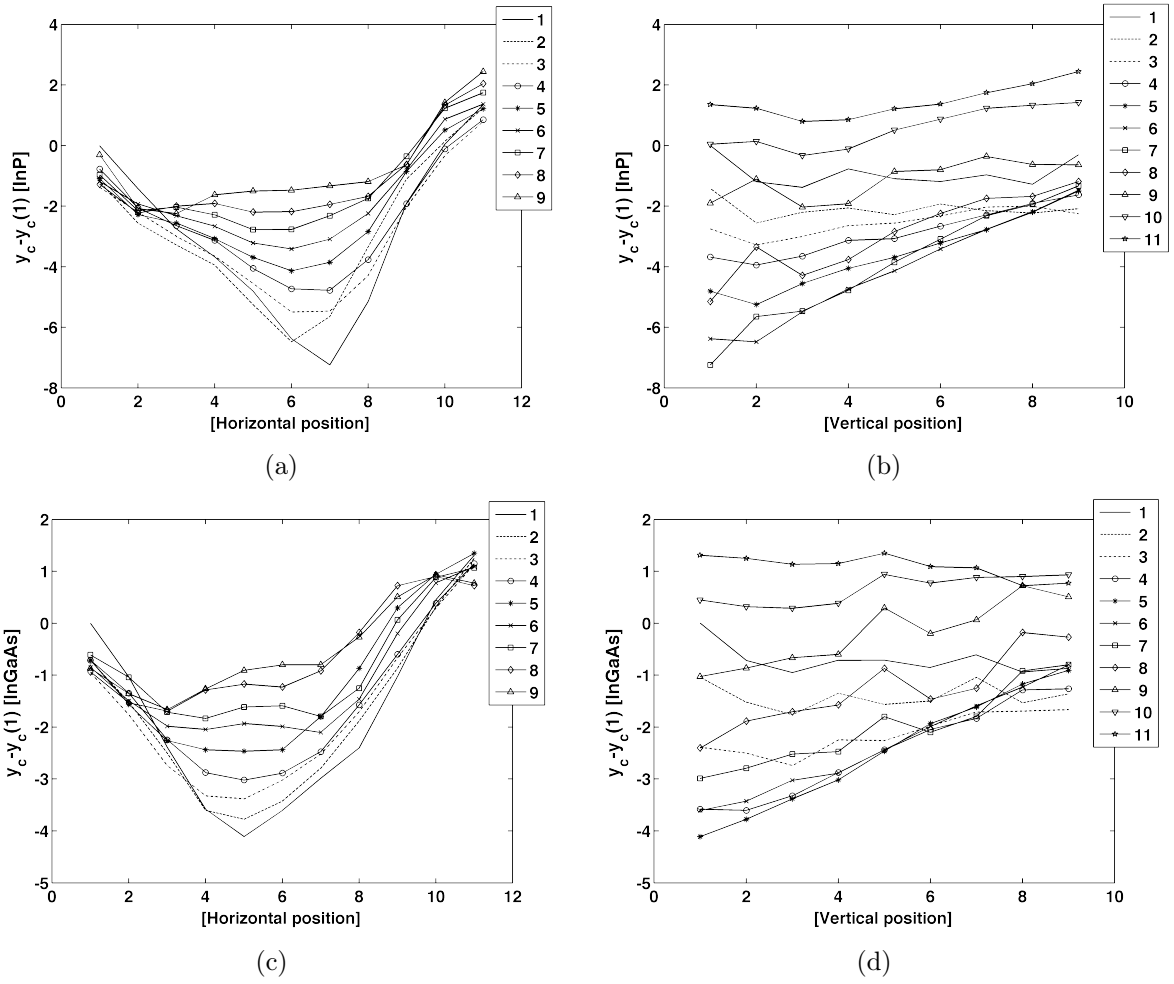

Figure 3.20: Diagrams of the relative distance of the InGaAs and InP diffraction patterns centroids, with respect to the centroid of the first diffraction pattern. (a) Δy_c for the InP diffraction patterns as a function of the column number of the ptychography scan. (b) Δy_c for the InP diffraction patterns as a function of the line number of the ptychography scan. (c) Δy_c for the InGaAs diffraction patterns as a function of the column number of the ptychography scan. (d) Δy_c for the InGaAs diffraction patterns as a function of the line number of the ptychography scan.

In addition to the changing position and extension of the diffraction patterns as a function of the beam positions, we can also observe a splitting of the InP peak along q_x for several diffraction patterns, as the one located in the top-right part of the ptychography XRD maps. This splitting is even more readily seen on the InGaAs Bragg peaks, resulting in an separation of the peak along the q_x direction. It is shown on Fig. 3.21b, indicated by the black lines. Along this direction, the

splitting suggests the presence of tilted crystallographic planes, whose tilt value can be calculated according to:

$$\frac{\Delta q_x}{2} = |\mathbf{G}_{004}| \tan(\phi/2) \Rightarrow \phi = 2 \tan^{-1}\left(\frac{\Delta q_x}{2|\mathbf{G}_{004}|}\right) \tag{3.4.1}$$

where $\Delta q_x = (9.5 \pm 1.7) \times 10^6 m^{-1}$, and $|\mathbf{G}_{004}| = 4.2578 \times 10^{10} m^{-1}$. Hence, the value of ϕ is estimated to be between 1.2×10^{-2} and 1.8×10^{-2} degrees, among the different positions of the ptychography scan.[3]

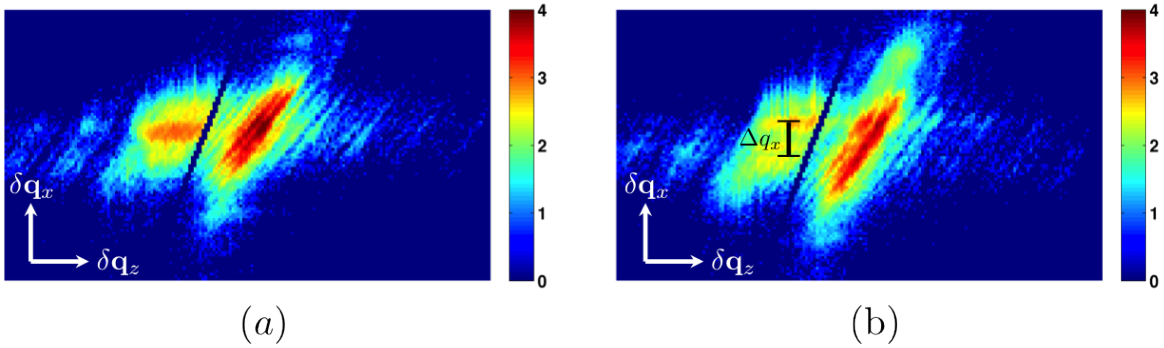

Figure 3.21: Intensity patterns represented on the orthogonal RS frame of the (004) Bragg reflection at (a) position 5 and (b) position 31 of the ptychography scan. ($\delta q_x = 0.1022 nm^{-1}, \delta q_y = 0.0120 nm^{-1}, \delta q_z = 0.1055 nm^{-1}$)

Another presentation of the dataset allows to bring interesting comparison elements. Figure 3.22 shows q_z scans extracted from the 3D diffraction patterns at the center of the Bragg peaks, for 6 beam-to-sample positions corresponding to the numbers shown on Figs. 3.18-3.19. These cuts allow to estimate the variations of the InP/InGaAs lattice mismatch, which are found to be negligible: the Bragg peak positions are not changing when different sample regions are probed. However, strong intensity variations can be seen between different positions. Interestingly, those fluctuations do not follow the same trends at the InP and InGaAs peaks (see for instance positions 5 and 9). Hence, the origin of the fluctuations on the intensity level can not be attributed to some regular decay in the measured intensity (like the one induced by the intensity current in the synchrotron ring). It is a consequence of the spreading of the InGaAs Bragg peak observed on some specific locations along the sample, due to the presence of structural inhomogeneities in the sample. Finally, we show in Fig.3.23 some 3D representations of the experimental intensity patterns measured at three different positions of the ptychography scan. Here again, we observe that the main distortions observed from one pattern to the other, appear as a spreading of the InGaAs peak mainly along the q_x and q_y directions.

[3]The tilt value presents fluctuations which have to do with the fact that at different scanning positions around the irregular phase feature, we see different amounts of the peak splitting. In addition, by geometrically estimating the distance we can assume some uncertainty of one or two pixels for every calculation.

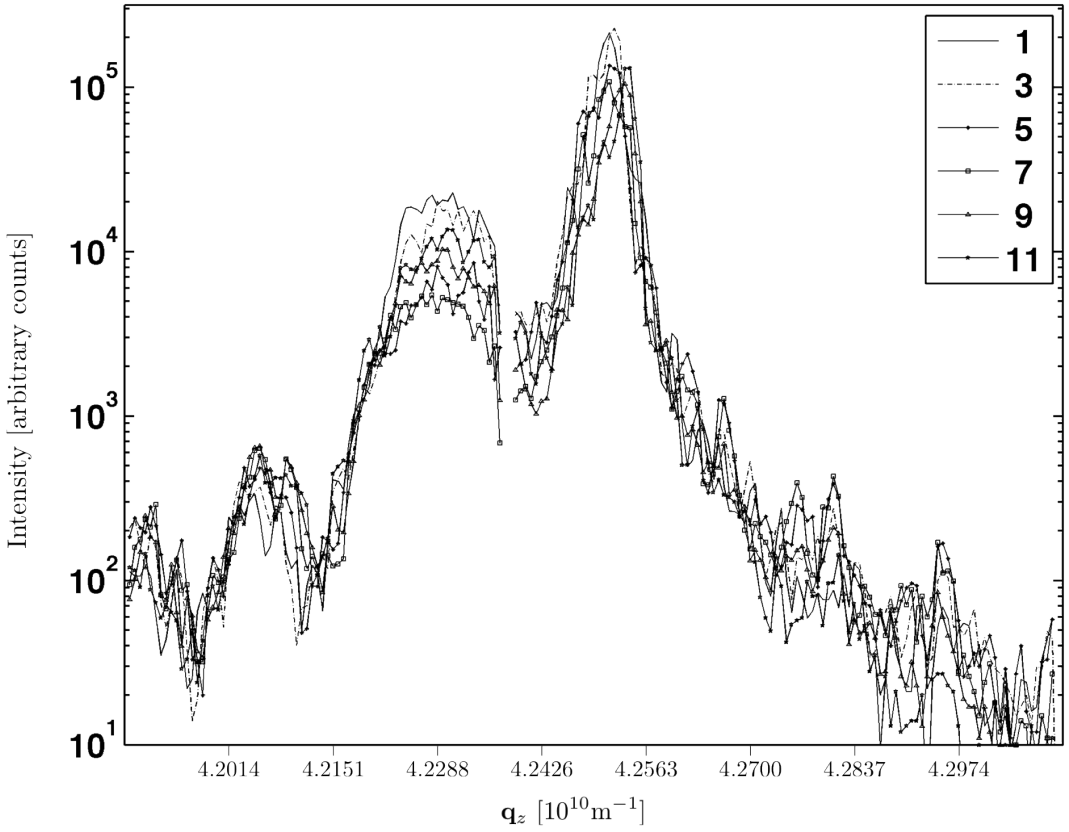

Figure 3.22: $\theta/2\theta$ scans extracted from the ptychographic data at 6 different positions of the scan.

Figure 3.23: Three-dimensional intensities at three different positions of the scan, plotted from different viewing angles. (a)-(b) Position 3 (c)-(d) Position 9 (e)-(f) Position 75.

3.5 Conclusions

In this chapter, we have presented all the experimental details related to this work. Although great care was taken in the sample structure design whose main characteristics were confirmed by complementary detailed post-fabrication structural characterizations, our Bragg ptychography dataset unambiguously shows that structural spatially-dependent fluctuations are present in the sample.

Chapter 4

Data inversion

Contents

One of the first necessary inputs for the experimental data inversion, is to provide an initial estimate of the object to the PRA. Although that in general, random estimates can initialize the algorithm, the development of a spare but accurate model of the sample is of major importance for the evaluation of the experimental reconstruction and the more in-depth understanding of the material behavior. Thus, the *a priori* information that is possessed thanks to the preliminary high-resolution XRD results, as well as the composition and growth knowledge allowed us to build a simple model for the numerical study of the problem.

Nevertheless, the modeling for ptychographic imaging also involves the illumination function which in the majority of the literature is obtained using ptychography with a perfectly known sample and solving the optimization problem with respect to the unknown probe profile [53], or simultaneously updating object and probe during the inversion with a more sophisticated algorithmic process [88, 58]. In Section 4.1, we will briefly describe the technique we employed in order to obtain the probe profile and how from that we constructed the three-dimensional probe.

The sample and probe modeling permitted the study of multiple parameters related with the ptychographic experiment and the inversion strategy, like the overlapping and oversampling conditions, the exposure time per frame (which defines the SNR), or the choice of the inversion algorithm. More specifically, in Section 4.2 we will investigate the role that the initial guess, the choice of the support thickness and the regularization parameter μ play in the data inversion and final reconstruction quality by comparing inversions of synthetic, noise-free and noise-corrupted data. Finally, we will see how we optimized the relevant parameters and discuss the reasons why we chose an *OS-NCG* hybrid inversion strategy for the experimental reconstruction.

4.1 The forward numerical modeling

In this section we will develop the physical model that describes the crystal structure of an ideal InP/InGaAs semiconducting thin film, and employ this model in order to simulate the measured intensity patterns according to the already described theory of the forward modeling [See Chapter 2].

4.1.1 Strain and lattice tilt modeling in a numerical sample

As we saw in Section 3.2, our thin film consists of two layers of InP, and between them, a layer of InGaAs which is lattice-matched with respect to InP. Suppose that the InP and InGaAs layers have exactly the same lattice parameters on the planes which are parallel to the (001) crystallographic planes ($a_{\parallel} = a_c$) after deposition (perfect lattice match). As a result, the unit-cell will elongate in the perpendicular to the (001) planes direction as seen on Fig. 4.1b, thus $a_{\perp} = a'_L$.

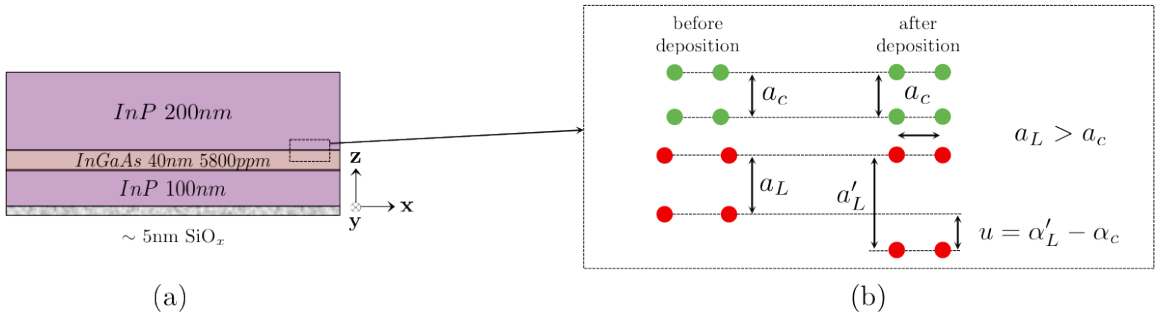

Figure 4.1: (a) A cross-section of the InP/InGaAs thin film. Zero is located in the bottom interface of the sample (InP/SiO$_x$ interface). (b) The atomic arrangement before and after the deposition process (MOVPE). For ideal lattice-matching, the $a_{\perp}$ will adjust to the value of a_c which corresponds to the InP lattice parameter.

The strain component along the (001) direction will be now given by the following equation:

$$\epsilon_{\perp} \equiv \epsilon_{zz} = \frac{a'_L - a_c}{a_c} = \frac{a_{InGaAs} - a_{InP}}{a_{InP}} = \frac{\delta a}{a} \tag{4.1.1}$$

If we consider the displacement along the (001) direction $u_{zz} = \delta a = \delta d$, constant inside the InGaAs layer, then the total phase shift between the two InP/InGaAs interfaces will be an integer multiple of the strained unit-cell which fits in the 40nm-thick InGaAs layer, times the absolute value of the chosen diffraction vector $\mathbf{G}_{004}$.

$$\left.\begin{array}{rcl} (1.1.2) & \Rightarrow & \frac{1}{d^2_{hkl}} = \frac{h^2+k^2+l^2}{a^2} \\ (1.1.8) & \Rightarrow & \Phi = \mathbf{u} \cdot \mathbf{G}_{hk\ell} \end{array}\right\} \Rightarrow \Phi(z) = u_{zz}(z) \cdot \mathbf{G}_{004} = n(z) \cdot \delta d \cdot |\mathbf{G}_{004}|$$

$$\Rightarrow \Phi(z) = \frac{\delta d}{d_{004}} \cdot |\mathbf{G}_{004}| \cdot z = \epsilon_{zz} \cdot |\mathbf{G}_{004}| \cdot z, \ \forall z \in [100, 140] \ [nm] \tag{4.1.2}$$

As we can see from Eqn. (4.1.2), the phase will have a linear dependence on the z coordinate inside the InGaAs layer, while in the two InP layers is expected to be constant, since the InP lattice parameter is ideally considered to be constant. Thus, we can write the phase function

inside the entire sample as a function, independent of the x and y coordinates:

$$\Phi(z) = \begin{cases} 0, & \forall z \in [0, 100)\ [nm] \\ \epsilon_{zz} \cdot |\mathbf{G}_{004}| \cdot z, & \forall z \in [100, 140]\ [nm] \\ 0, & \forall z \in (140, 340]\ [nm] \end{cases} \tag{4.1.3}$$

That is the quantity we are aiming to retrieve, which is contained in the electron density as we explained in Section 1 [See Eq. (1.1.9)]. We can see the phase profile in a cross-section along the thickness of the object on Fig. 4.2 below.

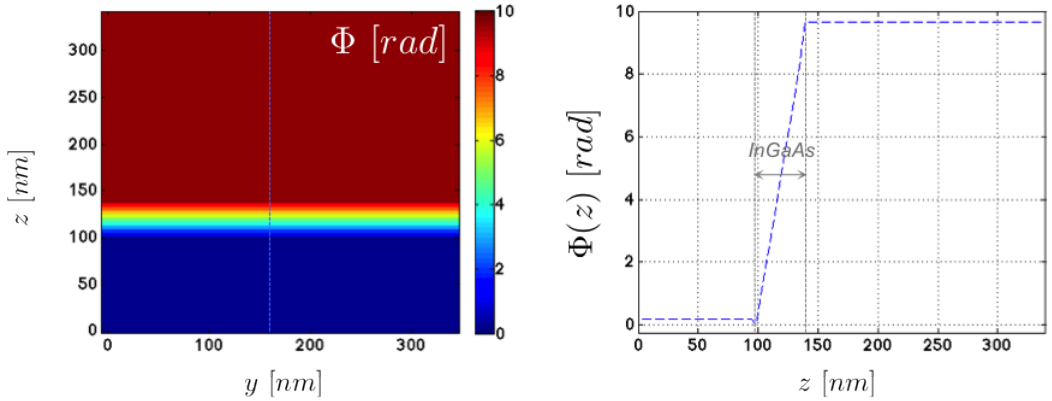

Figure 4.2: (a) Cross-section of the phase profile for an ideal InP/InGaAs thin film. The phase is constant inside the two InP layers depicted with *blue* and *dark red*, while it has a chromatic gradient inside the strained intermediate layer. (b) Plot of the phase along z, taken at the blue dashed line of the left figure.

From the physical point of view, it is worth understanding the influence of the derived model on the diffraction pattern. For this, we will calculate the Fourier transform of the exit-field as we have defined it in Section 2.1, for an illumination function $p_j(\mathbf{r})$ and the derived object function $\rho(\mathbf{r}) = |\rho(\mathbf{r})|\ e^{i\Phi}$ for each of the two materials.
For the two InP layers, since the phase is zero we will have:

$$\Psi(\mathbf{q}) = \int_{-\infty}^{+\infty} \psi_j(\mathbf{r})\ e^{-2\pi i \mathbf{r}\mathbf{q}} \mathbf{dr} = \int_{-\infty}^{+\infty} p_j(\mathbf{r}) |\rho(\mathbf{r})| e^{-2\pi i \mathbf{r}\mathbf{q}} \mathbf{dr} \tag{4.1.4}$$

While for the strained InGaAs layer we get:

$$\begin{aligned} \Psi'(\mathbf{q}) &= \int_{-\infty}^{+\infty} \psi'_j(\mathbf{r})\ e^{-2\pi i \mathbf{r}\mathbf{q}} \mathbf{dr} \\ &= \int_{-\infty}^{+\infty} p_j(\mathbf{r}) |\rho(\mathbf{r})|\ e^{i\Phi}\ e^{-2\pi i \mathbf{r}\mathbf{q}} \mathbf{dr} \\ &= \int_{-\infty}^{+\infty} \psi_j(\mathbf{r})\ e^{i\boldsymbol{\Delta}\mathbf{r}\mathbf{G}_{004} - 2\pi i \mathbf{r}\mathbf{q}} \mathbf{dr} \\ &= \int_{-\infty}^{+\infty} \psi_j(\mathbf{r})\ e^{-2\pi i (\mathbf{r}\mathbf{q} - |\boldsymbol{\Delta}\mathbf{r}| \hat{\mathbf{r}}\ \frac{\mathbf{G}_{004}}{2\pi})} \mathbf{dr} \\ &= \int_{-\infty}^{+\infty} \psi_j(\mathbf{r})\ e^{-2\pi i \mathbf{r}(\mathbf{q} - \frac{|\boldsymbol{\Delta}\mathbf{r}|}{|\mathbf{r}|}\ \frac{\mathbf{G}_{004}}{2\pi})} \mathbf{dr} \\ &= \Psi(\mathbf{q} - \frac{\epsilon_{zz}}{2\pi} \mathbf{G}_{004}) \end{aligned} \tag{4.1.5}$$

We can see that the presence of a linear phase profile inside the InGaAs layer, will displace its far-field diffraction peak with respect to the InP peak and the displacement amount depends only on the strain value ϵ_{zz} and the energy of the X-ray beam. This equation directly relates every gradient in the phase of the object function to the diffraction pattern .

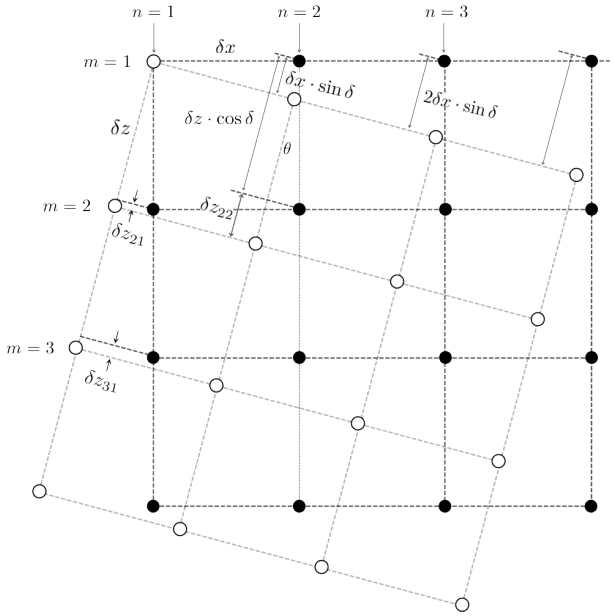

Figure 4.3: Atomic arrangement inside the *ideal* (black dots) and *tilted* (white dots) lattices.

Here, we will focus on investigating the phase behavior when the crystal lattice is tilted with respect to the y axis (tilt axis), which is normal to the rotation plane xz. For this we will use the method of mathematical induction for deriving the phase profile of a tilted lattice. Suppose δ is the tilt angle with respect to the ideal lattice, the displacement amount which will be "seen" by the diffraction vector can be calculated as follows. We start with calculating the accumulative displacement along z as we move in the direction of the x-axis.

$$\delta z_{11} = 0$$

$$\delta z_{12} = \delta x \sin\delta$$

$$\delta z_{13} = 2\delta x \sin\delta$$

$$\vdots$$

$$\delta z_{1n} = (n-1)\delta x \sin\delta$$

And now we continue with calculating the total displacement along z as we move along z, and finally for an arbitrary atom located at position m, n of the lattice.

$$\delta z_{21} = \delta z - \delta z \cos\delta = \delta z(1-\cos\delta)$$

$$\delta z_{31} = 2\delta z - 2\delta z \cos\delta = 2\delta z(1-\cos\delta)$$

$$\vdots$$

$$\delta z_{m1} = (m-1)\delta z(1-\cos\delta)$$

$$\delta z_{22} = \delta z + \delta x \sin\delta - \delta z \cos\delta = \delta x \sin\delta + \delta z(1-\cos\delta)$$

$$\Rightarrow \ \delta z_{mn} = (m-1)\delta x \sin\delta + (n-1)\delta z(1-\cos\delta) \tag{4.1.6}$$

Thus, the additional phase that will correspond to the tilted lattice will be:

$$\Phi(x,y,z,\delta) = \mathbf{u}\cdot\mathbf{G}_{004} = \delta z_{mn}\cdot|\mathbf{G}_{004}| = [(m-1)\delta x\sin\delta + (n-1)\delta z(1-\cos\delta)]\cdot|\mathbf{G}_{004}|$$

$$\Rightarrow\ \Phi(x,y,z,\delta) = [x\sin\delta + z(1-\cos\delta)]\cdot|\mathbf{G}_{004}| \tag{4.1.7}$$

with $\Phi = \Phi(x,y,z,\delta)$ in continuous form. For *small* values of δ we can make the following approximations of $\sin\delta \approx \delta$ and $(1-\cos\delta) \approx 0$. Thus, we obtain

$$\Rightarrow\ \Phi(x,y,z,\delta) = x\delta|\mathbf{G}_{004}| \tag{4.1.8}$$

Which means that any phase gradient in a given direction of DS, will displace the diffraction pattern *mainly* along its corresponding reciprocal direction ($x \rightarrow q_x$), but also in the direction of the diffraction vector $\mathbf{G}_{004}$.

Now, in order to extract the tilt angle δ from the reconstructed phase, one has to calculate the first derivative of the phase with respect to x.

$$\frac{\partial\Phi}{\partial x} = \sin\delta\cdot\mathbf{G}_{004} \Rightarrow \delta = \sin^{-1}\left(\frac{\frac{\partial\Phi}{\partial x}}{\mathbf{G}_{004}}\right) \tag{4.1.9}$$

That is an interesting outcome, because it shows that the distortion of the Bragg peak is encoded, and very small lattice tilts are going to be visible in the retrieved phase as gradients.

4.1.2 Construction of the 3D illumination

The 3D modeling of the intensity which we described in Section 2.2.4, necessitates the construction of a 3D object and a 3D illumination function ($\rho, p_j : \mathbb{R}^3 \rightarrow \mathbb{C}$). The construction of the 3D illumination function is done in two steps. First, we reconstruct the complex X-ray field at the point of focus using an adapted algorithm [51], and then we propagate and incline this field in order to produce a 3D beam in angle to 2θ with respect to the laboratory frame.

For the first step, the inversion approach necessitates the knowledge of the beam at different planes along the propagation axis x_i. The concept of the technique is to reconstruct the planar wavefield of the beam at the focal point [See Chapter 3.3, Fig. 3.9], using the relevant propagation relations from/to the slits and to/from the detector plane in the far field [51]. The knowledge of the slits opening and the measured intensity of the over-focused beam can then be used as constraints for the inversion algorithm, in order to iteratively retrieve the 2D complex illumination profile [See Refs. [44, 64] for more details].

Having this information, the 3D illumination along the propagation direction can be easily constructed under the assumption that the beam is constant inside the sample. A consideration which is valid in the case of X-rays, since the focal depth is a few hundreds of micrometers, while the beam path inside the sample only a few hundreds of nanometers, and absorption is negligible.

We schematically show the assembling of separate frames of the propagating beam in the vicinity of the focal point, for the development of a 3D illumination volume. While in Fig. 3.9b we can see the complex-valued representation of the beam on the normal plane to its propagation ($\mathbf{k}_i$), on Figs. 4.4a-4.4c we can see the amplitude of the beam on the yz plane, being translated in the direction of z in order to reproduce the beam positioning at 2θ in the laboratory frame (x,y,z). The translation is done by Fourier transforming the wavefront and then multiplying with an appropriate linear phase - using the shifts property of the Fourier transform.

On Figs. 4.4d-4.4f we can see different sections of the 3D exit-field inside the numerical sample. We remind the reader that the exit-field is nothing else but the product of the illumination times the object. The height difference of the three cross-sections is due to the Bragg geometry. More

specifically, in order to simulate the Bragg condition for the (004) reflections of the InP/InGaAs thin film, the sample has to be oriented in $\theta \approx 16^{\circ}$ in the laboratory frame, while the probe in 2θ. Finally, on Figs. 4.5a-4.5c we can see the illumination function on the xz plane of incidence, at different positions along y, and on Figs. 4.5d-4.5f the cross-section of the thin film with the illumination.

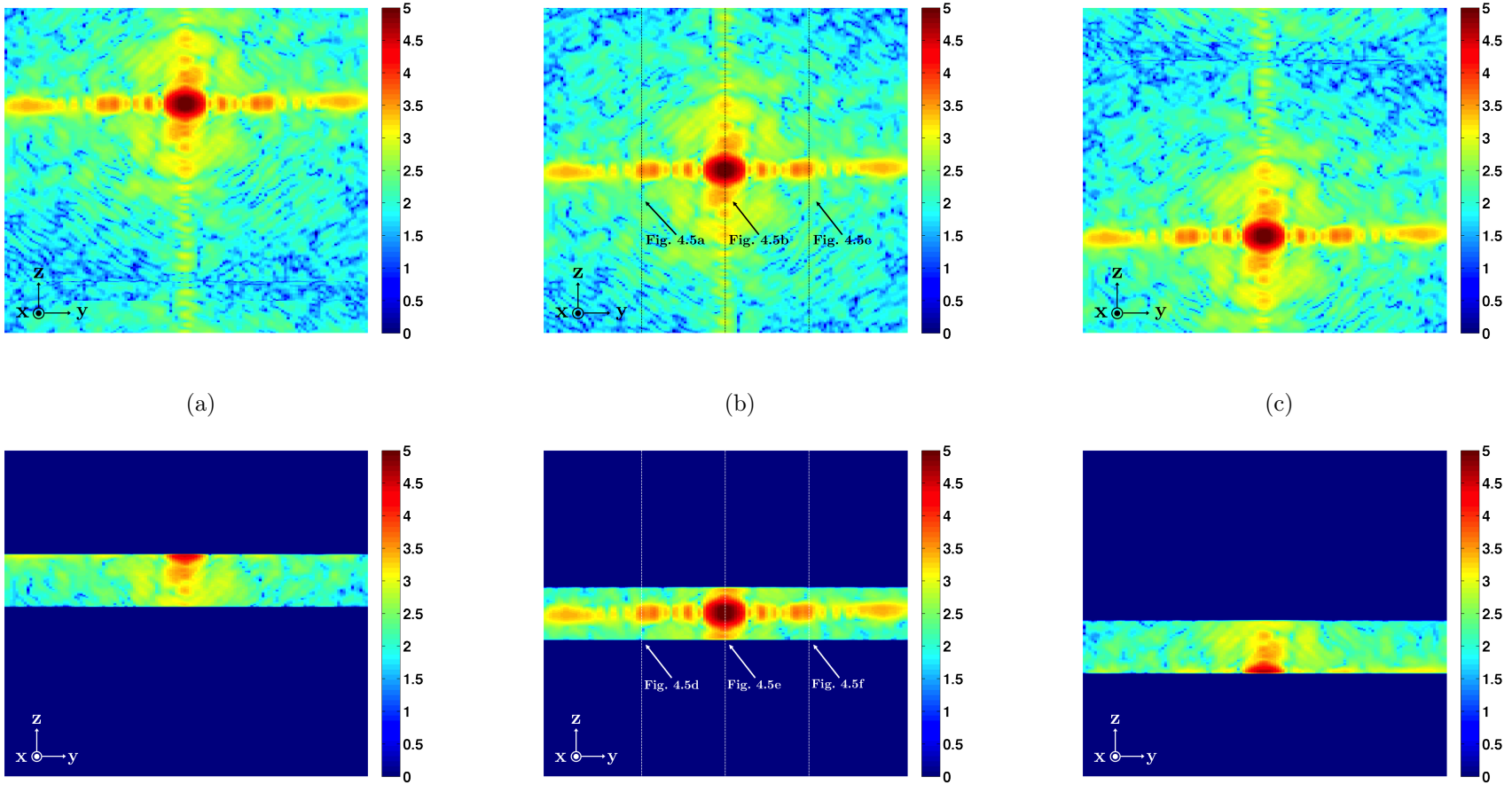

(a) (b) (c)

(d) (e) (f)

Figure 4.4: Cross-sections of (a)-(c) the 3D illumination and (d)-(f) exit-field amplitude at different yz planes in the laboratory reference system. (logarithmic scale, the arrows are scaled to ∼150 nm along y and 170 nm along z)

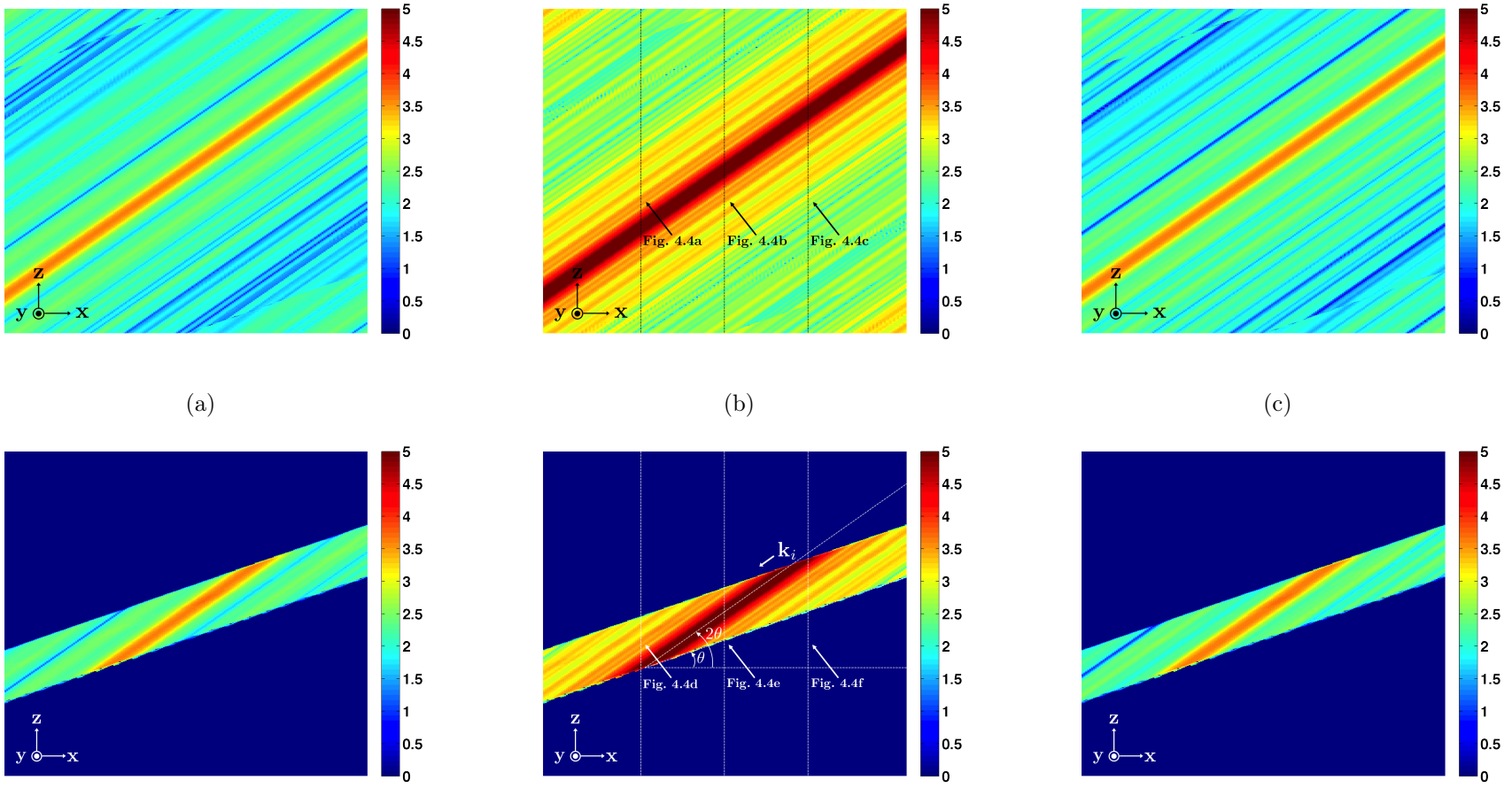

(a) (b) (c)

(d) (e) (f)

Figure 4.5: Cross-sections of (a)-(c) the 3D illumination and (d)-(f) exit-field amplitude at different xz planes in the laboratory reference system. (logarithmic scale, the arrows are scaled to ∼200 nm along x and 170 nm along z)

4.1.3 From a numerical sample to a noisy mock dataset

From Eqn. (2.2.11) and (2.2.19), the expected (*i.e.,* average) intensity detected during a Bragg ptychographic experiment is defined by the following relation[1,2]

$$\mathbf{h}_j(\boldsymbol{\rho}) = |\boldsymbol{\Psi}_j(\boldsymbol{\rho})|^2 + \mathbf{b}_j \tag{4.1.10}$$

where $\mathbf{b}_j \in \mathbb{C}^{M_1 \times M_2 \times M_3}$ is the expected background event component and $\boldsymbol{\Psi}_j \in \mathbb{C}^{M_1 \times M_2 \times M_3}$ is the 3D Fourier transform of the exit-field [See Subsection 2.2.4]

$$\boldsymbol{\Psi}_j(\boldsymbol{\rho}) = \mathrm{DFT}_{3\mathrm{D}}\left(\boldsymbol{p}_j \dot{\times} \boldsymbol{\rho}\right) \tag{4.1.11}$$

with $\boldsymbol{\rho}$ and $\boldsymbol{p}_j$, respectively the sample and the j-th probe function expressed in the DS natural system. Because the sample $\boldsymbol{\rho}$ is the quantity of interest, the formal dependency with respect to $\boldsymbol{\rho}$ is made explicit in the modeling relations (4.1.10) and (4.1.11).

In this chapter, our aim is to investigate, through numerical means, if the sample can be retrieved from the inversion of a noisy ptychographical dataset. From that perspective, the expected intensity (4.1.10) is a pivotal quantity. Firstly, this relation is used for *simulation* purposes when one aims at generating a numerical (mock) Bragg ptychography diffraction dataset, when both probe and sample are given. More precisely, according to Subsection 2.2.4, for each probe position $j = 1 \cdots J$, the recorded intensities are gathered in a matrix $\boldsymbol{Y}_j$ with size $M_1 \times M_2 \times M_3$, where $M_1 \times M_2$ is the number of pixels on the camera and M_3 is the number of points extracted in the rocking-curve. For a more realistic simulation, photon shot-noise is considered: each element in $\boldsymbol{Y}_j$ is a pseudo-random integer drawn from a Poisson law via the following probability distribution function[3]

$$P(\boldsymbol{Y}_{j;\boldsymbol{m}}) = e^{-\mathbf{h}_{j;\boldsymbol{m}}(\boldsymbol{\rho})} \times \frac{\mathbf{h}_{j;\boldsymbol{m}}(\boldsymbol{\rho})^{\boldsymbol{Y}_{j;\boldsymbol{m}}}}{\boldsymbol{Y}_{j;\boldsymbol{m}}!} \tag{4.1.12}$$

where $\boldsymbol{m} = (m_1, m_2, m_3)$ stands for a triplet locating a scalar in the 3D matrices $\boldsymbol{Y}_j$ or $\boldsymbol{h}_j(\boldsymbol{\rho})$. This results in a synthetic dataset $\{\boldsymbol{Y}_j\}_{j=1}^{J}$ mimicking the diffracted intensity expected during the Bragg diffraction experiment presented in Section 3.3. Let us stress that such a mock data-set can be generated with an arbitrary signal-to-noise ratio. For that purpose, the expected intensity (4.1.10) considered in (4.1.12) is slightly modified and reads

$$\mathbf{h}_j(\boldsymbol{\rho}\,;\, I_0) = I_0 \times |\boldsymbol{\Psi}_j(\boldsymbol{\rho})|^2 + \mathbf{b}_j \tag{4.1.13}$$

where the parameter $I_0 \in \mathbb{R}^+$ scales the averaged intensity of the probe function, hence allowing to adjust the global photon counting rate that would be detected by the camera.

On Figure 4.6 we show the expected (noise-free) diffraction pattern generated from the numerical sample, presented in the beginning of the chapter for two angles of incidence: one that satisfies the Bragg condition for the InP (004) crystallographic planes, and the other one for the InGaAs. On the same figure [Figs. 4.6d,g] we can also see the noise-corrupted diffraction patterns for two different values of SNR. The reason for $I_0 = 10^4$ was dictated by the actual counting rate of the ptychography experiment, as depicted in Fig. 3.16, where the maximum intensity is 13000 photons. This value of I_0 produces counting rates similar to the ones observed in the real experiment.

[1] In the relation (4.1.10) and (4.1.11) above, $|\cdot|^2$ and $\dot{\times}$ stand for component-wise squared modulus and multiplication operations.

[2] Let us stress that, according to Sec. 2.2.4, the relation (4.1.10) should read $\mathbf{h}'_j = |\boldsymbol{\Psi}'_j|^2 + \boldsymbol{b}'_j$ where the "$'$" mark denotes the sampling of the reciprocal-space along the *natural coordinate system*. However, for notational convenience, the the "$'$" mark will be dropped in the sequel, and the notations $\mathbf{h}'_j$, $\boldsymbol{\Psi}'_j$, $\boldsymbol{p}'_j$ and $\boldsymbol{\rho}'$ are replaced hereafter by $\mathbf{h}_j$, $\boldsymbol{\Psi}_j$, $\boldsymbol{p}_j$ and $\boldsymbol{\rho}$, respectively.

[3] The random outcome is generated with the **poissrnd** function from the Matlab Statistics Toolbox.

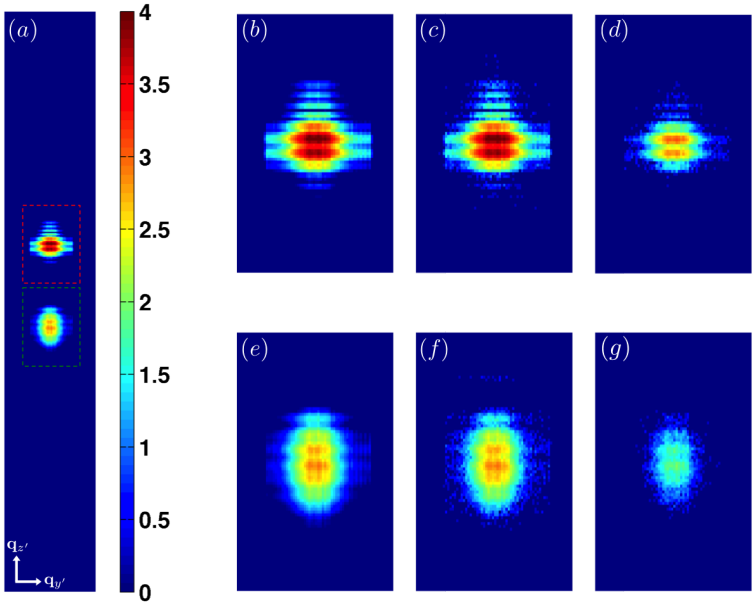

Figure 4.6: (a) The noise-free InP and InGaAs (004) Bragg peaks superimposed (13000 photons at max). (b) Zoom on the red rectangle area of the InP peak (noise-free). Same frame as before for (c) noise-corrupted data with 13000 photons at max and (d) 1300 photons at max. (e) Zoom on the green rectangle area of the InGaAs peak (noise-free). Same frame as before for (f) noise-corrupted data with 13000 photons at max and (g) 1300 photons at max.

Finally, as explained in Sec. 2, relation (4.1.10) is also a pivotal quantity involved in the *phase retrieval* algorithm, *i.e.,* when one aims at retrieving the sample with both the knowledge of the probe and the ptychographical dataset. Since mock datasets can be generated with arbitrary SNRs, we now aim at investigating the ability of the inversion algorithms presented in Subsection 2.1.2 to retrieve the numerical sample defined above from a set of diffracted intensities.

4.2 Inversion strategy

The algorithms presented in Section 2 make rather straightforward to investigate if the numerical sample (or at least a good estimate of it) can be retrieved from a simulated noisy dataset: given an *initial-guess* (or initial estimate) $\boldsymbol{\rho}_{k=0}$, either the OS-PIE (2.1.17) or the nonlinear conjugate-gradient (2.1.20) generates a sequence $\{\boldsymbol{\rho}_k\}_{k=1\cdots\infty}$ aiming at iteratively minimizing the (least-square) criterion that reads

$$\mathcal{L}(\boldsymbol{\rho}) = \sum_j \mathcal{L}_j(\boldsymbol{\rho}) \qquad \text{with} \qquad \mathcal{L}_j(\boldsymbol{\rho}) := \sum_{\mathbf{m}} \left[\boldsymbol{Y}_{j;\mathbf{m}}^{1/2} - \boldsymbol{h}_{j;\mathbf{m}}^{1/2}(\boldsymbol{\rho}) \right]^2 . \tag{4.2.1}$$

As explained in Section 2.1.2, the quantity (4.2.1) is also known as the *data fidelity term* since it is a distance between the *recorded intensities* $\{\boldsymbol{Y}_j\}_{j=1}^J$ and the *expected intensities* $\{\boldsymbol{h}(\boldsymbol{\rho})\}_{j=1}^J$ generated from the proposed sample $\boldsymbol{\rho}$. As a result, this quantity vanishes if one considers in (4.2.1) the noise-free dataset and the true object —*i.e.,* the sample used to generate the intensity patterns. If the initial-guess is *not* the true object (but it is not "too far" from it either) we do expect that the true object will be retrieved, leading to a criterion decreasing toward zero as the iteration number grows. As an illustration, 300 iterations of the OS algorithm were performed

with an initial-guess that is a slightly perturbed[4] version of the true object. The evolution of the criterion is shown in Fig. 4.9, and a cross-section[5] through the initial/retrieved objects is shown in Fig. 4.10a-4.10d and in Figs. 4.11a-4.11d for a zoomed version.

Obviously, noisy data should be considered in a real experiment and, in this case, the criterion does not decrease toward zero with the iteration number. In this case, if one uses an initial-guess that is the true object, the algorithm converges to a "perturbed" version of this object; this retrieved object is however the one that is consistent with the data. These assertions are illustrated in Fig. 4.9, and in Figs. 4.10e-4.10h and Fig. 4.11e-4.11h.

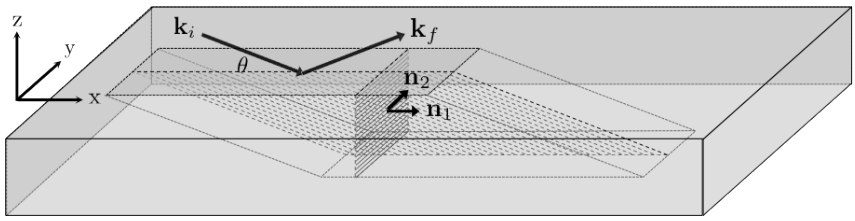

Figure 4.7: 3D representation of the InP/InGaAs thin film. We can see the inclined illuminated volume, the incident and diffracted beam ($\mathbf{k}_i$ and $\mathbf{k}_f$), as well as the yz and xz planes (denoted by their normal $\mathbf{n}_1$ and $\mathbf{n}_2$ vectors respectively).

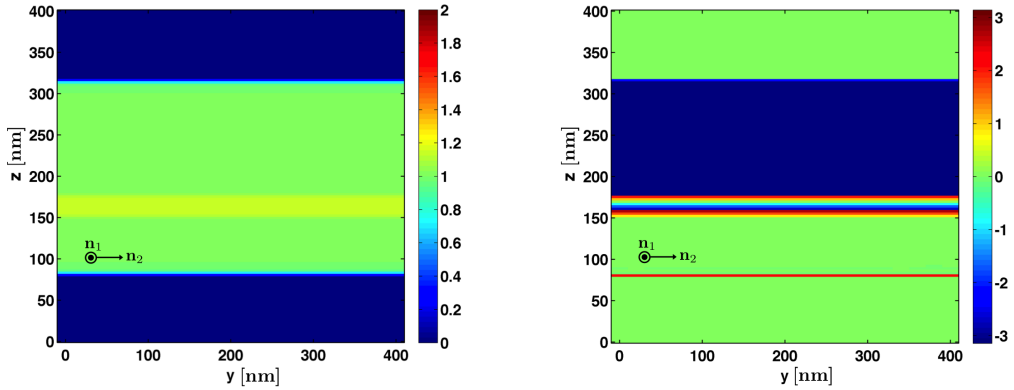

Figure 4.8: Slice of the true object object on the central yz plane of the 3D numerical object. We can see its (a) amplitude and (b) phase.

From the computational side, it should be stressed that we have to deal with a *very large-scale* optimization problem. For instance, the number of unknown parameters that are updated in each iteration is $N_x \times N_y \times N_z = 276 \times 120 \times 622 = 20.600.640$ — *i.e.,* the size of the 3D numerical

[4]The initial estimate is related with the true object by the following equation, which points out the relative amplitude and phase fluctuations with an adequate degree of randomness.

$$\boldsymbol{\rho}_{k=0;\mathbf{n}} = \boldsymbol{\rho}^*_{\mathbf{n}} + X \cdot e^{i\pi Y}, \quad \forall \mathbf{n} \in \mathcal{S} \tag{4.2.2}$$

where $\boldsymbol{\rho}^*$ is the true object, and X, Y are two random variables with uniform distribution in $[0, 1]$.

[5]For the examination of the retrieved objects, we will make use of 2D slices taken from the 3D volume, as seen in Fig. 4.7. Having in mind the inclined by $\theta_B = 16.38°$ incident beam, denoted by the $\mathbf{k}_f$ vector, and the fact that the algorithm is going to reliably reconstruct the amplitude and phase *only* in the well lighten part of the sample, one needs to define a reasonable way to examine and compare the reconstructions. For this reason we take 2D slices at the center of the reconstructed volume on the yz plane, defined by the normal to its surface vector $\mathbf{n_1}$. [See Figs. 4.7, 4.8].

sample. In addition, each one of the $J = 99$ probe positions give birth to $M_3 = 180$ diffraction patterns, each one being composed with $M_1 \times M_2 = 516 \times 100$ pixels. The sample estimate and the dataset are bulky quantities requiring several GBs of RAM for the storage. Hence, the algorithms have to deal with a considerable computational burden: one single iteration of the OS-PIE or the NCG requires typically[6] 3 minutes, leading to around 15 hours of run-time for 300 iterations. With such running times, it turns out that the choice of the *initial guess* is a critical issue. This is the put forward in the next subsection.

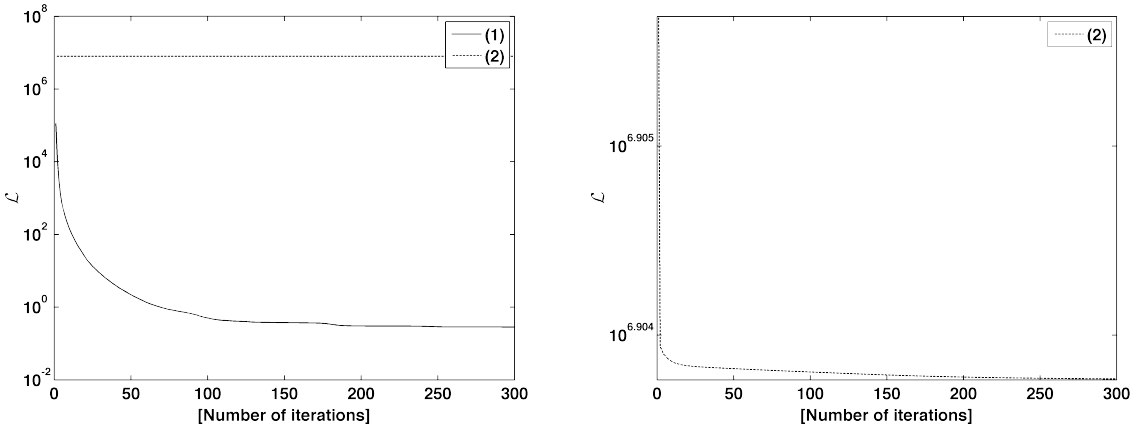

(a) (b)

Figure 4.9: (a) The criterion of Eqn. 4.2.1 as a function of the number of iterations for the two inversions, with their results shown on Fig. 4.10. (b) Zoom at the criterion of the second inversion (2). We can see that in the case of noise-corrupted data the criterion doesn't decrease below 10^6, while for noise-free data it converges to zero.

[6]For the phase retrieval we used a workstation with 2 Quad Core Intel Xeon X5690 CPUs @ 3.47GHz and 94GB of DDR3 RAM @ 1333MHz.

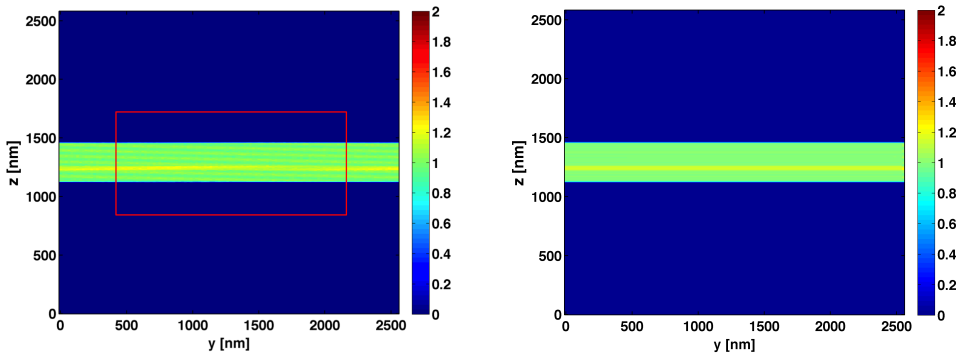

(a) Initial amplitude (1)

(b) Retrieved amplitude (1)

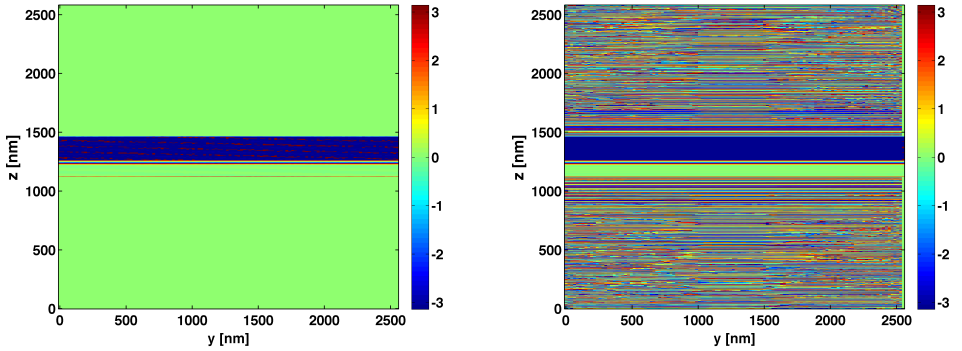

(c) Initial phase (1)

(d) Retrieved phase (1)

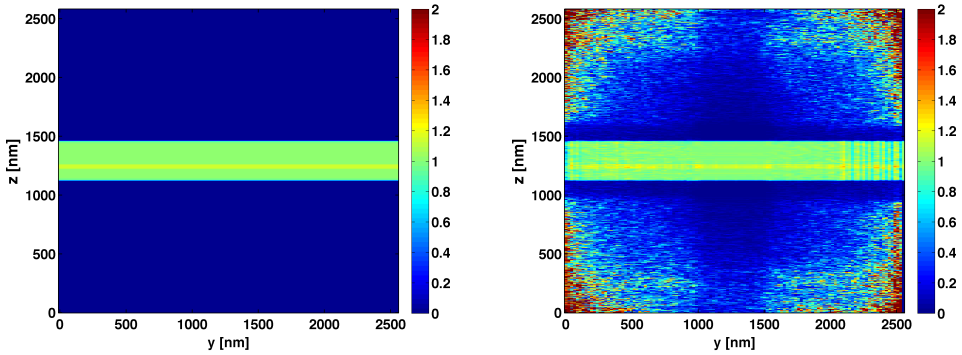

(e) Initial amplitude (2)

(f) Retrieved amplitude (2)

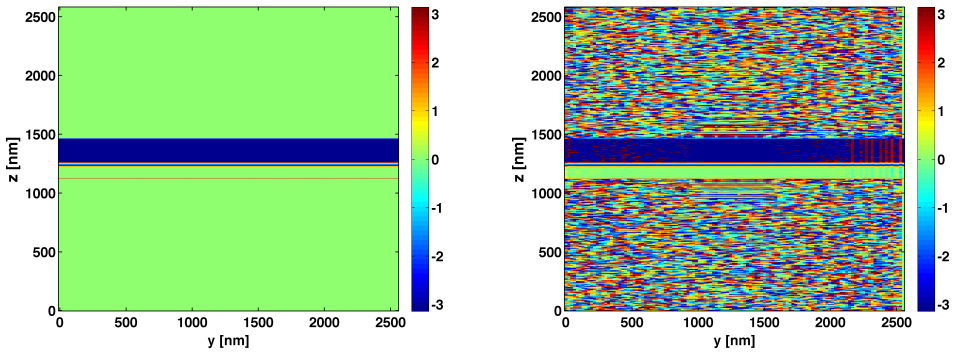

(g) Initial phase (2)

(h) Retrieved phase (2)

Figure 4.10: In the left column, cross-sections of the initial estimate are shown: (a, c) are from an object "close" to the true object (see text for details) while (e, g) correspond to the true object. The retrieved object is shown in the right column: (b, d) were obtained from noise-free data while (f, h) were obtained with noisy data.

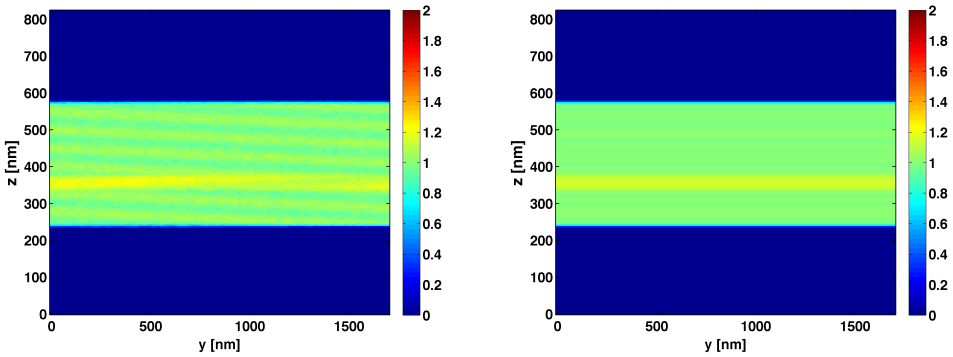

(a) Initial amplitude (1)

(b) Retrieved amplitude (1)

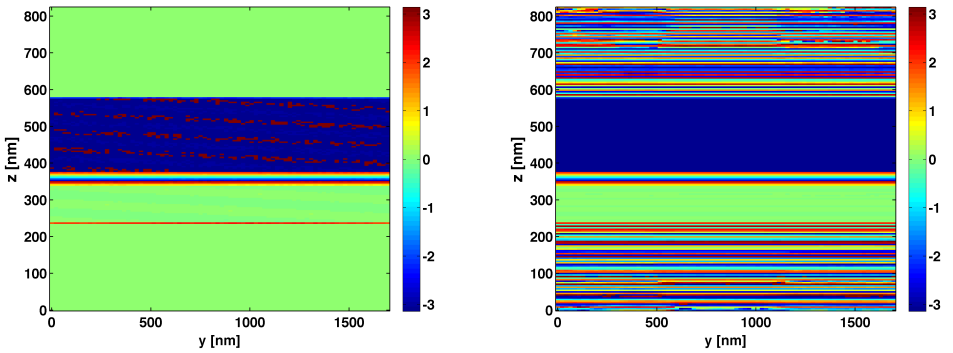

(c) Initial phase (1)

(d) Retrieved phase (1)

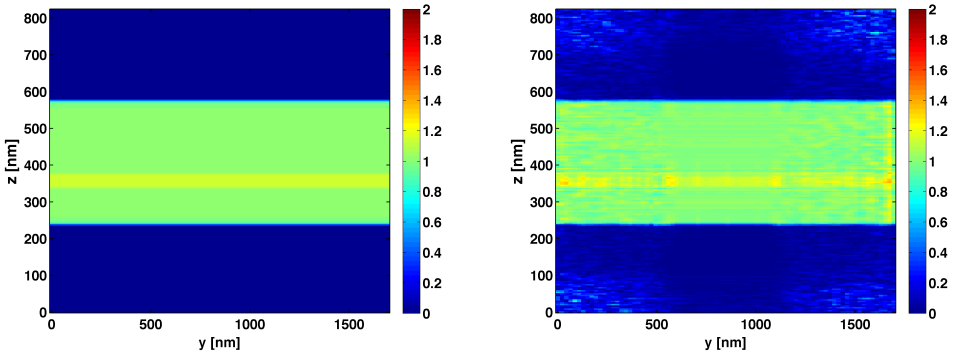

(e) Initial amplitude (2)

(f) Retrieved amplitude (2)

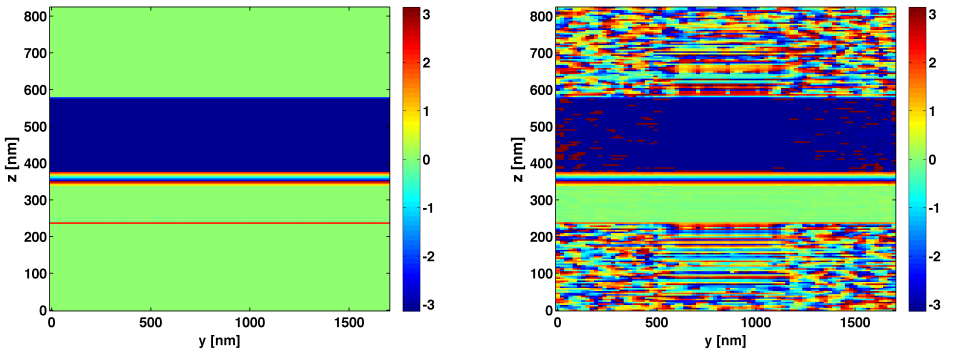

(g) Initial phase (2)

(h) Retrieved phase (2)

Figure 4.11: Zooms of the previous page cross-sections. Again, we can see the retrieved amplitude and phase for two different initial estimates using noise-free (b, d) and noise-corrupted data (f, h). The initial estimate in (a, c) is $\neq$ true object but sufficiently close to the true object, while in (e, g) is the true object.

4.2.1 A reconstruction (very) sensitive to the initial-guess

The sample retrieved from noisy data in Figs. 4.10f and 4.10h can somehow be considered as the "best" reconstruction one can achieve since it was obtained with the true numerical sample as an initial-guess. In practice though, the true object is unknown or never known precisely and it is legitimate to investigate how the reconstruction is sensitive to the initial-guess.

As shown in Figs. 4.14a and 4.14d, a poor initial estimate clearly prevents the algorithm to reach a valuable reconstruction of the sample. Furthermore, we note that the final value reached by the criterion decreases when some relevant features about the sample are introduced in the initial-guess. However, this numerical experiment clearly suggests that this initial guess needs to be really "close" to the minimizer of the least-square criterion if one hopes that it is reached (at least in a realistic amount of time) by the algorithm. For instance, while the initial guess shown in Fig. 4.13c and 4.14c is almost identical to the true object (they share the same modulus and the phases are only slightly different in the InGAS layer: the phase slope in the initial guess is 70 % the slope in the true object), the retrieved object seems rather deteriorated. In other words, the spatial diversity in 3D Bragg ptychography is not sufficient to avoid a stagnation of the iteration and/or the convergence to an irrelevant local minimum.

These pathological behaviors are long known in the standard (2D) CDI community [23, 89] and we wish now to explore these issues with this comparison in mind. For instance, the solution unicity for the 2D phase problem[7] [20] assumes the knowledge of the support of the unknown object [24, 89] and, as shown by several numerical analysis [90], the robustness with respect to this support constraint is rather poor. In the '90s, this issue was circumvented with a scanning probe extracting, in each position, a local information about the phase of the sample: it is exactly the 2D ptychographic experiment that is much more robust to the initial guess. In a 3D Bragg ptychographic experiment, *because the probe is invariant along the propagation direction, this information about the sample is not extracted locally along that direction.* As a result, the reconstruction is poorly constrained along that direction, resulting in "echoes" which prevent the algorithm to converge efficiently, see for instance Fig. 4.10f.

In conclusion, these convergence issues stem from the inherent ambiguities of the 3D phase retrieval problem that we aim at solving by the iterative minimization of Equation (4.2.1). Nevertheless, some additional constraints can solve (at least partially) these issues. This is the topic of the next section.

[7] In addition, this unicity result still hold if the diffraction pattern is *sampled* at twice the Nyquist sampling rate [22].

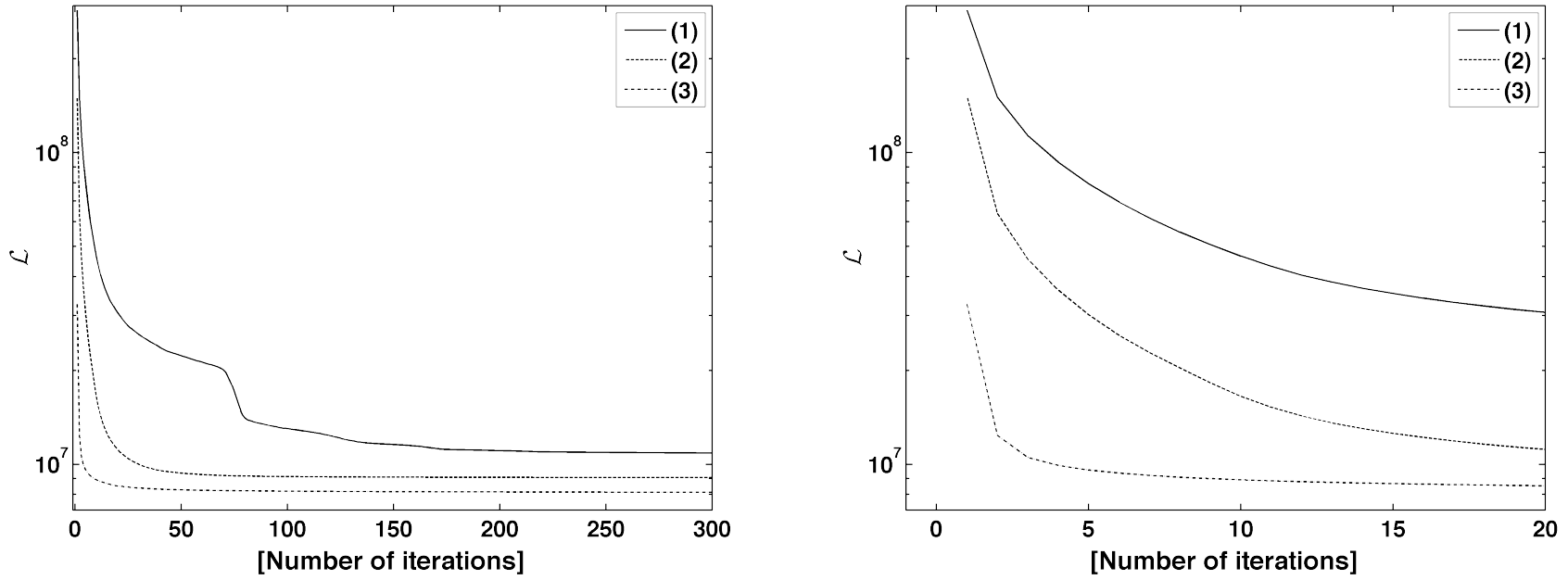

(a) (b)

Figure 4.12: (a) The criterion of Eqn. 4.2.1 as a function of the number of iterations for three inversions, with their results shown in Figs. 4.13-4.14. The bottom curve corresponding to the inversion using the true object as initial estimate, can be considered as a lower limit for the values of the criterion, and represents ultimately the ideal reconstruction one can obtain using noise-corrupted data. (b) Zoom at the criterion of the three inversions during the first twenty iterations. We can see that as we provide an initial estimate which is closer to the true object, the value of the criterion starts from lower values.

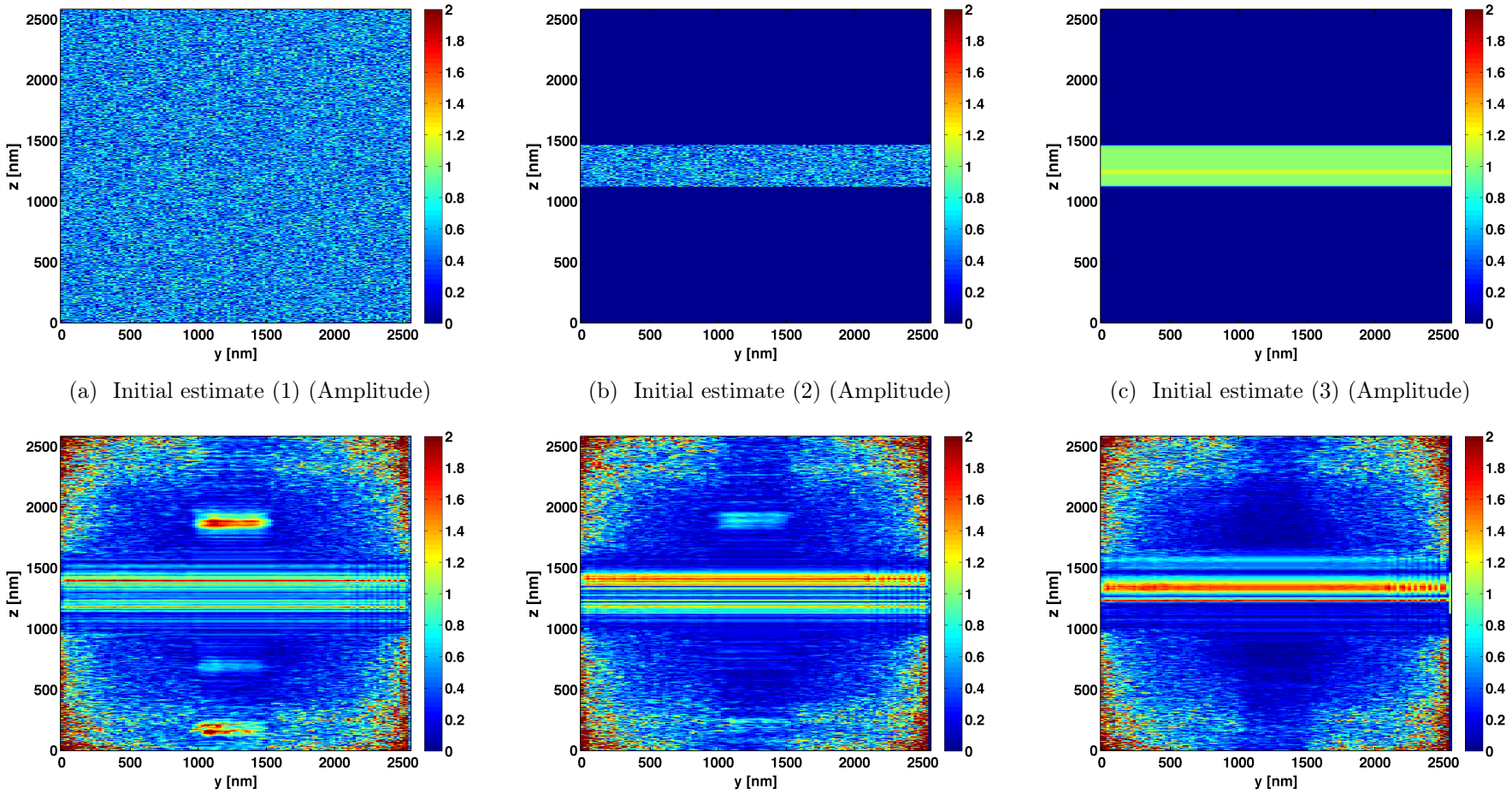

(a) Initial estimate (1) (Amplitude)

(b) Initial estimate (2) (Amplitude)

(c) Initial estimate (3) (Amplitude)

(d) Retrieved object (1) (Amplitude)

(e) Retrieved object (2) (Amplitude)

(f) Retrieved object (3) (Amplitude)

Figure 4.13: Cross-sections of the retrieved amplitude for three different initial estimates using noisy data. The initial estimates amplitude can be seen in (a)-(c), and the retrieved object in (d)-(f). For comparison with the inversion result when providing as initial estimate the true object we refer to Fig. 4.11f.

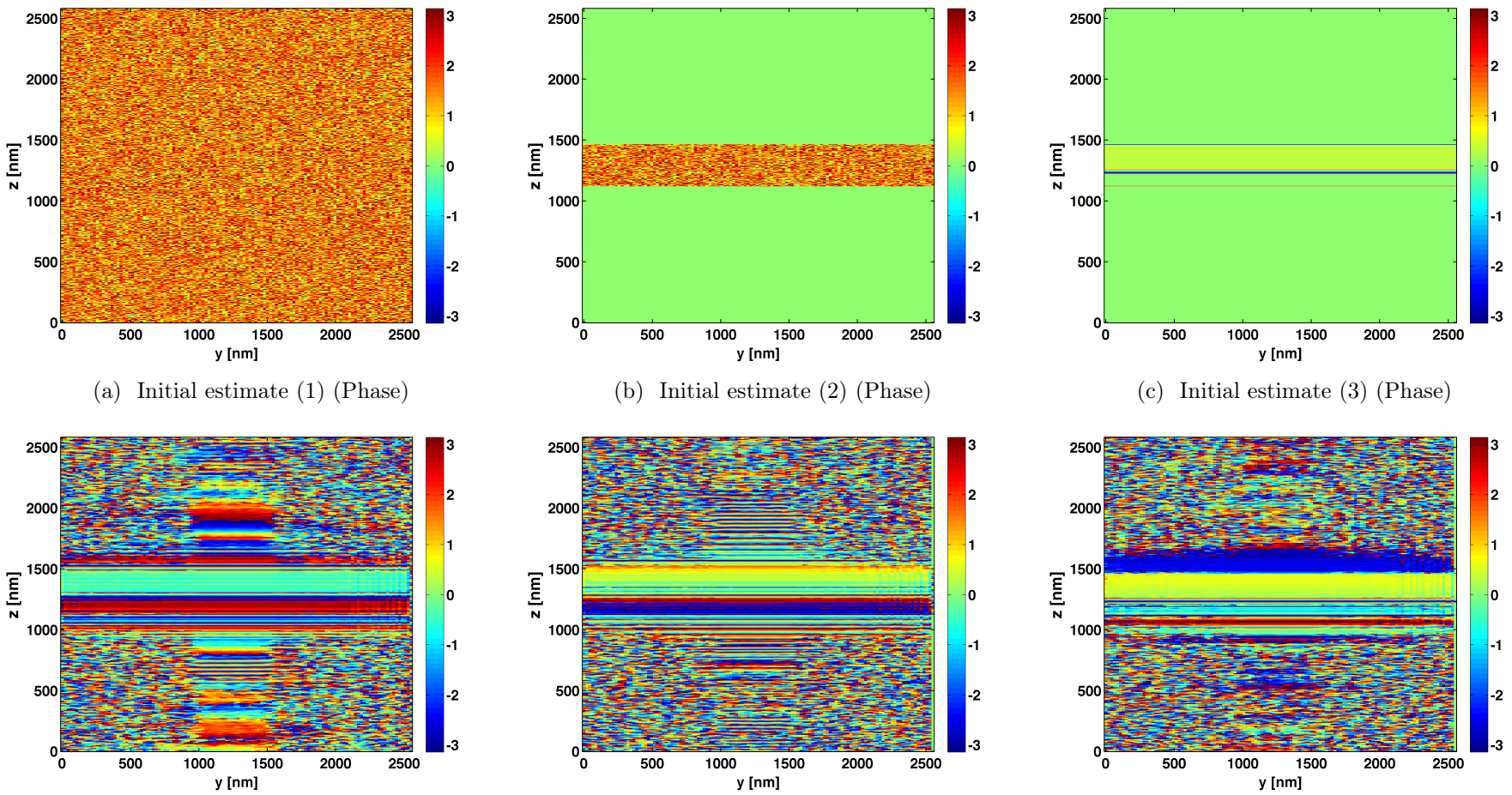

(a) Initial estimate (1) (Phase)

(b) Initial estimate (2) (Phase)

(c) Initial estimate (3) (Phase)

(d) Retrieved object (1) (Phase)

(e) Retrieved object (2) (Phase)

(f) Retrieved object (3) (Phase)

Figure 4.14: Cross-sections of the retrieved phase for three different initial estimates using noisy data. The initial estimates phase can be seen in (a)-(c), and the retrieved object in (d)-(f). For comparison with the inversion result when providing as initial estimate the true object we refer to Fig. 4.11h.

4.2.2 A penalization acting as a "soft" support-constraint

From a methodological (*i.e.,* inverse problem theory) perspective, the robustness problems reported above should be solved *via* the introduction of *a priori* structural constraints about the expected solution. These constraints act as additional information about the true sample. This strategy (also known as regularization) is a quite common process in the field of inverse problems [61, 91, 92].

From a practical viewpoint, this regularization usually takes the form of a *penalty function* $\mathcal{P}$ added to the data-fidelity term (4.2.1). Obviously, this penalty is chosen so that it enforces some expected features in the retrieved sample. In our case, following Berenguer *et al.* [62], this penalty simply enforces the retrieved sample to be a thin film (*i.e.,* it should act as a support constraint). More precisely, let us introduce the sets

$$\Omega := \{\mathbf{n} \,|\, \mathbf{n} \text{ does belong to the support of the thin film}\}$$

and

$$\overline{\Omega} := \{\mathbf{n} \,|\, \mathbf{n} \text{ does } \textit{not} \text{ belong to the support of the thin film}\},$$

then, the *penalized criterion* that the algorithm aims at minimizing now reads

$$\mathcal{J}(\boldsymbol{\rho}\,;\,\mu) = \mathcal{L}(\boldsymbol{\rho}) + \mu\mathcal{P}(\boldsymbol{\rho}) \qquad \text{with} \qquad \mathcal{P}(\boldsymbol{\rho}) := \textstyle\sum_{\mathbf{n}\in\overline{\Omega}} |\boldsymbol{\rho}_{\mathbf{n}}|^2 \tag{4.2.3}$$

where $\boldsymbol{\rho}_{\mathbf{n}} \in \mathbb{C}$ stands for the scalar element with coordinate $\mathbf{n} := (n_x, n_y, n_z)$ in the 3D matrix $\boldsymbol{\rho}$. Because the penalty $\mathcal{P}$ is a summation over the set $\overline{\Omega}$, any non-zero value outside the support of the retrieved sample is penalized (but not prohibited). The *regularization parameter* $\mu \geqslant 0$ tunes how this support constraint should be enforced in the final solution. While the traditional support constraint in CDI is a "hard" constraint (0 or 1), this "soft" support constraint does not set the voxel outside the support to be exactly zero, hence allowing non-zero values to emerge if the dataset is strongly informative. In the sequel, we will assume that the geometry of the thin film consists in a rectangular slab that is *only parametrized by its thickness* denoted by ω. Obviously, with experimental datasets, both the thickness ω and the regularization parameter μ need to be adjusted. Before we detail the tuning of these parameters, we need to explain how the algorithms in Section 2.1 should be modified so that the penalized criterion (4.2.3) can be minimized.

Some implementations details. Let us consider the following equivalent formulation for the criterion of Eqn. (4.2.3)

$$\mathcal{J}(\boldsymbol{\rho}\,;\,\mu) = \sum_{j=1}^{J} \mathcal{J}_j(\boldsymbol{\rho}\,;\,\mu) \qquad \text{with} \qquad \mathcal{J}_j(\boldsymbol{\rho}\,;\,\mu) := \mathcal{L}_j(\boldsymbol{\rho}) + \frac{\mu}{J}\sum_{\mathbf{n}\in\overline{\Omega}} |\boldsymbol{\rho}_{\mathbf{n}}|^2. \tag{4.2.4}$$

According to the presentation of the OS-PIE and the nonlinear conjugate-gradient algorithm [See Subsection 2.1.2], the gradient of $\mathcal{J}_j$ is needed for the construction of these algorithms. It is easy to obtain that this gradient reads

$$\partial\mathcal{J}_{j;\mathbf{n}}(\boldsymbol{\rho}) = \begin{cases} \partial\mathcal{L}_{j;\mathbf{n}}(\boldsymbol{\rho}) + \dfrac{2\mu}{J}\boldsymbol{\rho}_{\mathbf{n}} & \forall \mathbf{n} \in \overline{\Omega} \cap \mathcal{S}_j \\ \partial\mathcal{L}_{j;\mathbf{n}}(\boldsymbol{\rho}) & \forall \mathbf{n} \in \Omega \cap \mathcal{S}_j \\ 0 \quad \text{otherwise} \end{cases} \tag{4.2.5}$$

where $\partial\mathcal{L}_{j;\mathbf{n}}$ was defined in (2.2.31).

Finally, the preconditioning matrix that was previously defined in (2.1.18) should also be modified according to

$$\mathbf{\Lambda} = \alpha + \sum_j \left(\boldsymbol{p}_j^* \dot{\times} \ \boldsymbol{p}_j \right) + \mu \, \boldsymbol{I}_{\overline{\omega}} \qquad \alpha > 0 \tag{4.2.6}$$

where $\boldsymbol{I}_{\overline{\omega}}$ is a 3D matrix of the size of the sample with only zeros and ones, the entry is one if $\mathbf{n} \in \overline{\Omega}$ and zero if $\mathbf{n} \in \Omega$.

The tuning of the regularization parameter μ. Although the addition of an extra parameter μ is not a wishful thinking for optimization processes, it permits a more elaborate use of the inversion strategy while generalizing the support constraint. Now we can consider for $\mu \to 0$ the absence of any support, while for $\mu \to \infty$ the use of a traditionally abrupt support constraint. As an illustrative example, Figs. 4.16 shows the impact of this regularization parameter for a noisy dataset and the true object as an initial guesses. Clearly, a rational mean to find an "optimal" value of the regularization parameter is needed. In an attempt to define what "optimal" means, let us first note that the minimizer of the criterion (4.2.3) is a trade-off between two sources of information: the one coming from the data-fidelity part and the one coming from the *a priori* (penalty) part. The *L-curve strategy* [93, 94] aims at finding a value for μ resulting in a *balanced trade-off* between both these sources of information. In practice, this strategy consists in minimizing the criterion (4.2.3) for various values $\mu \in \{\mu_1, \mu_2, \cdots, \mu_L\}$, hence providing a set of 3D retrieved samples $\{\widehat{\boldsymbol{\rho}}_l\}_{l=1\cdots L}$.

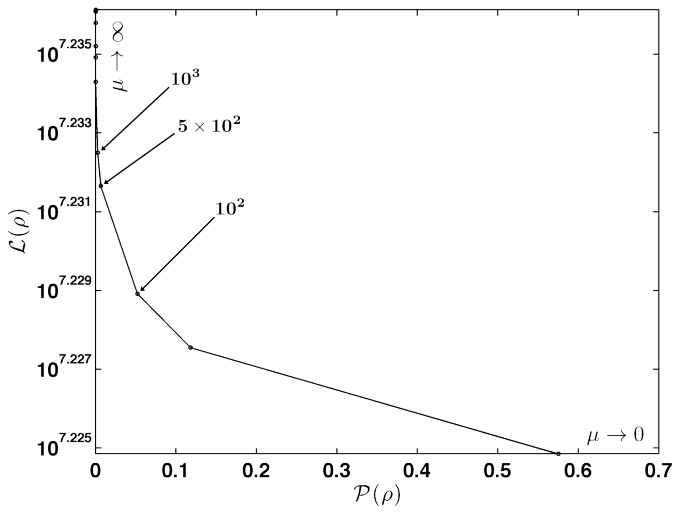

Figure 4.15: The *L-curve* for the optimization of the regularization parameter μ.

The plotting of the data-fidelity term $\{\mathcal{L}(\widehat{\boldsymbol{\rho}}_l)\}_{l=1\cdots}$ *versus* the "penalization term" $\{\mathcal{P}(\widehat{\boldsymbol{\rho}}_l)\}_{l=1\cdots}$ usually shows a "L shape". The lower (horizontal) part of the "L" shape defines the solution set that are mostly driven by the *prior* information. Conversely, the upper (vertical) part of the "L" shape defines the solution set that are mostly driven by the data-fidelity information. Between these two regimes lies the corner of the "L" that defines the solution that is usually selected, *i.e.*, a solution driven by a balanced contribution of both the sources of information, see Fig. 4.15 for an illustration.

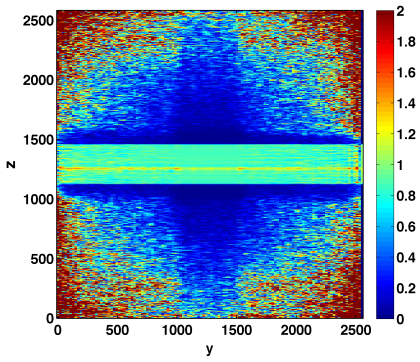

(a) Retrieved amplitude ($\mu = 0$)

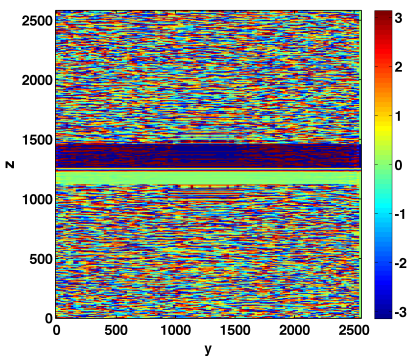

(b) Retrieved phase ($\mu = 0$)

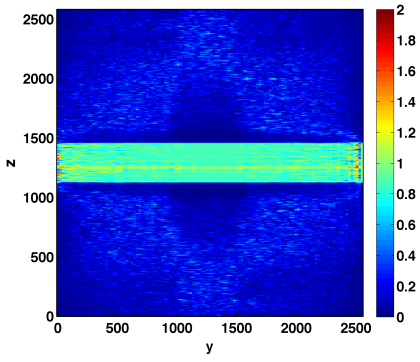

(c) Retrieved amplitude ($\mu = 10^2$)

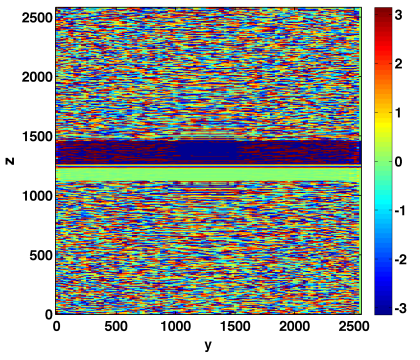

(d) Retrieved phase ($\mu = 10^2$)

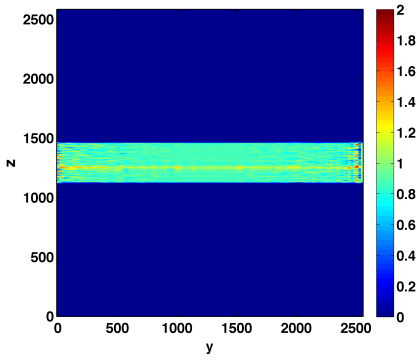

(e) Retrieved amplitude ($\mu = 10^7$)

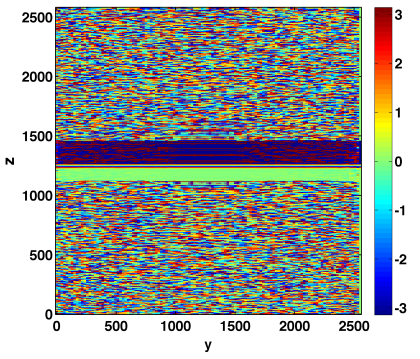

(f) Retrieved phase ($\mu = 10^7$)

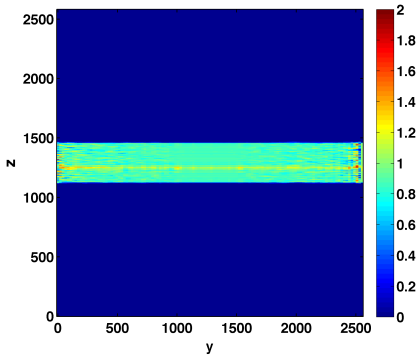

(g) Retrieved amplitude ($\mu = 10^{90}$)

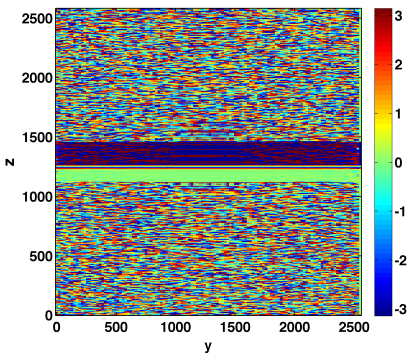

(h) Retrieved phase ($\mu = 10^{90}$)

Figure 4.16: Cross-sections of the retrieved amplitude and phase when providing as initial estimate the true object and noisy data. We can see that for low values of μ, a large number of pixels outside of the support shows nonzero values.

It should be noted, however, that this prior information is mostly enforced *outside* of the support of the sample. This is not the situation originally considered for the L-curve since in [93] the regularity constraint is enforced in the whole reconstruction domain. In our case, we expect that this "outside" constraint will help in the reconstruction of the sample, and an arbitrary high value for μ may be also appropriate. In practice, we found that a finite value for μ was most appropriate and, by a trial and error exploration, we chose the value $\mu = 10^7$. This value was considered in the sequel as the "optimal" value for our problem.

The tuning of the support of the thin film. In practice, the exact geometry of the thin film is not precisely known and the support $\overline{\mathcal{S}}$ needs also to be adjusted when one deals with experimental data. For sake of simplicity, we do assume that the thin film is a rectangular object only parametrized by its *unknown thickness* noted by ω. A strategy for the estimation of this thickness is now developed, mostly inspired by the "L-Curve" technique.

Let us consider a set of retrieved samples obtained with increasing thickness[8] of the thin film. Clearly, we do expect that the data-fidelity term $\mathcal{L}$ is *very large* when the thickness of the film is *underestimated*. Obviously, this data-fidelity term should get lower and lower as the thickness ω is increased and, we do also expect that this *rate* of decreasing will be different if ω is *underestimated* or *overestimated*. Here again, the plotting of the data-fidelity term *versus* the width of the film should exhibit L-shape and the "corner" should locate the width of the film, see Fig. 4.17 for an illustrative example. Interestingly, this strategy seems rather efficient in selecting an appropriate width for the sample.

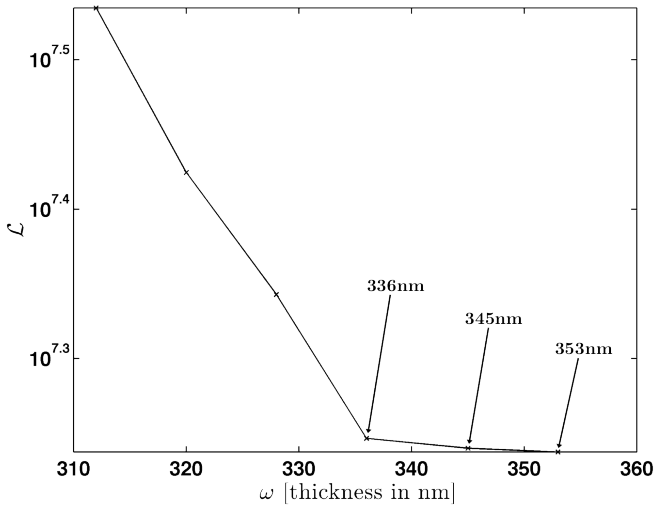

Figure 4.17: A selection of the support thickness value (regularization parameter) by means of the "L-curve". On the curve, we can distinguish two regions of different descent rates.

Still looking for a good initial-guess. With noisy data, even if the retrieved phase matches well the true phase when the inversion is initiated with the true numerical object (which is expected to be very close to the minimizer), we fail to obtain a satisfactory reconstruction when the initial estimate is only slightly different, even with the regularization term properly tuned. This situation is illustrated in Fig. 4.18 where the reconstruction obtained from an initial-guess that exhibits a slope of the phase in the nominal InGaAs layer that is 70% the one of the true object is shown. Clearly, we still need a strategy to providing a very good initial guess. In the

[8] In this experiment, the initial-guess and the regularization parameter μ are unchanged, the thickness ω being the only parameter under investigation.

next section, we will use the ingredient presented so far for the design of an *ad hoc* strategy providing such an initial guess.

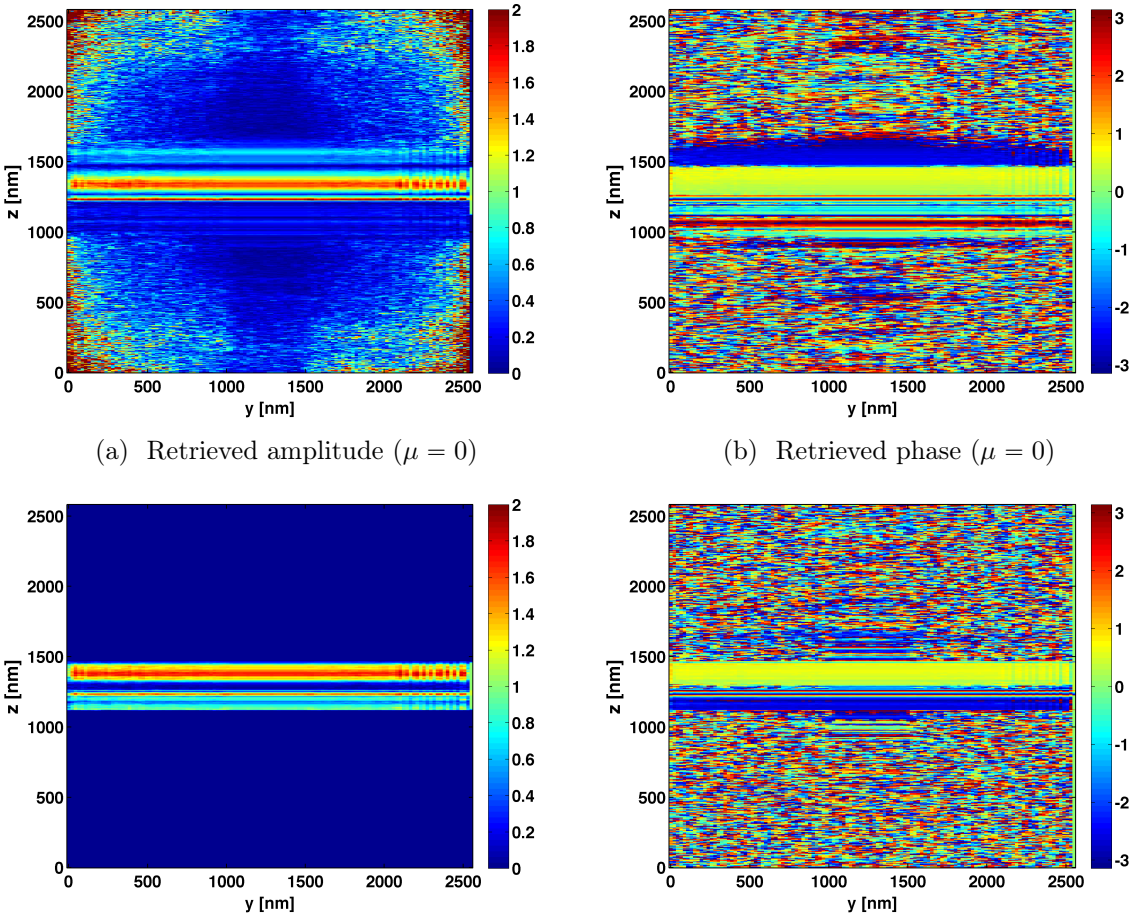

(a) Retrieved amplitude ($\mu = 0$)

(b) Retrieved phase ($\mu = 0$)

(c) Retrieved amplitude ($\mu = 10^7$)

(d) Retrieved phase ($\mu = 10^7$)

Figure 4.18: Cross-sections of the retrieved amplitude and phase when providing as initial estimate an object with $0.70 f_1$ of the nominal InGaAs phase slope and noisy data, for $\mu = 0$ and $\mu = 10^7$.

4.2.3 Towards a good initial-guess built from the dataset.

One of the salient features of the reconstruction artifacts is that the phase oscillations are related to the amplitude inhomogeneity, and *vice versa*. As a result, we do expect that making the amplitude smoother during the inversion will reduce the phase oscillations. This strategy seems appropriate for our problem since we gathered from Sec. 3.2 that the modulus within the InGaAs layer is only 20% higher than the one in the InP layers — in other words, *the modulus within the thin film is almost constant*.

An homogeneous modulus is a rather strong (real-space) constraint for our reconstruction problem. This constraint is indeed too strong since we would like to retrieve in the end the small modulus variations within the thin-film. However, *this constraint can help, as a first step for building a "good" initial-guess* that will be further improved, in a second step, by either the OS-PIE or the NCG algorithm.

Because we would like to build this initial-guess from the dataset, this first step is indeed also an iterative process relying on the OS update, given by relation (2.1.17). Since this update $\widetilde{\boldsymbol{\rho}}_{k+1}$ is subject to modulus inhomogeneity, it is corrected so that the modulus is homogenized in each update: the next constrained update is defined by

$$\boldsymbol{\rho}_{k+1;\mathbf{n}} \;=\; \begin{cases} \overline{\rho}_{k+1} \times \dfrac{\widetilde{\boldsymbol{\rho}}_{k+1;\mathbf{n}}}{|\widetilde{\boldsymbol{\rho}}_{k+1;\mathbf{n}}|} & \mathbf{n} \in \Omega \\ \widetilde{\boldsymbol{\rho}}_{k+1;\mathbf{n}} & \text{otherwise} \end{cases} \tag{4.2.7}$$

where $\overline{\rho}_{k+1}$ is the *homogenized modulus* within the thin-film[9]

$$\overline{\rho}_{k+1} \;:=\; \sum_{\mathbf{n}\in\Omega} \widetilde{\boldsymbol{\rho}}_{k+1;\mathbf{n}}.$$

Hereafter, the update (4.2.7) will be called a *modulus homogenization step* (MH step). Obviously, we note that the iteration (2.1.17)-(4.2.7) has to be initiated with a first estimate. We do expect, however, that the final result (*i.e.* the provided initial-guess) will be rather robust with respect to this first estimate, see below.

The strategy described above is clearly inspired from CDI in that a real-space constraint is added on the modulus of the retrieved object during the inversion step. However, this constraint is rather "crude" and whereas the constraining step (4.2.7) could be enforced repeatedly in each iteration, we also *give the opportunity to relax this constraint for a few tens of iterations* —in this case, the update $k \to k+1$ is just a conjugate gradient step given by $\boldsymbol{\rho}_{k+1} = \widetilde{\boldsymbol{\rho}}_{k+1}$. Fig. 4.19 present the resulting initial guess obtained with 80 MH iterations followed by 20 unconstrained updates ; in this case, a synthetic dataset corrupted by noise (with a maximum counts $\sim 10^4$) was used. The retrieved amplitude (and phase as well) approach more the profile of the limiting case of starting with the true object as initial estimate, noisy data and letting the inversion unconstrained (UN*). That means the object that minimizes the criterion is closer to the true object than before.

This is better illustrated on Fig. 4.20a where we can see the behavior of the criterion as a function of the number of iterations, for each of the three inversions respectively. The first curve corresponds to one hundred iterations without application of the modulus constraint (UN). On the top curve, the first eighty iterations are constrained and thus, the criterion values are elevated. As soon as the MH constraint is removed, the values directly go down, reaches the UN curve and decrease even further as it can be evidenced on Fig. 4.20d (zoomed region of the criterion for the last five iterations).

[9] Instead of providing an averaged modulus value $\overline{\rho}_{k+1}$ to all the pixels in Ω, one can provide precisely the expected modulus profile we have developed in Subsection 4.1.1. However, it should be underlined that this more "subtle" strategy results in artifacts if the position of the buried layer is mis-located.

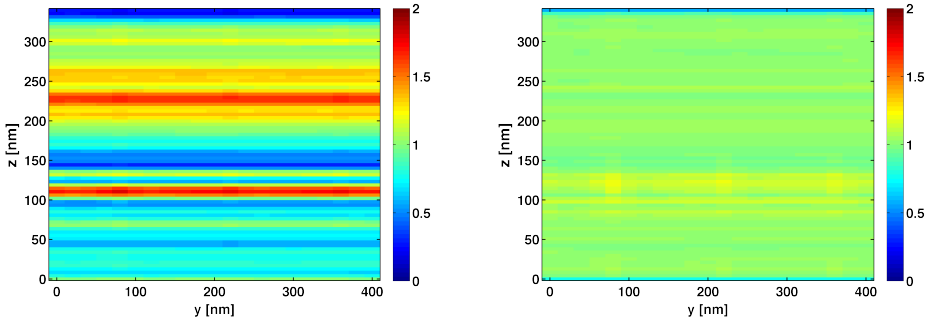

(a) Amplitude (**0MH**) (b) Amplitude (**5MH**)

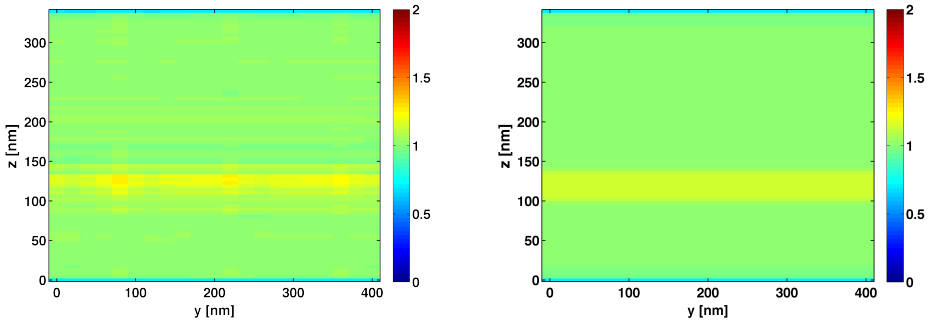

(c) Amplitude (**UN***) (d) Amplitude (**True object**)

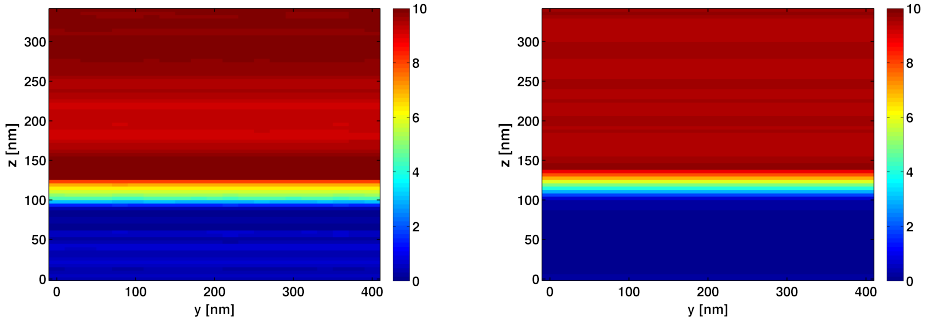

(e) Phase (**0MH**) (f) Phase (**5MH**)

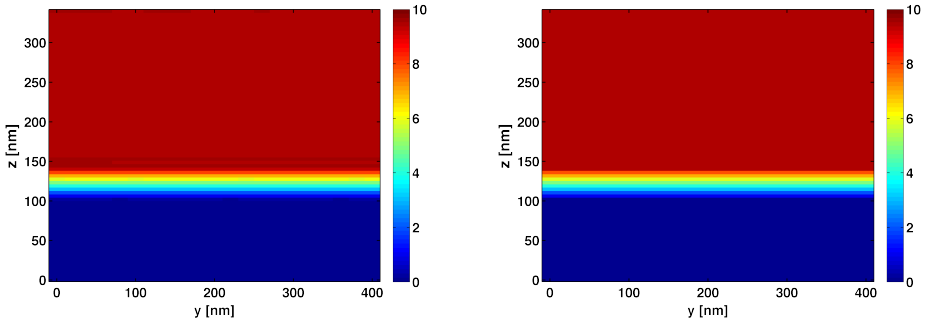

(g) Phase (**UN***) (h) Phase (**True object**)

Figure 4.19: The retrieved amplitude and phase for unconstrained and MH constrained iterations. The first three figures show the inversion results when using as initial estimate for the PRA a rough guess of the true object (slope=$0.70f_1$). The UN* result corresponds to the completely unconstrained inversion when using the true object as initial estimate. For all the inversions we have used noise-corrupted data.

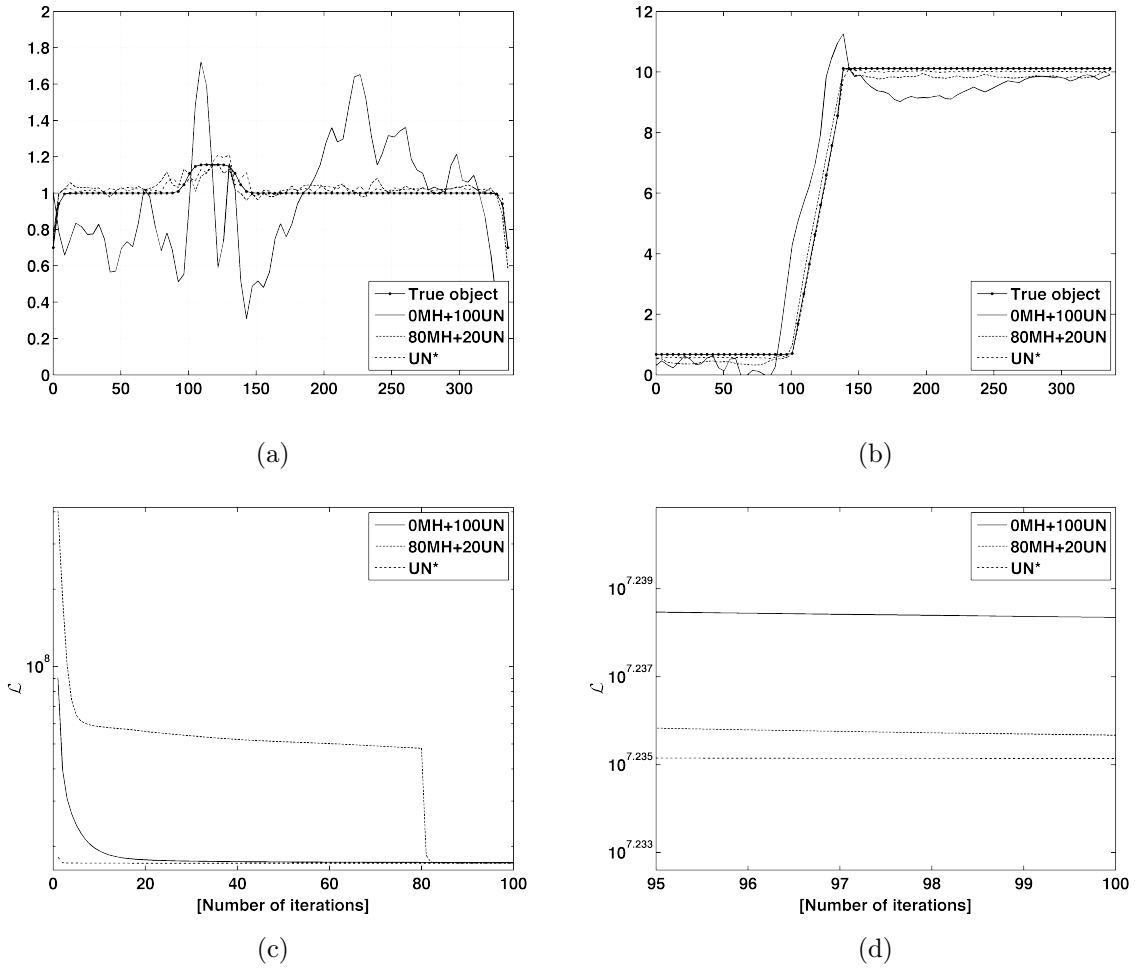

Figure 4.20: (a) Retrieved amplitude of the final reconstruction for the unconstrained and MH constrained inversion scheme, when using a rough initial estimate. Comparison with the completely unconstrained case when providing the true object as initial estimate and the amplitude of the true object. (b) Retrieved phase (*idem*). (c) The criterion as a function of the number of iterations for the three inversions. (d) *Idem* zoomed on the last five iterations.

4.3 As a conclusion: an optimized inversion strategy

After the development of a physical and numerical model for the InP/InGaAs crystal thin film, we described as well the physical process of measuring a 3D ptychographic dataset assembled by 2D Fraunhofer diffraction patterns in Bragg geometry. The description of this process contains the assumption of certain noise statistics, which is used in the inversion scheme when minimizing the data fidelity term. We saw that only minimizing the data fidelity term is not a simple task since the inversion results have been unsatisfactory and for this reason we incorporated the widely used approach of regularizing the obtained solution. The incorporation of regularization slightly improved the quality of the retrieved object, while the optimization of its parameters (support thickness and μ-value) turned out to be a matter of finding an empirical solution, rather than obeying the *L-curve* rule.

Nevertheless, even the addition of regularization was not sufficient for retrieving a satisfactory image, and for this reason we had to work in developing a suitable initial guess. This process we referred to as modulus homogenization, aimed in accelerating the OS convergence by providing extra a priori information concerning the modulus distribution (MH constraint). The outcome of

the MH process was then provided to the NCG algorithm as initial estimate, for a final stage of unconstrained iterations, where is going to hopefully gain by the small refinements of the NCG update. This optimized strategy is illustrated in Fig 4.21 where the 100 first iterations aim at constructing the initial-guess while the 100 following NCG iterations provide some additional refinements.

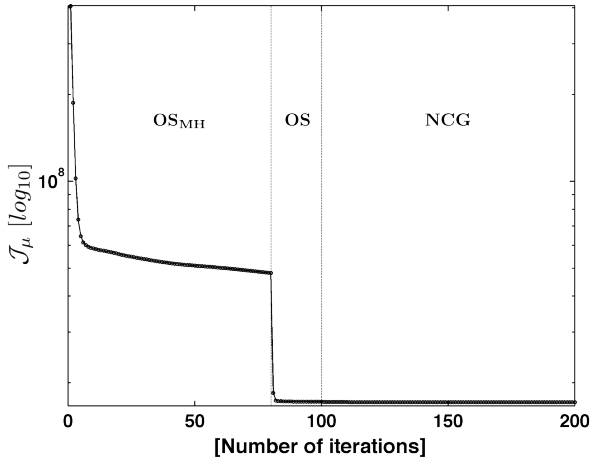

(a) The criterion of the complete inversion scheme. During the first eighty iterations we apply the MH constraint using the OS algorithm, the constraint is removed for the last twenty iterations and the outcome is then provided for one hundred more iterations to the NCG (no constraint applied).

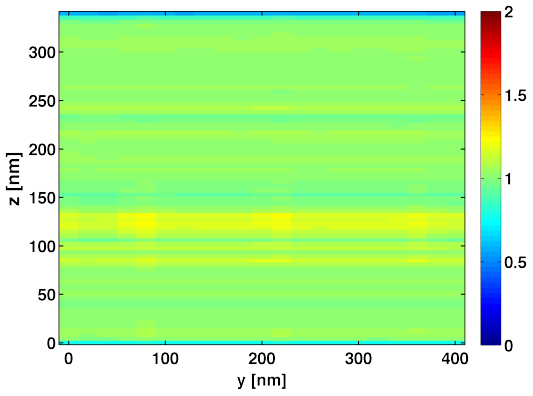

(b) Amplitude of the final reconstruction.

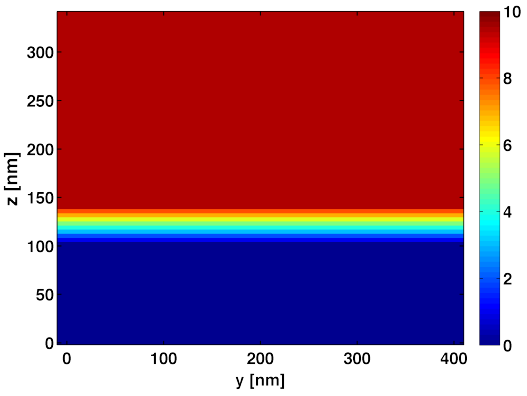

(c) Phase of the final reconstruction.

Figure 4.21: The optimized scheme proposed as the final inversion strategy of the experimental data [See for comparison Fig. 4.19].

In conclusion, we have shown that this strategy scheme is robust enough and can significantly overcome the stagnation problems that are encountered when starting the inversion with an initial guess which is far away from the true object. In the next chapter we will see that the additional implementation of the MH constraint (inside the OS routine) as a preparatory step for building a good initial estimate, in combination with the empirical optimization of the inversion process and a final amount of unconstrained cycles using the NCG algorithm, consist a good choice of inversion strategy for the given problem, and was indeed an appropriate methodology to tackle the inversion issues and achieve a satisfactory reconstruction result.

Chapter 5

Bragg ptychography on experimental data

Contents

In this chapter, we present and examine the results that are obtained using the optimized inversion strategy we presented in Chapter 4. The 3D reconstruction, obtained by the Bragg ptychography experimental dataset is first shown in the Fourier and in sample spaces. This aims at evaluating the overall quality of the obtained reconstructions. In the second section we have a more detailed description of the sample retrieved image. The observation of structural features that were not expected on this high-quality sample are shown to be linked to specific characteristics of the intensity patterns. Their relation with the retrieved structural features is investigated with the help of a numerical model, presented in Section 5.3. In the last section we discuss the impact of the obtained experimental results.

5.1 3D reconstruction on experimental data

In this section, we present the details of the inversion strategy together with an overall description of the 3D reconstruction.

5.1.1 Inversion strategy

In the previous chapter, we presented the results of an extended study performed on synthetic, noise-corrupted data, aiming at validating the inversion strategy. We saw that the unconstrained use of the OS algorithm gave dissatisfying results, with noisy reconstructions both in terms of retrieved amplitude and phase, as well as high values of the criterion [Section 4.2]. This led

us to the additional implementation of a regularization approach, which favors solutions inside a reconstruction volume of a planar film, and the incorporation of a "weighting" penalization parameter (μ). After the optimization of the two regularization parameters, the addition of an extra amplitude constraint dramatically improved the quality of the reconstruction [Section 4.2.3].

Having that in mind, we chose for the inversion of the experimental data, a hybrid strategy which consisted in 1000 iterations using the OS algorithm, for which the amplitude constraint was applied during the first 800 iterations, while for the remaining 200 iterations the constraint was removed. The result of this process provided a high-quality estimate as input to the NCG algorithm, which ran for 1000 additional iterations [See Fig. 5.1]. During both inversion steps (OS and NCG) regularization was applied, penalizing the reconstruction for every pixel outside the planar support. The thickness of the support was fixed at a slightly larger value than the actual film thickness at 353nm (along z), and the regularization parameter was $\mu = 10^7$. For the amplitude constraint, we used $a_h \approx 1$ and applied it as described in Chapter 4. The computing time for the entire inversion was 117h (around 3mins/iteration for the OS and 4mins/iteration for the NCG).

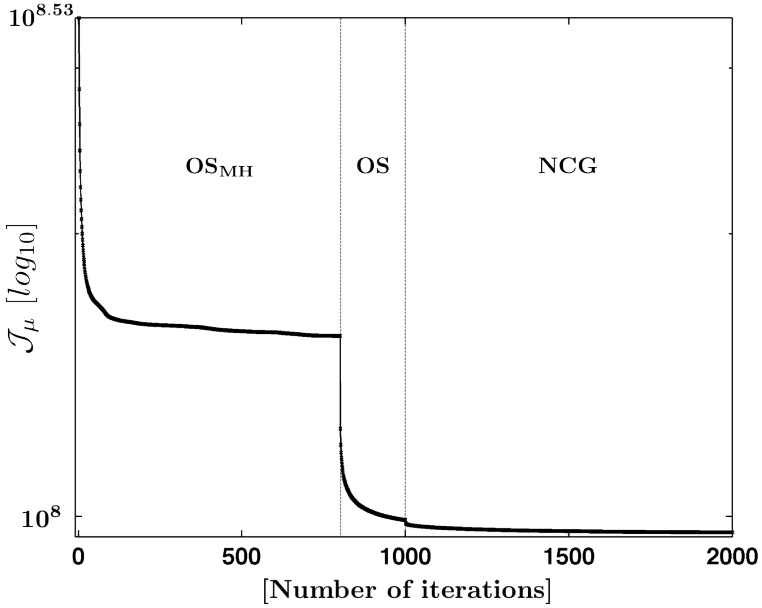

Figure 5.1: Evolution of the criterion during the reconstruction based on the experimental data. The different steps used in the optimized inversion procedure are indicated on the graph.

5.1.2 Retrieved data fidelity

The inversion process aims at finding a 3D complex-valued object that satisfies the reciprocal space constraints, *i. e.* the data. Hence, a direct index for the evaluation of the data fidelity term seems naturally to be the criterion of Eqn. (2.1.13) shown above. However it is not an absolute reference index. In addition to that, since it is a quantity summed over the entire number of illuminated positions, it provides an average value for the complete reconstruction despite the deviation of its values from one position to another.

For those reasons, visually comparing the measured experimental intensity patterns with the ones produced by the retrieved object at each scan position, is a good way to evaluate the reconstruction. For sake of simplicity, six specific beam-to-sample positions have been chosen, which are considered as our reference positions all along this chapter. On Figs. 5.2, 5.3, 5.4 and

5.5, the proposed intensity patterns are compared to the experimental intensities. The two first figures show the retrieved intensity in the detector plane, taken at two different points of the rocking curve, corresponding to the InP and the InGaAs peaks respectively, while the third one shows the retrieved intensity in the (q_x, q_z) plane.

In Fig. 5.2, which presents the obtained results in the vicinity of the intense InP peak, we can see that the proposed diffraction patterns are well reproduced with respect to the experimental data, especially in the positions which demonstrate the expected phase profile (away from the tilted area of the crystal film). Nevertheless, the fitting is surprisingly good even for some among the tilted crystal positions, like position 9 [See Fig. 5.2b]. In particular, the overall shape, position and internal intensity distributions of the InP peak are well reproduced by the found solution, especially in the high photon counts. This is no more the case at the less intense InGaAs peak, where the shape and position are well reproduced by the solution, while the structural details of the intensity pattern are most of the time missing [Fig. 5.3]. This behavior suggests that a satisfying convergence of the inversion procedure was achieved in the InP layer, while the fine structural details related to the InGaAs peak could not always be retrieved. Finally, the views shown in Figs. 5.4 and 5.5 allow to confirm the good agreement between the shapes, positions, spreading of the Bragg peaks produced by the found solution and the measured ones.

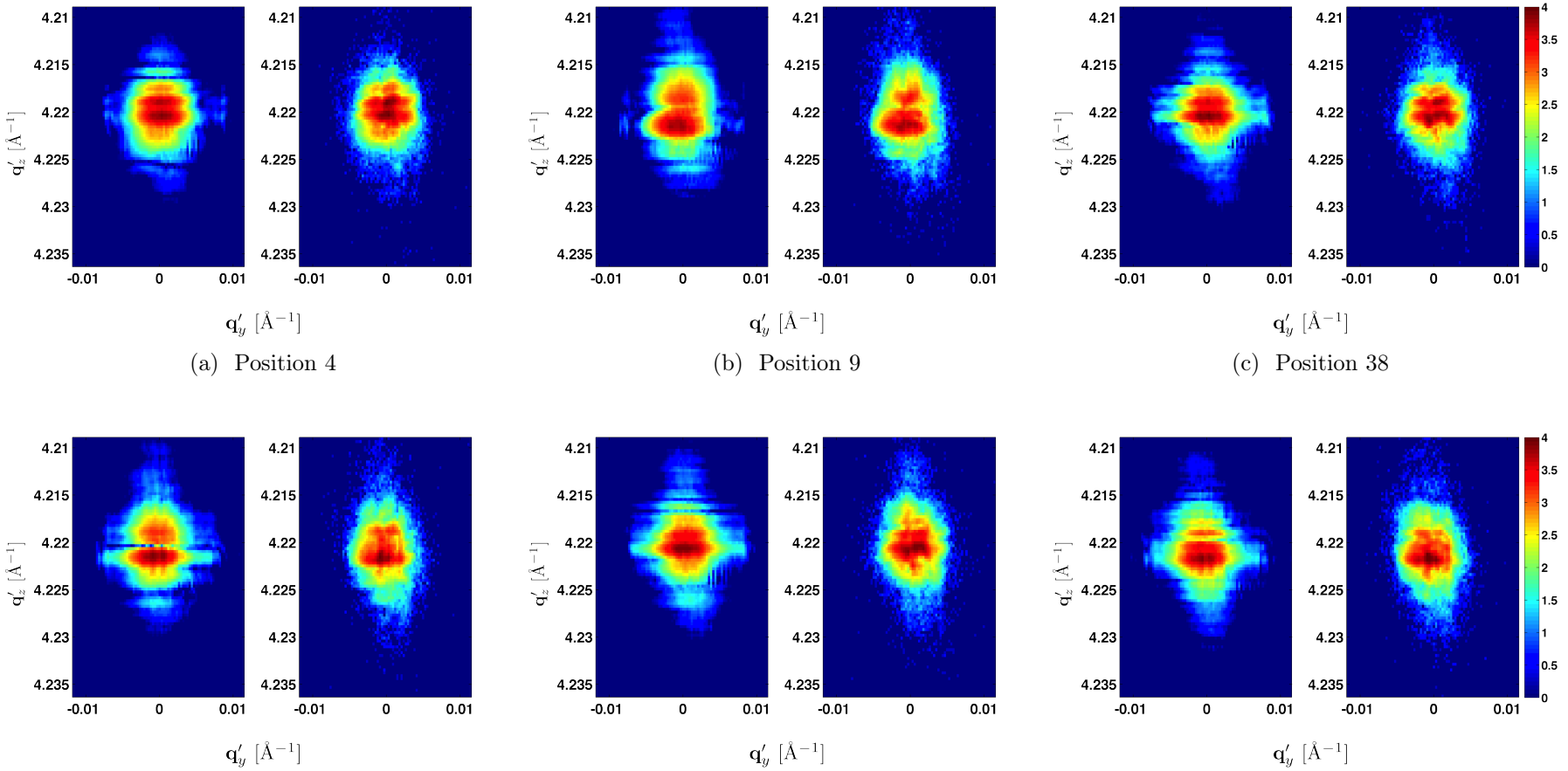

(a) Position 4 (b) Position 9 (c) Position 38

(d) Position 53 (e) Position 70 (f) Position 77

Figure 5.2: InP Bragg peak: on the left of every figure, we can see the proposed intensity patterns by the PRA compared to the corresponding measurement on the right, at different positions of the ptychography scan.

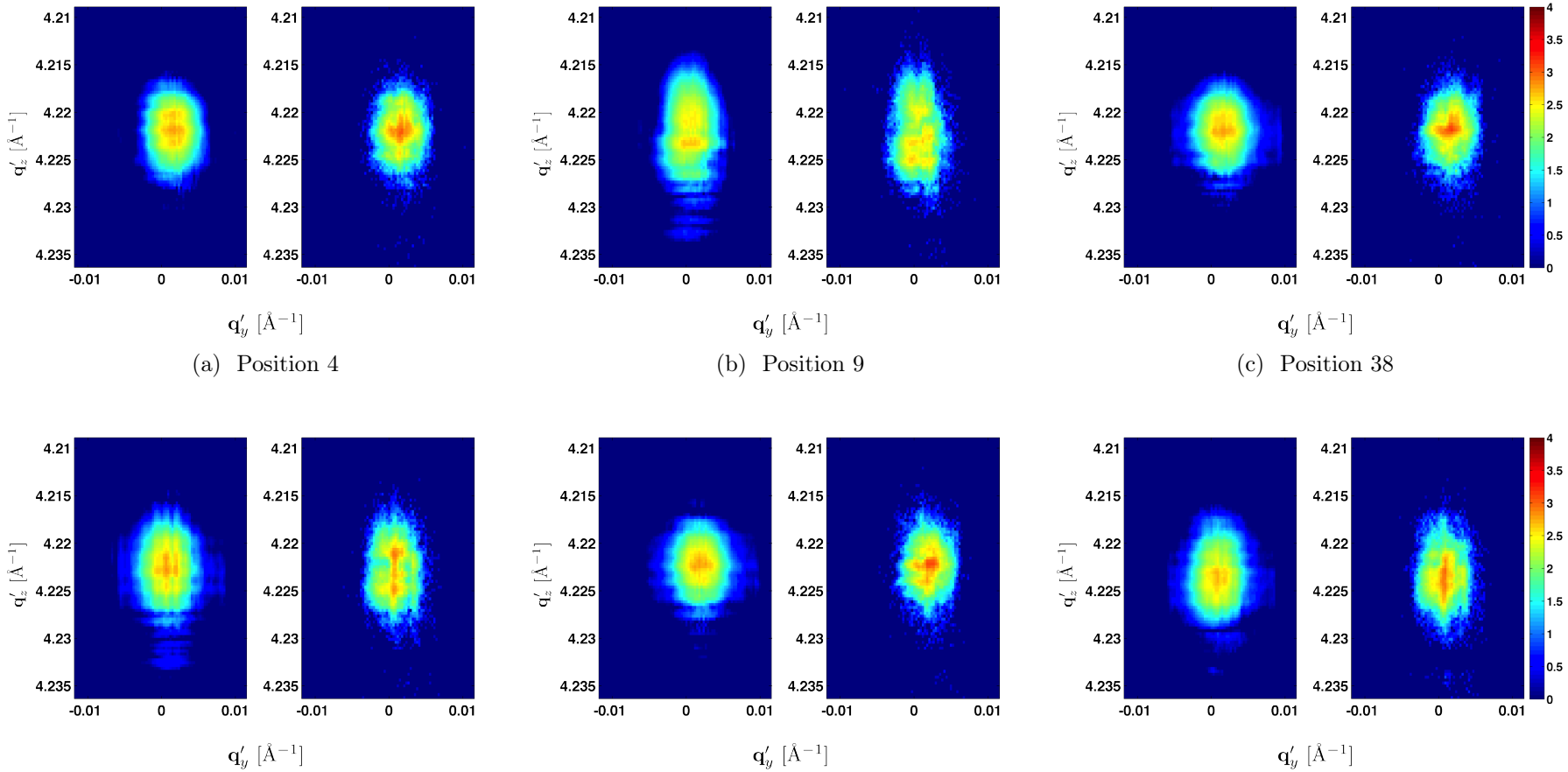

(a) Position 4 (b) Position 9 (c) Position 38

(d) Position 53 (e) Position 70 (f) Position 77

Figure 5.3: InGaAs Bragg peak: on the left of every figure, we can see the proposed intensity patterns by the PRA compared to the corresponding measurement on the right, at different positions of the ptychography scan.

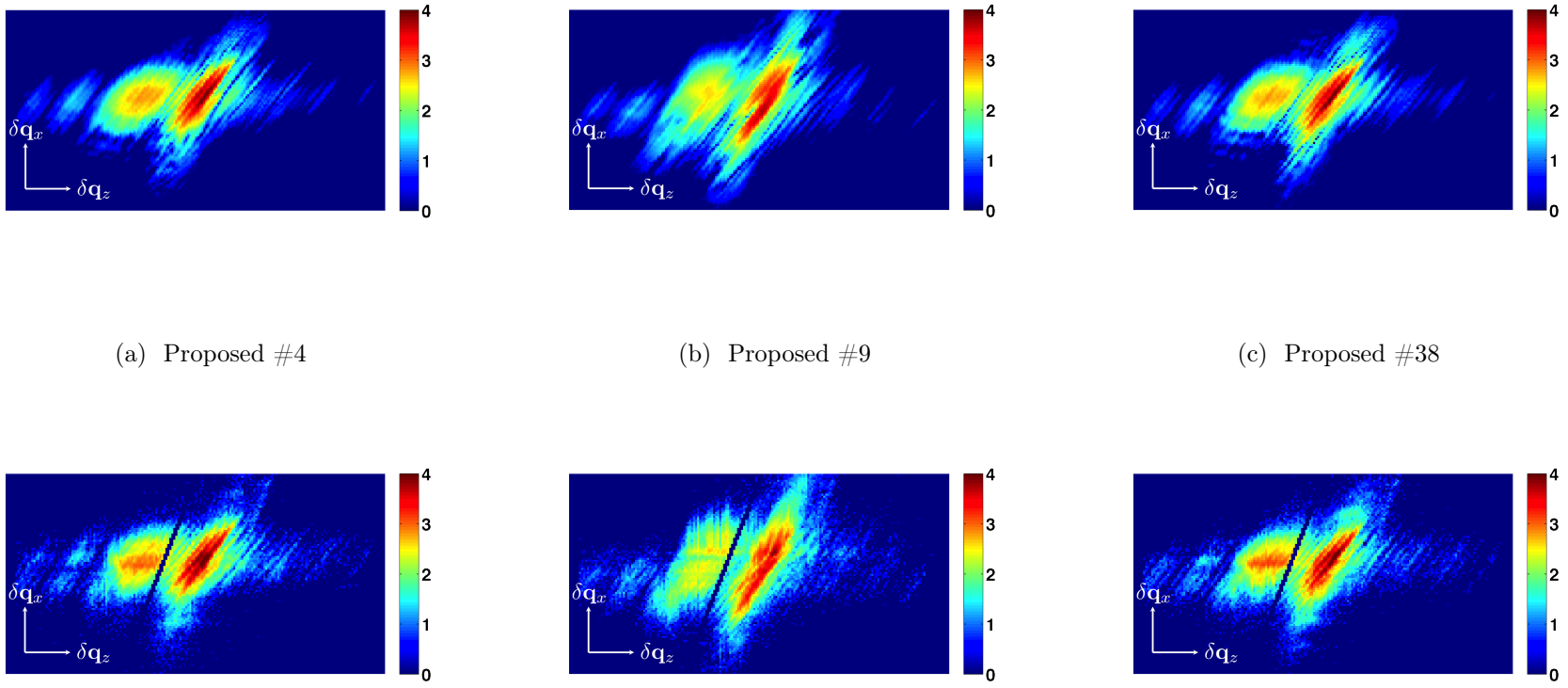

(a) Proposed #4 (b) Proposed #9 (c) Proposed #38

(d) Measured #4 (e) Measured #9 (f) Measured #38

Figure 5.4: Intensity patterns shown on the $\mathbf{q}_x\mathbf{q}_z$ plane, taken at different positions of the ptychography scan ($\delta q_x = 0.1022nm^{-1}, \delta q_z = 0.1055nm^{-1}$).

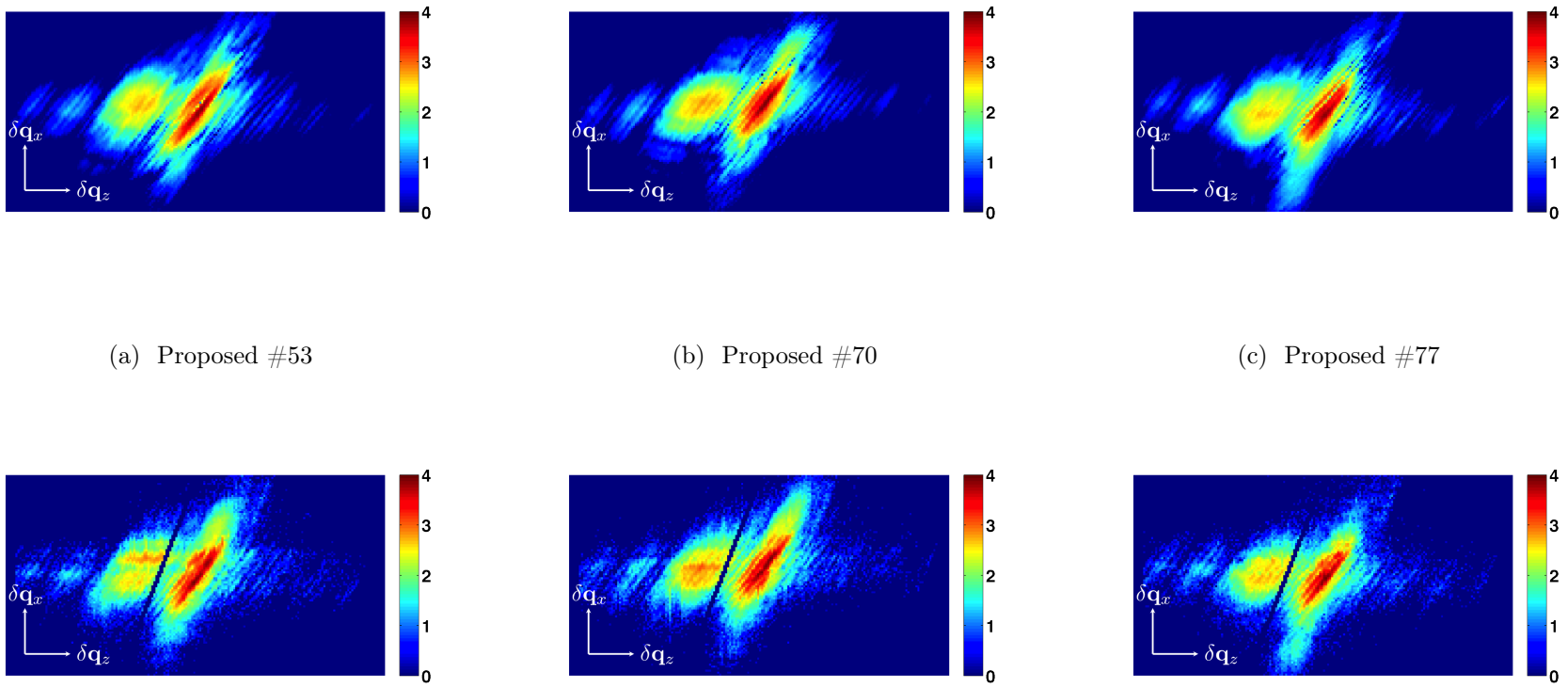

(a) Proposed #53 (b) Proposed #70 (c) Proposed #77

(d) Measured #53 (e) Measured #70 (f) Measured #77

Figure 5.5: Intensity patterns shown on the $\mathbf{q}_x\mathbf{q}_z$ plane, taken at different positions of the ptychography scan ($\delta q_x = 0.1022nm^{-1}, \delta q_z = 0.1055nm^{-1}$).

5.1.3 3D retrieved image

The inversion of the Bragg ptychography dataset allows to retrieve the complex-valued electron density, as described in Chapter 2. The retrieved 3D sample structure is now presented in Fig. 5.6, where the 3D amplitude and phase are shown. The found solution obtained in the nonorthogonal space (the conjugate to the detector space) is transformed so that it can be plotted into the laboratory frame. The ptychography scan, performed on a restricted area of the whole continuous film, allows to image only a small volume of the film, presenting a parallelepiped shape. Due to the shallow angle of incidence ($\theta_B = 16.38°$), the volume is elongated along the beam-footprint direction. Moreover, on the border of the scan, the total impinging intensity is smaller than in the center, and as a result those regions are more noisy. For this reason, we kept only the part of the reconstruction which contains the most reliable phase information and which corresponds to the parallelepiped volume of Figure 5.6. The internal distribution of amplitude and phase are shown on two 2D cross-sections, one along the parallel and one along the perpendicular to the beam-footprint direction.

The retrieved amplitude presents important fluctuations - much more important for the retrieved amplitude than the phase - a common issue in phase retrieval problems [61, 40] which has often been solved using uniformity constraints on the retrieved amplitude [30]. On the opposite, the retrieved phase of the 3D reconstruction shown in Fig. 5.6b, is in good agreement with the expected physical model we have derived in Section 4.1. In particular, the thickness values of the three layers are retrieved with a good agreement with respect to their nominal structural values. The position of the InGaAs layer within the InP material is correct as well.

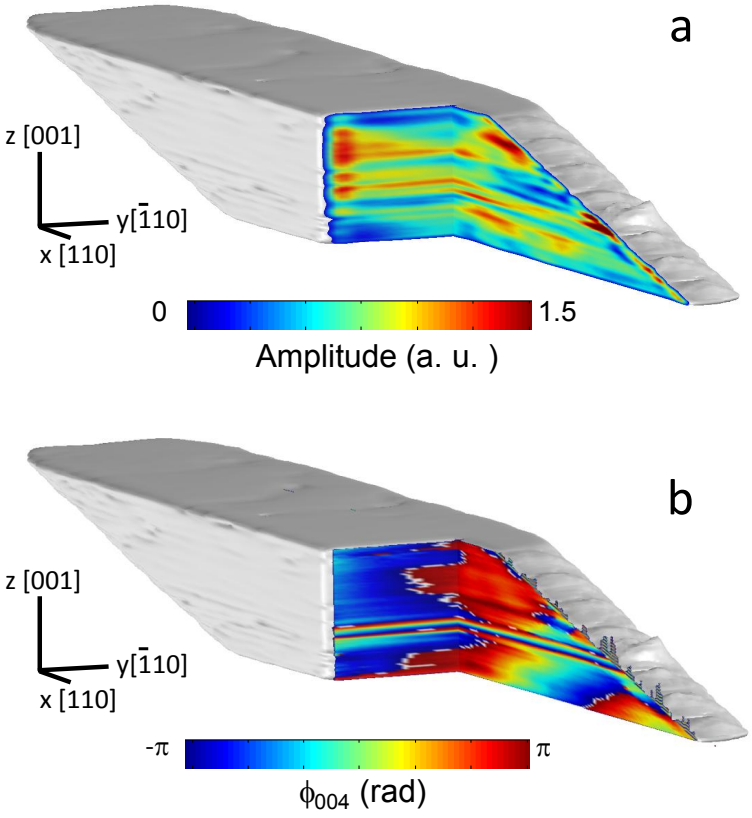

Figure 5.6: 3D representation of the reconstruction. The isosurface corresponds to isovalue=0.6. The shape of the volume is inclined due to the Bragg geometry, where the incidence angle is $\sim 16°$.

This is further emphasized with the extraction of the strain component ϵ_{zz}, obtained from the 3D phase map. After unwrapping the phase, a task usually performed by dedicated algorithms [95] and which provides the retrieved phase in its actual range and not multiple times wrapped in $[-\pi,\ \pi]$, we apply Eqn. (4.1.2) in its differentiated form, that is

$$(4.1.2) \ \Rightarrow \ \frac{\partial \Phi}{\partial z} = \epsilon_{zz} |\mathbf{G}_{004}| \ \Rightarrow \ \epsilon_{zz} = \frac{\frac{\partial \Phi}{\partial z}}{|\mathbf{G}_{004}|} \tag{5.1.1}$$

The result is presented in Fig. 5.7, where we can see the calculated strain map for the same region as in the figure above. Although we can see some fluctuations on the ϵ_{zz} maps, the general profile is quantitatively in agreement with our expectations regarding the strained InGaAs layer. The 1D profile extracted from the 3D volume shows that the strain value is retrieved with a good accuracy with respect to the nominal value. Moreover, the full width of the InGaAs layer, slightly larger than the nominal one, allows to evaluate the vertical resolution, which is estimated to about 7 nm.

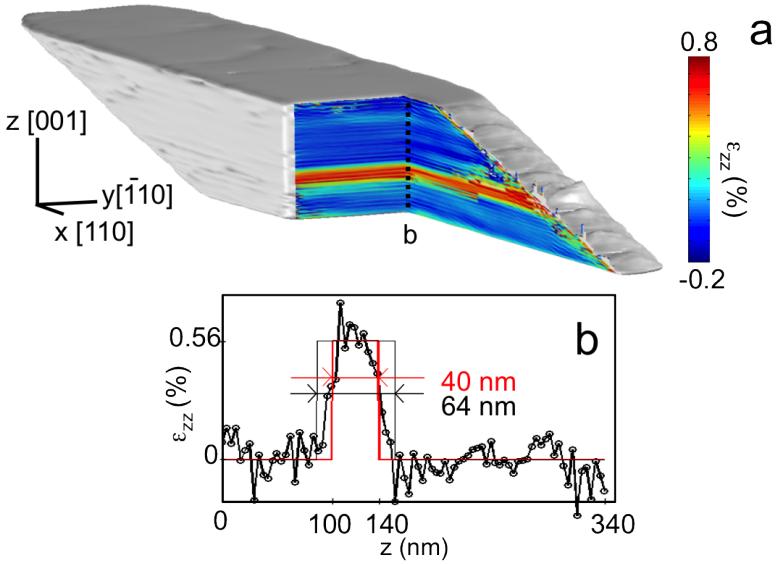

Figure 5.7: 3D representation of the reconstruction with plotted the retrieved ϵ_{zz} strain component.

5.2 Detailed analysis of the 3D retrieved image

5.2.1 Phase maps

In order to perform a more extensive examination of the retrieved solution, we now proceed with the investigation of 2D cross-sections taken across the 3D reconstruction. The axis orientation together with the illumination positions are defined in Fig. 5.8. The wrapped phases are plotted onto 2D planes either parallel to the yz plane, taken along x (Fig. 5.9), or on xz planes, taken along the y axis (Fig. 5.10).

On most of the retrieved volume, the phase profile is behaving as expected: the phase values are quite constant on the two InP layers and the InGaAs layer presents a constant phase gradient. However, a strong modification of the phase profile is evidenced in an area around $x = 1500$ nm and $y = 400$ nm. This phase feature can be roughly described as a gradual increase of the phase along the y axis and as positive phase bump along the x axis. This additional phase profile leads to the bent appearance of the InGaAs layer. Note that this sample part was investigated with illumination position 9 and its neighboring positions, as indicated in Figs. 5.8 and 5.11. In this

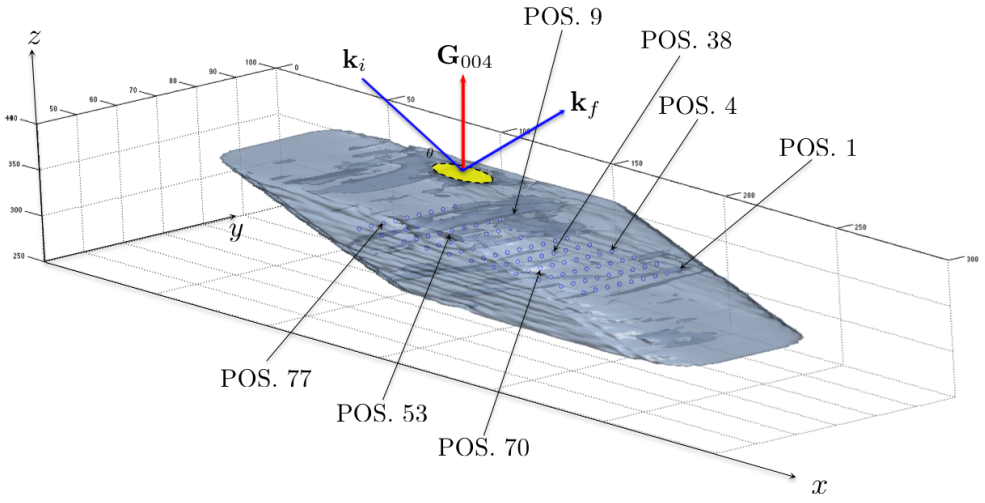

Figure 5.8: Transparent isosurface of the reconstructed amplitude (isovalue=0.6). The sample volume is represented in the orthogonal (x, y, z) reference frame. With yellow we can see the "effective" footprint (in scale) of the beam and with blue dots the scan positions taken in the center of the illumination and the middle of the sample depth, with $\mathbf{k}_i, \mathbf{k}_f$ the incident and diffracted beam.

region, the diffraction patterns present a splitting of the InGaAs Bragg peak together with an important elongation of the InP and InGaAs peaks [See Fig. 5.4 and 5.5].

5.2.2 Tilts of crystal planes

The features observed in the reciprocal space and along the retrieved phase map are indicating the presence of crystalline plane rotations. The rotation angles can be easily extracted from the 3D phase, using Equation 4.1.9. In a more general notation which includes tilt components around two different axes of rotation, it writes:

$$\delta_{i+1} = \sin^{-1}\left(\frac{\partial_i \Phi}{\mathbf{G}_{004}}\right), \text{ with } \partial_i = \frac{\partial}{\partial i}, \; i = x, y \tag{5.2.1}$$

Thus, by calculating the partial derivatives $\frac{\partial \Phi}{\partial x}, \frac{\partial \Phi}{\partial y}$ of the 3D phase map, we can estimate the tilt maps, δ_y or δ_x, that correspond to rotations around the y and x axis, respectively. The detailed behavior of the δ_x distribution is shown in Figs. 5.12,5.13 and 5.14, while similar plots obtained for δ_y are presented in Figs. 5.15, 5.16 and 5.17.

As seen with the analysis of the dataset, their behavior is not homogeneous but presents spatial variations. For both δ_x and δ_y, we observe that the volume can be divided in two regions. On the larger x side, the tilts are rather constant, taken as an orientation reference and therefore being equal to 0 in average. On the other region corresponding to the lower values of x, the δ_x tilt value increases to about $0.02°$. For δ_y, the tilt is first decreasing down to $\approx -0.02°$ before increasing up to about $0.02°$, from the right to the left of the retrieved areas along x. Those behaviors are in agreement with the angular motion of the Bragg peaks observed in the data set, as detailed below. Interestingly, the typical tilt values obtained from the inversion process are in good agreement with the tilt value estimated from the splitting of the Bragg peak.

5.3 Introducing a crystal plane tilt model

In order to go deeper in the understanding of the features observed in the retrieved phase map and in the corresponding tilt map, we now introduce a numerical model taking into account a local rotation of the probed crystalline plane.

5.3.1 The crystal plane tilt model

The discrepancies observed between the defect-free model and the experimental data invoke the presence of spatially localized rotations of the crystalline planes. In chapter 4, we introduced a model that we used to account for those tilts. We showed that a local tilt expresses itself as an additional displacement field component u_t, varying linearly with the spatial coordinates perpendicular to the tilt axis. For a tilt corresponding to the rotation of the crystal planes around the y axis, u_t writes

$$u_{t,001}(x, z, \delta) = x \sin\delta - z\,(1 - \cos\delta) \tag{5.3.1}$$

from which we can derive the phase offset $\phi_{t,004}$ associated to the $\mathbf{G}_{004}$ Bragg vector

$$\phi_{t,004}(x, z, \delta) = |\mathbf{G}_{004}| \times \big(x \sin\delta - z\,(1 - \cos\delta)\big). \tag{5.3.2}$$

This model was used to introduce a local tilt in the numerical mode initially built on the nominal structural parameters of the InP nanostructured layer. Several configurations were tested, where one or two tilts were introduced, with different values for δ, tilt width along x and vertical extension limited to some or all the InP and InGaAs layers. On Fig. 5.18, we present a series of phase profiles, where a crystalline plane rotation has been introduced. It consists in a positive and then negative rotation of the plane, extending along x over a distance L, for 2 values of δ. The intensity profiles have been calculated for different positions of the incoming beam, whose centers are schematically represented by the colored circles.

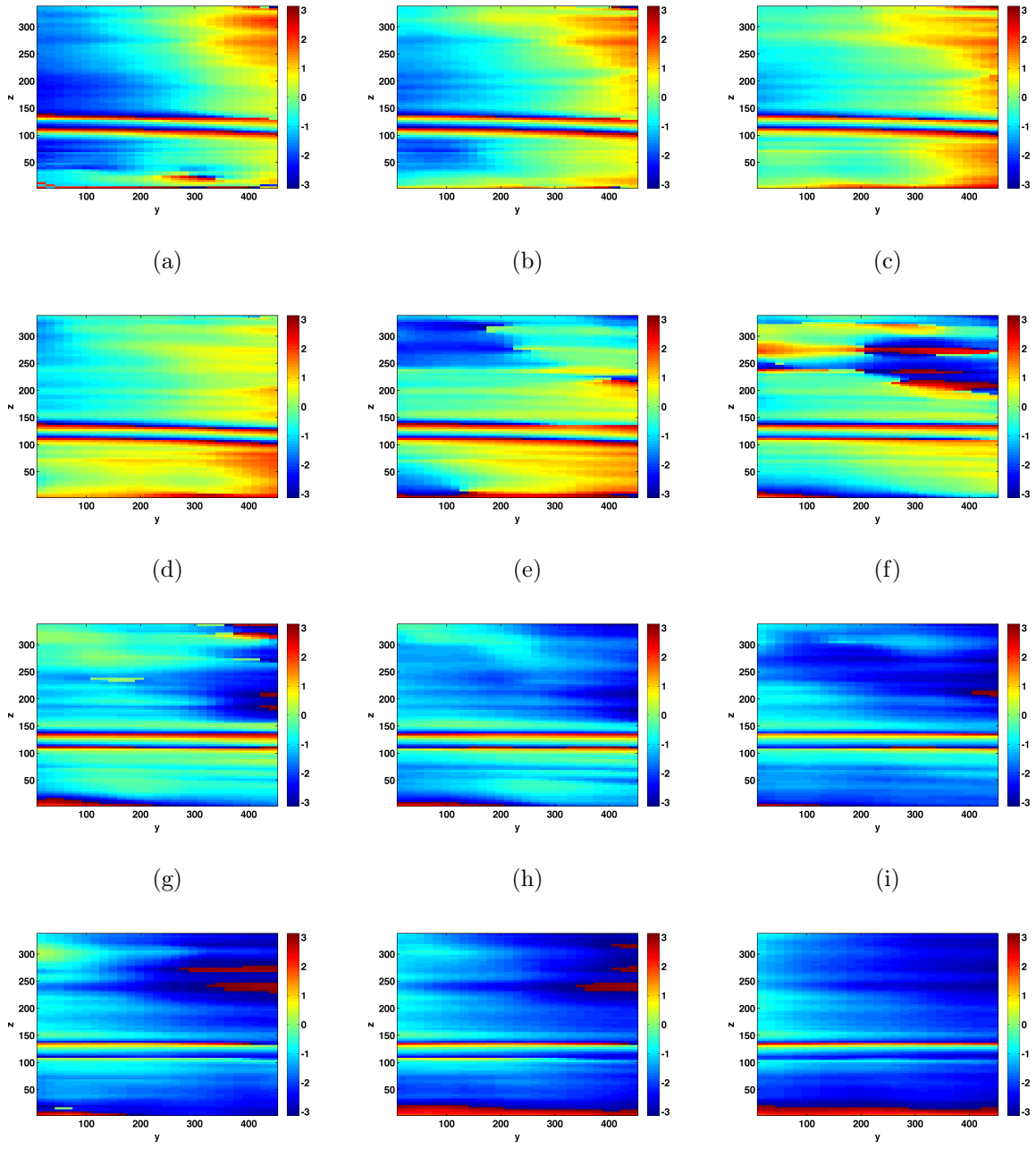

Figure 5.9: Plots of the retrieved wrapped phase on successive yz planes, taken along the $x > 0$ axis. On the two InP layers (top and bottom) the retrieved phase is expected to be constant, while inside the InGaAs layer a linear phase is expected. Due to the total angle difference of $\Delta\Phi \approx 9.5$rad in the entire thickness of the InGaAs layer the phase is wrapped in the value space of $[-\pi, \pi]$.

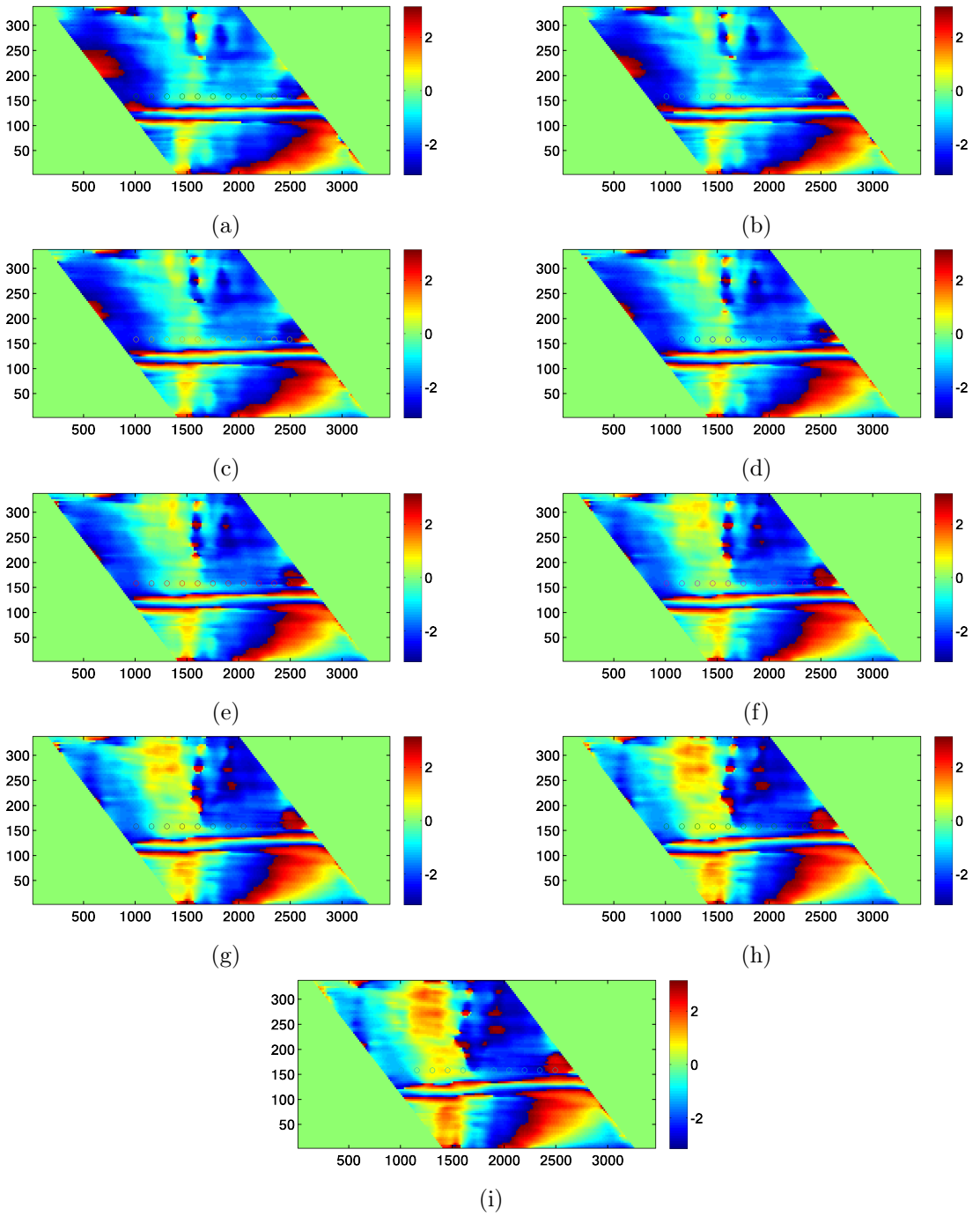

Figure 5.10: Plots of the retrieved wrapped phase taken on successive xz planes, along the $y > 0$ axis.

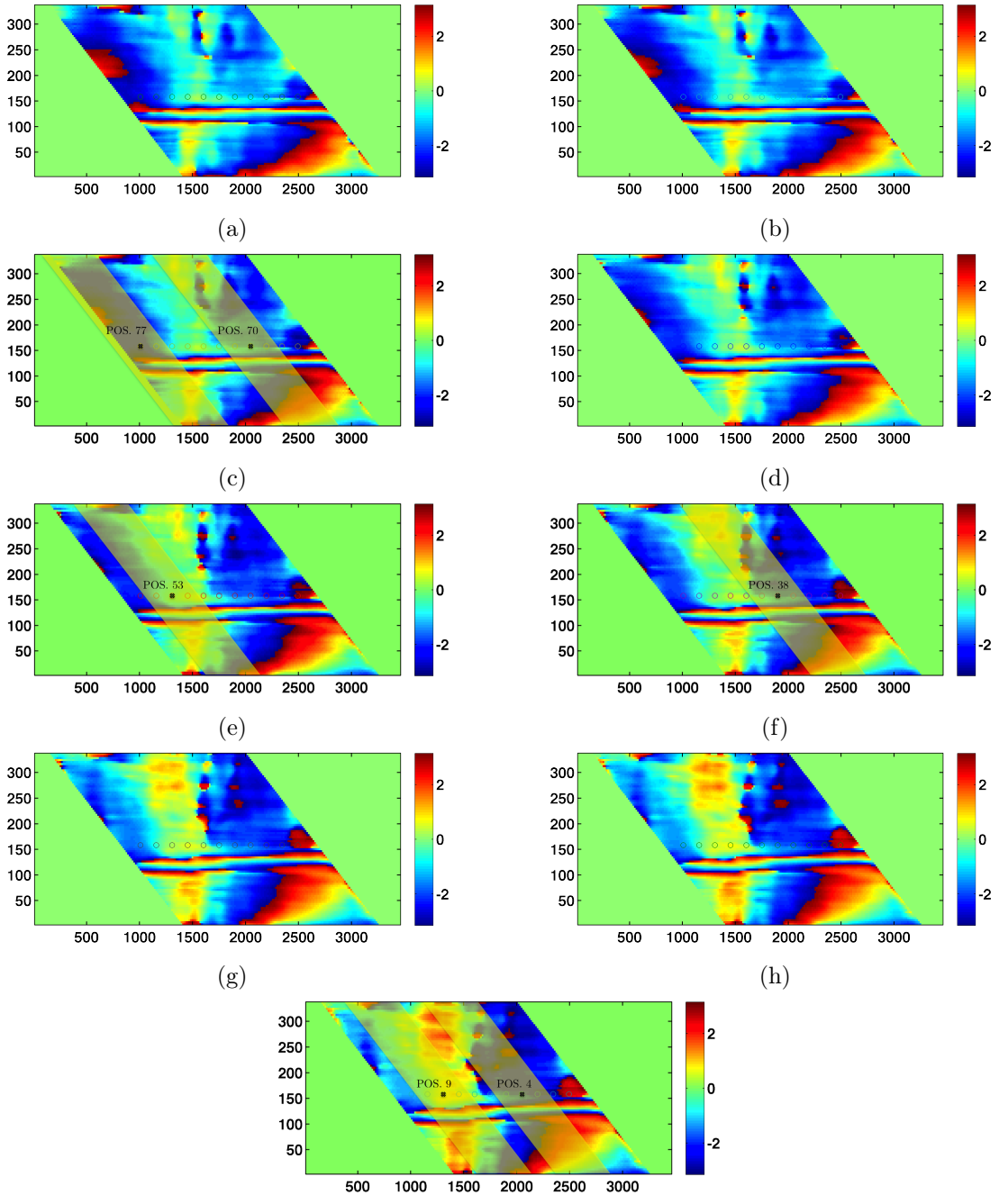

Figure 5.11: Plots of the retrieved wrapped phase taken on successive xz planes, along the $y > 0$ axis. The rectangles correspond to the diffracting volume which mainly contributes to the formation of the measured intensity patterns (at positions 4,9,38,53,70,77). The dots indicate the centers of the ptychography scan - beam positions.

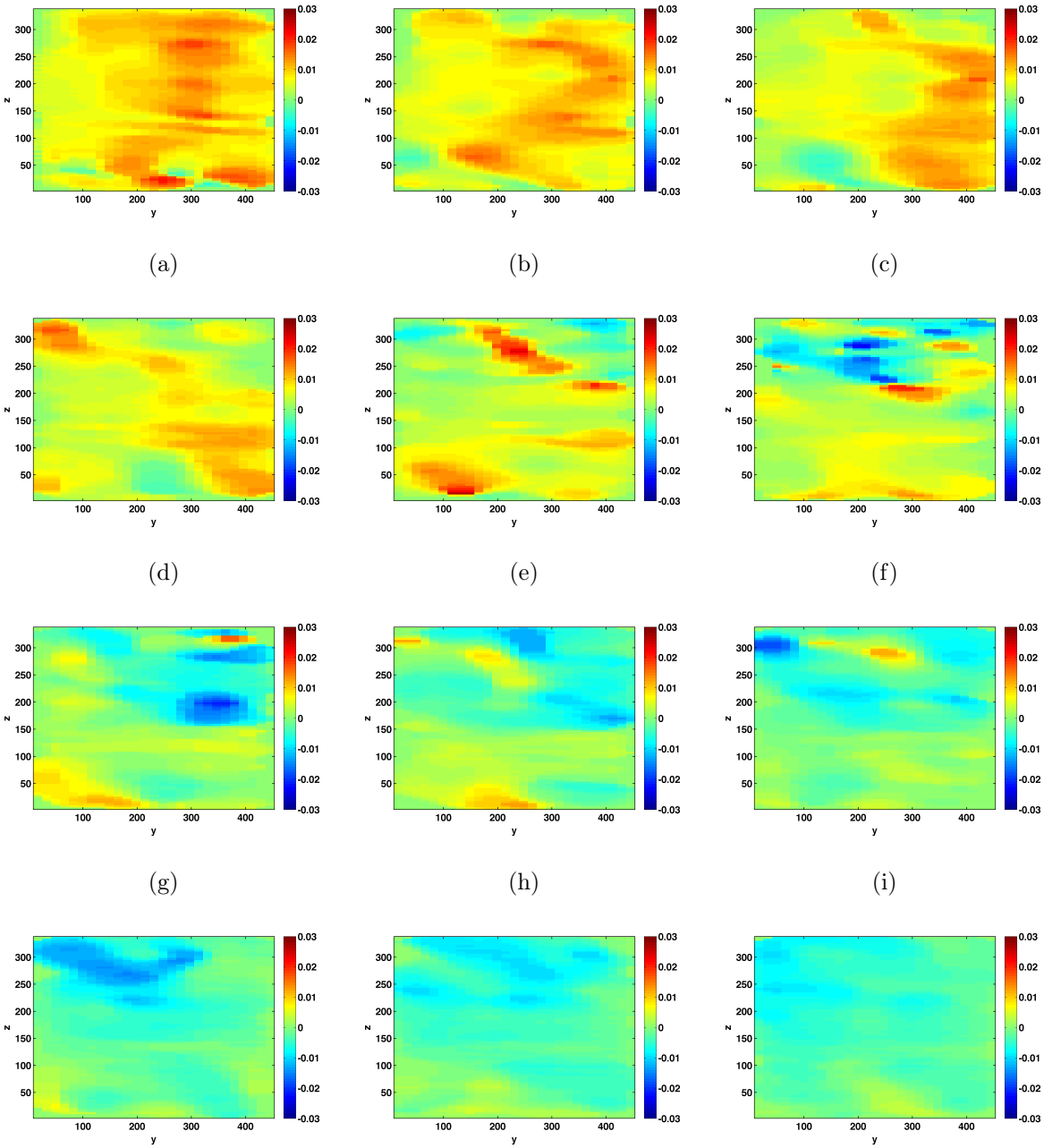

Figure 5.12: Crystal tilt δ_x correponding to the crystal plane rotation around the x axis, shown at different yz planes ($\partial\Phi/\partial y$). The shown quantity is calculated using Equation (5.2.1), with $i = y$.

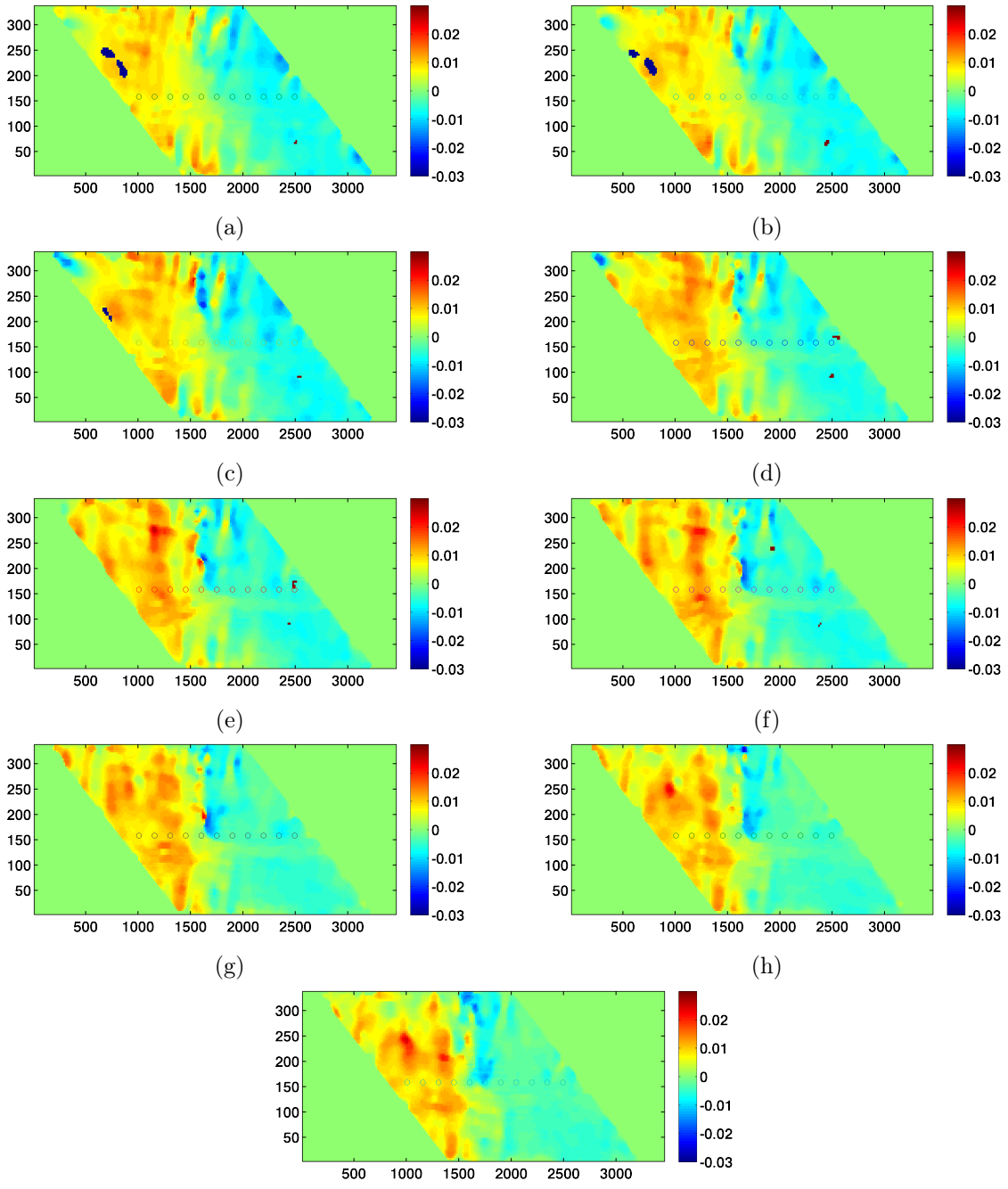

Figure 5.13: Crystal tilt δ_x correponding to the crystal plane rotation around the x axis, shown at different xz planes ($\partial\Phi/\partial y$).

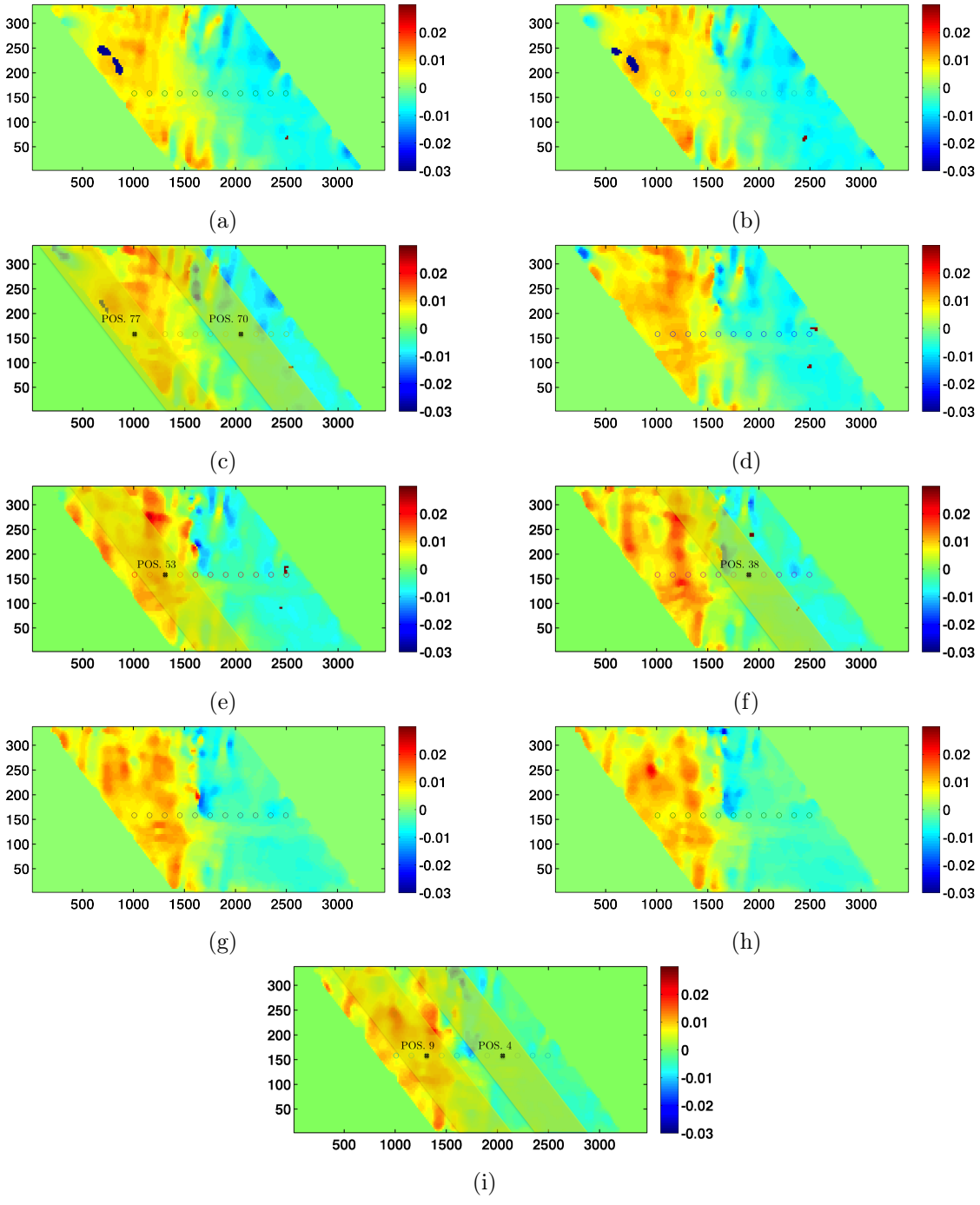

Figure 5.14: Crystal tilt δ_x correponding to the crystal plane rotation around the x axis, shown at different xz planes. The rectangles correspond to the diffracting volume which mainly contributes to the formation of the measured intensity patterns (at positions 4,9,38,53,70,77). The dots indicate the centers of the ptychography scan - beam positions.

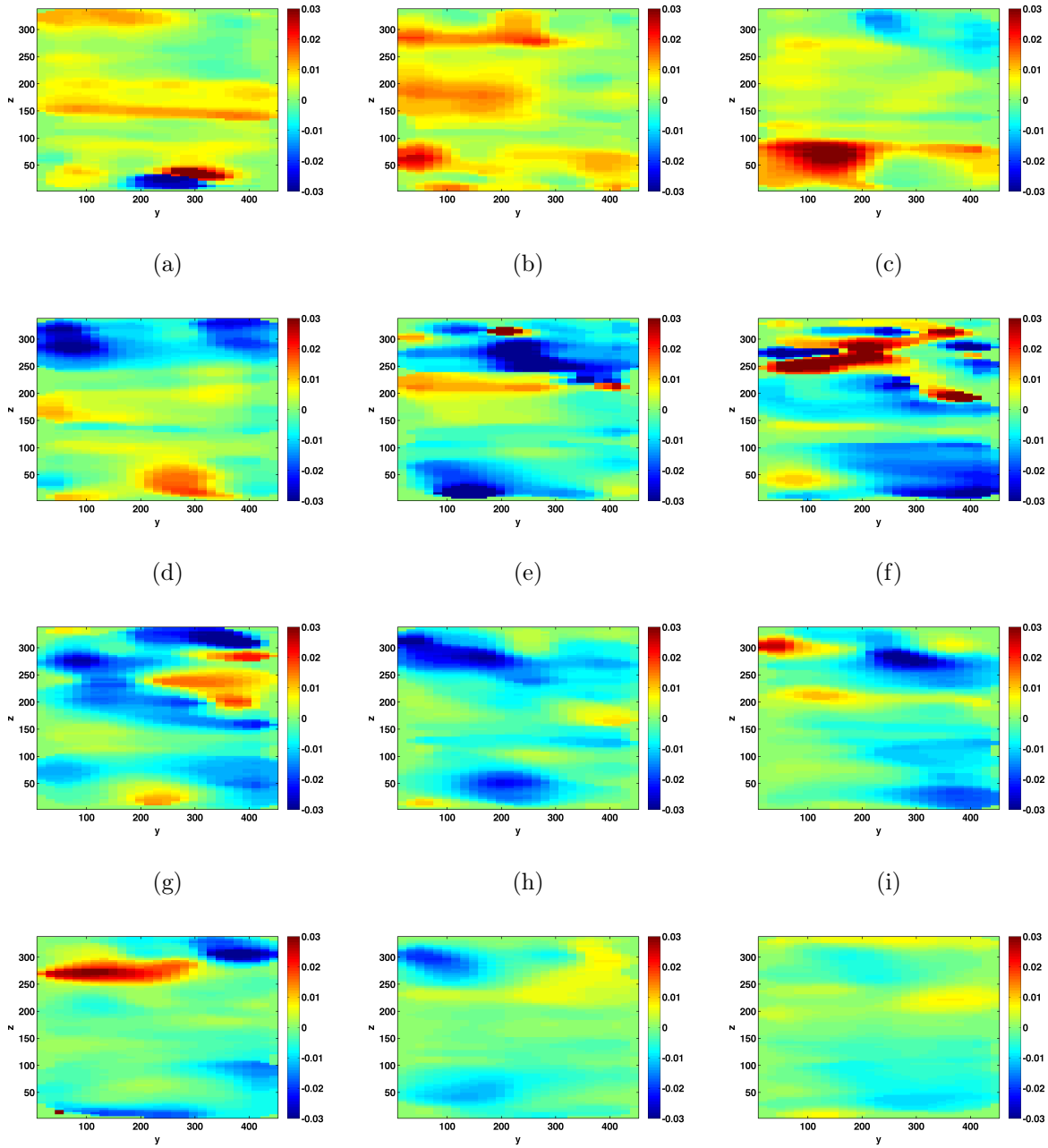

Figure 5.15: Crystal tilt δ_y correponding to the crystal plane rotation around the y axis, shown at different yz planes ($\partial\Phi/\partial x$).The shown quantity is calculated using Equation (5.2.1), with $i = y$.

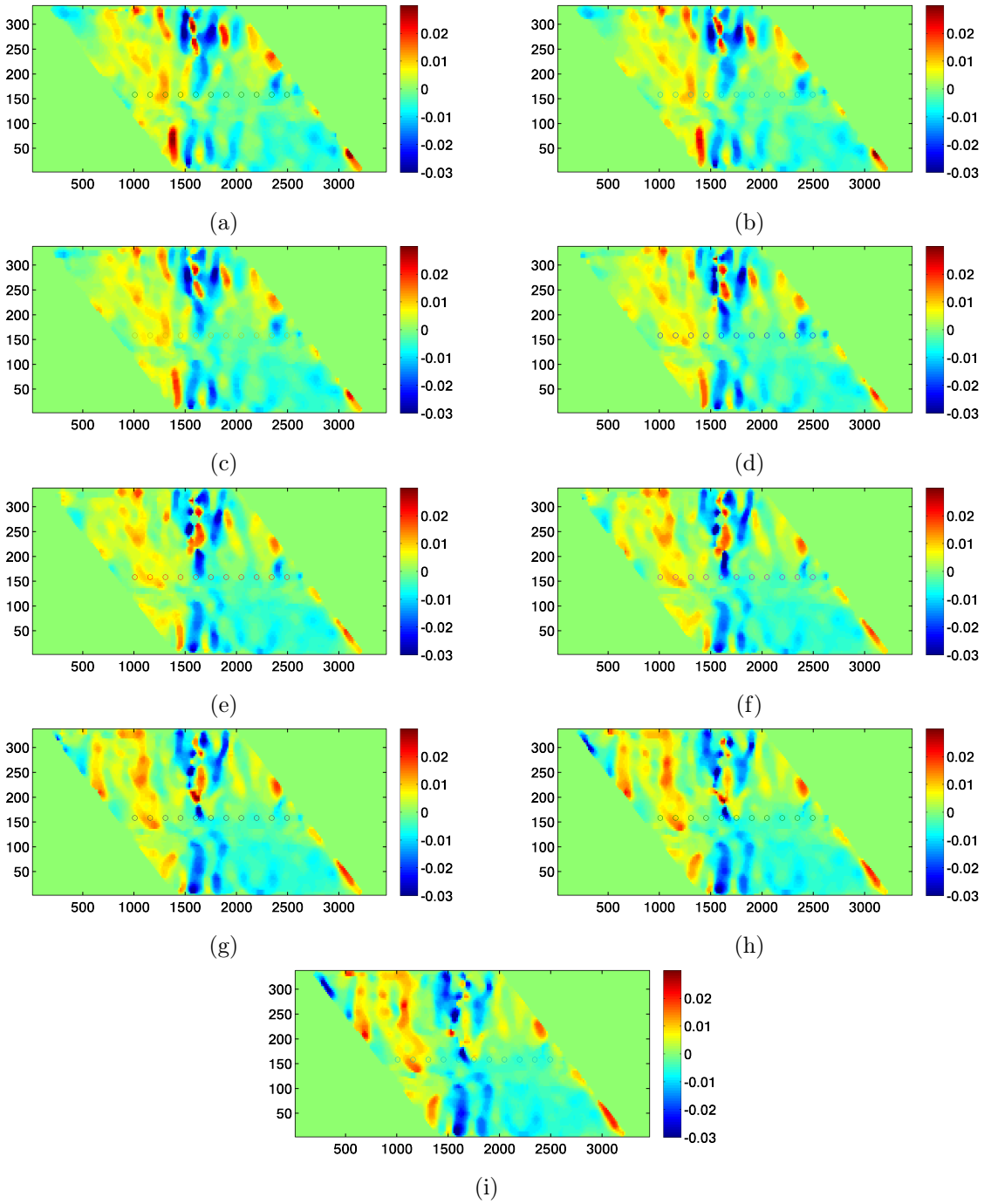

Figure 5.16: Crystal tilt δ_y correponding to the crystal plane rotation around the y axis, shown at different xz planes ($\partial\Phi/\partial x$).

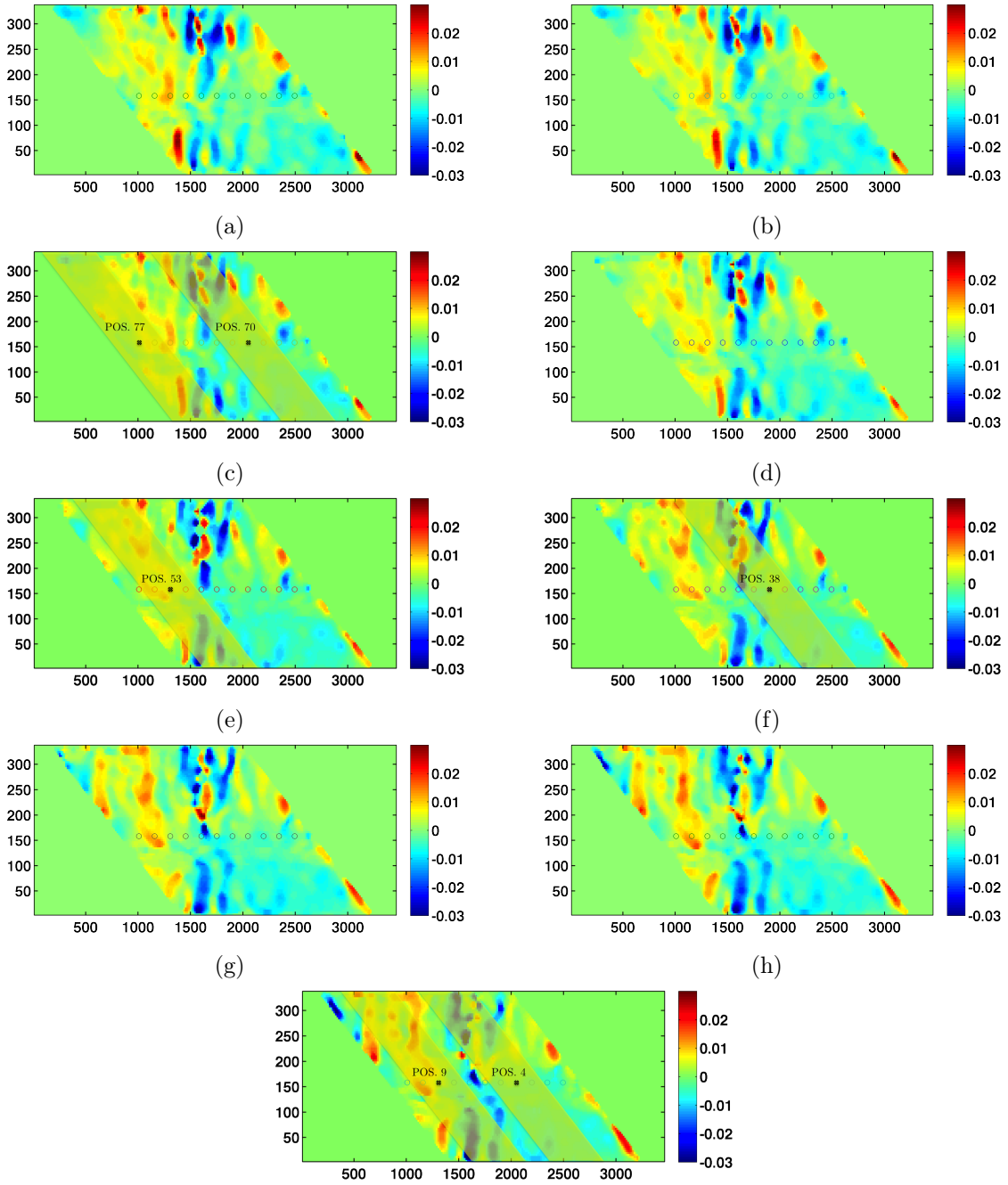

Figure 5.17: Crystal tilt δ_y correponding to the crystal plane rotation around the y axis, shown at different xz. The rectangles correspond to the diffracting volume which mainly contributes to the formation of the measured intensity patterns (at positions 4,9,38,53,70,77). The dots indicate the centers of the ptychography scan - beam positions.

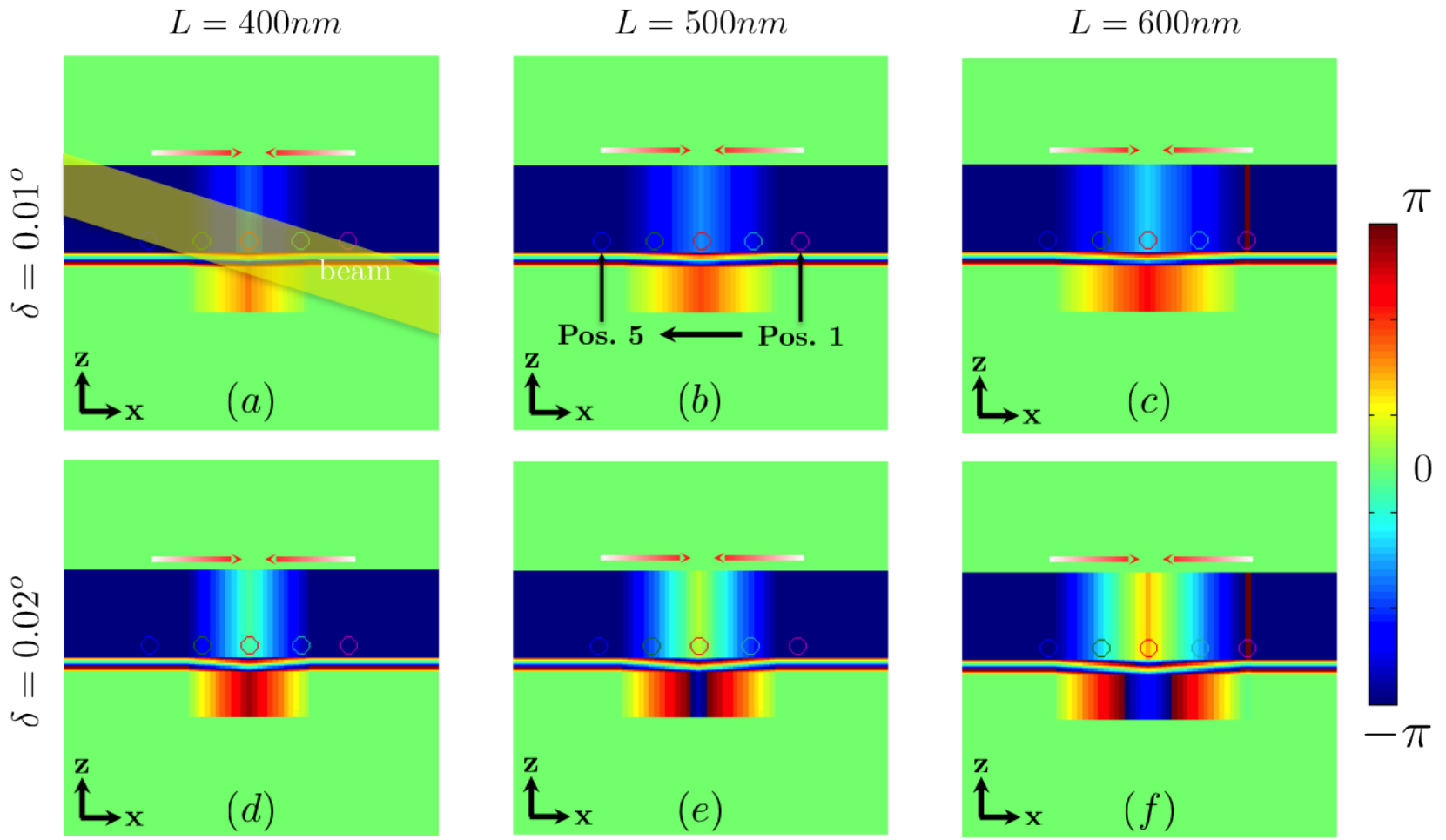

Figure 5.18: Phase profile resulting from the introduction of a local tilt in the numerical model of the nanstructured sample. The tilt extent and values are respectively noted L and δ. A series of 6 combinations was studied, for which the resulting diffraction patterns were calculated as a function of the beam-to-sample position (see Fig. 5.18).

5.3.2 The intensity patterns

The resulting diffraction patterns are presented in Fig. 5.19 for each structural configuration (tilt value, spatial extension and beam position) presented in Fig. 5.18. The intensity modifications induced by the presence of the tilts are evident: distortion and elongation of the Bragg peaks, shifts and/or splitting of the InGaAs peak along $\mathbf{q}_x$. Directly linking the phase behavior to the intensity distribution is not straightforward because the phase profile into the elongated illuminated volume is rather complex and because the whole intensity pattern is produced by the interferences between the fields arising from the InP and InGaAs layers. However one can conclude that a negative phase gradient produces a shift of the associated signal towards $q_x > 0$. The opposite behavior is observed for a positive phase gradient. This is especially verified in the case of the InGaAs peak, which has visibly moved down on the fifth position of the scan. When the illuminated volume includes regions of both negative and positive phase gradients, then the peak splitting is more pronounced, as evidenced for the fourth beam position.

When compared to the experimental data, we can see that this model reproduces some of the specific features experimentally observed while scanning the beam. For those regions, we can also observe that the retrieved phase field, presents strong similarities with the numerical model. All these indicate the compatibility of this hypothesis with the experimental observations. Note that the qualitative agreement between the simulated and experimental data, was achieved although we restricted the model to a minimum number of fitting parameters.

Reproducing the observed phase feature was important for deciphering the information that appears on the measured diffraction patterns. It verifies the claim for lattice tilts inside the thin film, but most of all, demonstrates the sensitivity of 3D Bragg ptychography to small crystalline rotations.

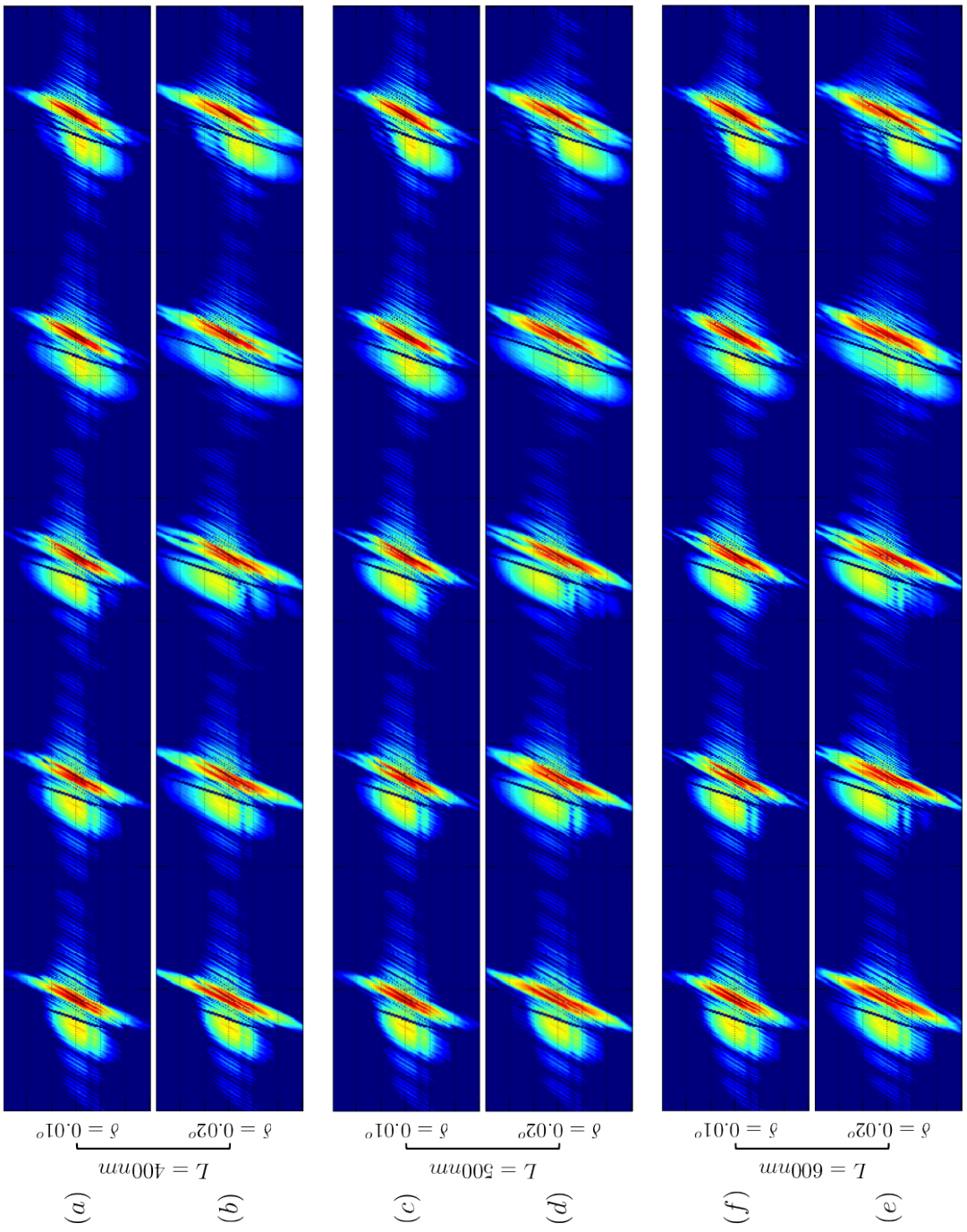

Figure 5.19: Simulated diffraction patterns corresponding to the six different configurations that produced the phase profile of Fig. 5.18.

5.4 Discussion, conclusion

The inversion of the Bragg ptychography data set has allowed to retrieve the crystalline properties of the InP stack. The obtained image shows the presence of the expected InGaAs embedded layer with a good accuracy (thickness, position, strain). However, additional structural features are observed in a locally restricted region of the retrieved volume. Those features agree well with the introduced physical model of local crystalline tilts, as shown with the numerical analysis above. However, the presence of those tilts was not confirmed by TEM investigation. Apart from the chemical fluctuations observed at the InP/Si interface, none of the structural inhomogeneities observed in the ptychographic data and reconstruction, were observed with electron microscopy.

However, if one wants to compare these two microscopy approaches, it is of major importance to have in mind their respective specificities. STEM provides crystal images with an extremely high spatial resolution, restricted to a field of view of about 0.1 μm. The sensitivity of the setup was estimated from the measurements (Fig. 5.20) with geometrical phase analysis [85, 96, 97] allowing to extract the r_{xz} rotation (around the y axis) and the ϵ_{zz} strain (along the z (001) direction). The presence of fluctuations on the images shown in Figs. 5.20b and c, allows to quantify the sensitivity to crystal rotations to about 0.5° and the accuracy on ϵ_{zz} to about $\pm 3 \times 10^{-3}$. On the contrary, our 3D Bragg ptychography reconstruction is extremely sensitive to the crystalline distortions (a lower bound of about 0.005° is estimated from Fig. 3.20d) and carries long length-scale information over a large volume (here about $2 \times 0.4 \times 0.34$ μm^3). Similar difficulties in comparing Bragg ptychography and electron microscopy results have been reported in Ref. [64].

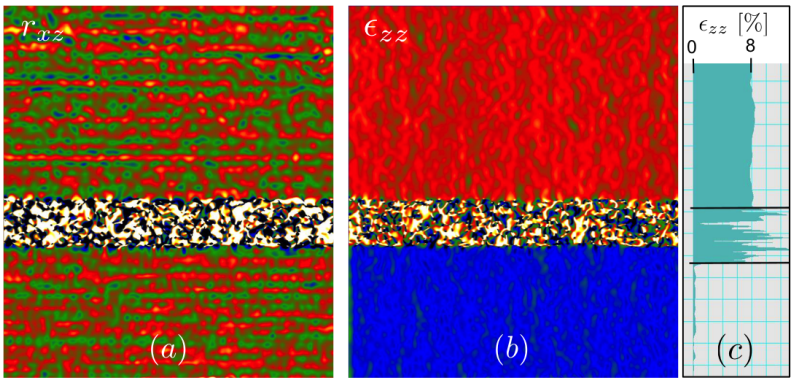

Figure 5.20: Quantifying STEM sensitivity. (a) HAADF mode view of the InP/Si interface. (b) Rotation r_{xz} and (c) strain ϵ_{zz} maps obtained from (a) using geometrical phase analysis. The color scale in (b) goes from $-0.5°$ to $+0.5°$, while in the inset of (c), the 1D cross section of ϵ_{zz} along z exhibits fluctuations of about ± 0.3 %.

Finally, we would like to underline that understanding the origin of the observed features is beyond the scope of this work. For sure, it is possible to address this question with additional analysis tools, such as finite element modeling, in order to calculate the displacement field according to the crystal elastic constants and test different structural conditions (inhomogeneous chemical composition or pressure during the bonding process, presence of dislocations *etc*). However, a deep understanding of the origin of the local tilts in the crystal thin film requires validating the proposed model with dedicated experiments. This is beyond the scope of this work.

Chapter 6

Conclusions and outlook

The goal of modern nanoscience for strain imaging of crystalline objects led to the development of X-ray Bragg CDI techniques, which computationally reconstruct the lost phase information from intensity-only measurements with the use of PRAs. The latest and one of the most promising imaging approaches, 3D X-ray Bragg ptychography, aims in becoming a routine X-ray imaging tool that can provide new insights to the investigation of crystals. Here we will summarize the contributions of this work in successfully realizing 3D Bragg ptychography and better understanding the particularities of thin film strain imaging, as well as testing the limits of the technique.

In Chapter 2 we presented the formalism of 3D strain imaging using the ptychographic approach, and developed the principles related to the forward problem and the inverse of the 3D ptychographic reconstruction of the crystal electron density by phase retrieval algorithms (OS, NCG). We discussed the *natural* and *laboratory* reference frames which we had to work with due to the particularity of the Bragg geometry, and saw the most recent developments in the field of Bragg ptychography until today.

In Chapter 3 we have presented the experimental needs of this work, like the sample design and X-ray experimental setup. We saw some of the properties of the InP/InGaAs crystal thin film and had a detailed look on the measured diffraction data from ID13 (evaluation of the data quality, experimental setup stability and investigation for radiation damage). The comparison of the post-fabrication HR-XRD with a laboratory source with the ptychographic dataset revealed the local inhomogeneities of the lattice structure, which were hidden behind the statistical measurements of HR-XRD. It showed the comparative advantages of nanodiffraction with a coherent light source in terms of probing materials at the nanoscale and with extreme sensitivity.

In Chapter 4 we developed a physical (and numerical) model for our system and described the physical process of measuring a 3D ptychographic dataset assembled by 2D Fraunhofer diffraction patterns in Bragg geometry. We saw that minimizing the data fidelity term is not a simple task for the PRA since the inversion results were unsatisfactory when starting the inversion with an initial estimate not close enough to the true object. The incorporation of regularization slightly improved the quality of the retrieved object, while the optimization of its parameters was empirically done. Nevertheless, even the addition of regularization was not sufficient for retrieving an image of good quality, and for this reason we had to work in developing a suitable initial guess by means of the MH constraint and finally reach a successful inversion scheme. We have shown that this strategy is robust enough and can significantly overcome the stagnation problems that are encountered when starting the inversion with an initial guess which is considerably *far away* from the true object.

The developed strategy for inverting the Bragg ptychography dataset has allowed retrieving the crystalline properties of the InP stack. The obtained image showed the presence of the expected InGaAs layer with good accuracy. Its thickness, position inside the slab and strain levels are in agreement in average with the nominal values. However, additional structural features are observed at a locally restricted region of the retrieved volume - also evidenced in the measured diffraction data. Those features agree well with the introduced modeling for local crystal tilts, as demonstrated with numerical analysis. However, apart from the chemical fluctuations observed at the InP/Si interface, none of the structural inhomogeneities observed during the ptychography experiments (data and reconstruction) were observed with TEM. The latter can be understood if considering the respective sensitivity and resolution of these two approaches. Furthermore it underlines the particularity of the 3D Bragg ptychography method.

Concerning the understanding of the observed features origin, it is possible to address this question with additional analysis tools such as finite element modeling. That would allow calculating the displacement field according the crystal elastic constants and test different structural conditions (inhomogeneous chemical composition or pressure during the bonding process, presence of dislocations in the wider area of the thin film *etc.*). However, a deep understanding of the origin of the local tilts in the crystal, requires at the end to validate the proposed model during dedicated experiments, something which was beyond the scope of this PhD project.

At this point, it is worth discussing some of the things that could be done in the future for improving the experimental conditions and the quality of the reconstruction, as well as, some of the potential opportunities for future research. In a ptychographic experiment in Bragg geometry, we often reach the limits of the developed beamline setups. The need for nanometer-accurate piezostages but most importantly the drifts or the small, negligible but inevitable misalignments with respect to the center of rotation, introduce and accumulate errors. The innovative approach of displacing the illumination instead of the sample [3] can be a potential way to considerably decrease the drifts during the experiment, and although the fact that the illumination profile will change at every scan position is not wishful, it is something that can be cured by additionally updating the probe [57, 88]. Even if that cannot be easily done due to experimental limitations, the positioning errors correction algorithms can be an alternative that has to be tested in the future [59]. In addition to that, an interesting method to enhance the resolution could be found in using randomly structured illuminations [98].

The need to perform rocking scans at every position, could in principle be substituted by using beams at different energies [99], and even if that is experimentally hard to achieve, the brand new approach of 3D Bragg Projection Ptychography [100] which can provide 3D images only from 2D acquisitions, could solve most of the stability issues currently encountered. Another problem that needs to be addressed is the fundamental limitation of the sample's thickness, as we have shown in Appendix A, which is imposed by the longitudinal coherence length of the illumination. Finally, there are always lots of things to be done concerning the algorithms for reducing the computational burden or accelerating the time-costly inversion strategies, like parallelization of the inversion processes or implementation of the existing codes in C++. In terms of theory as well, the field of numerical optimization will hopefully provide new heuristic approaches in the future.

Appendices

Appendix A

Coherence properties of third-generation synchrotron X-ray sources

The term of coherence refers to the degree of correlation between two waves. In order to quantify the coherence of a beam on a plane perpendicular to its propagation, we consider the horizontal and vertical *transverse* coherence length ($L_T = L_h, L_v$) [101]. It is defined as the lateral distance along a wavefront over which there is a complete dephasing between two waves of the same wavelength, which originate from two separate points in space. The visible outcome of the fact that the radiation source is not point-like but has some lateral extension (Δs), is the degradation of the interference fringes visibility.

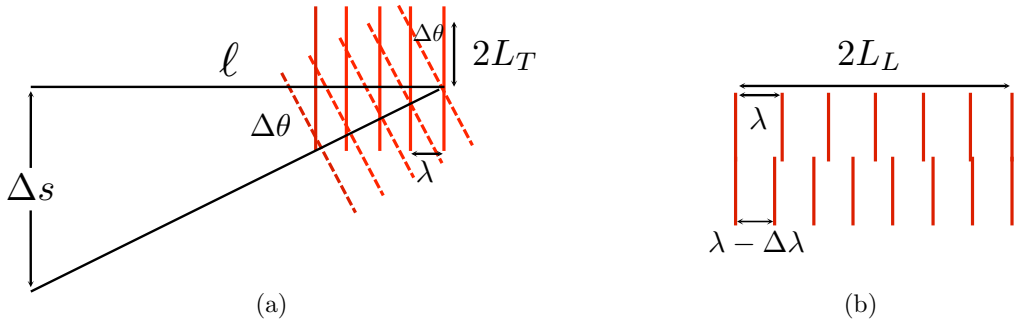

Figure A.1: (a) Transverse coherence length (L_T) (b) Longitudinal coherence length (L_L)

If we assume that two waves originate from points with a small angular separation $\Delta\theta$, ℓ the distance from the source and λ the radiation wavelength, then the transverse coherence lengths are given by:

$$\frac{\lambda}{2L_T} = \tan\Delta\theta, \qquad \frac{\Delta s}{\ell} = \tan\Delta\theta \qquad \Rightarrow \qquad L_T = \frac{\lambda\ell}{2\Delta s} \tag{A.0.1}$$

The degree of coherence of the radiation along its propagation direction, is described by the *longitudinal* coherence length [101]. It is defined as the distance over which two waves that simultaneously depart from the same source point with slightly different wavelengths will completely dephase [102]. It can be easily calculated by studying Figure A.1b

$$\begin{gathered} N\lambda = (N+1)(\lambda - \Delta\lambda) = N\lambda - N\Delta\lambda + \lambda - \Delta\lambda \\ \Rightarrow \lambda = (N+1)\Delta\lambda \Rightarrow \frac{\lambda}{\Delta\lambda} = N+1 \Rightarrow \frac{\lambda}{\Delta\lambda} = \frac{2L_L}{\lambda} + 1 \\ \Rightarrow L_L \approx \frac{\lambda^2}{2\Delta\lambda} \end{gathered} \tag{A.0.2}$$

Third generation synchrotron radiation sources produce highly coherent beams with typical transverse and longitudinal coherence lengths of several micrometers [103] (*e.g.* at the ESRF ID13 beam-line where the size opening of the slits is distance from the undulator is 92m, the working energy 14.9keV and the monochromaticity $\Delta E/E = 10^{-4}$, the coherence lengths are: $L_h = 60\mu m$,$L_v = 64\mu m$ and $L_L \approx 210nm$).

In particular in the case of Bragg geometry, the longitudinal coherence length has been shown to be limiting the maximum thickness s of a crystalline sample [104].

$$L_L \geqslant (PLD) \quad \Rightarrow \quad \frac{\lambda^2}{2\Delta\lambda} \geqslant 2s\sin\theta \quad \Rightarrow \quad s \leqslant \frac{1}{4\sin\theta}\frac{\lambda^2}{\Delta\lambda} \tag{A.0.3}$$

Thus for an angle of incidence of around 16^o, the maximum thickness of the sample is $\approx 370nm$.

Appendix B

Detection-space vs. direct-space in Bragg geometry

This appendix derives the relation between the *laboratory* DS coordinate systems and the *natural* DS coordinate system, relation that stems from the one that links their RS counterparts. Let $\boldsymbol{q}' = (q'_x, q'_y, q'_z)^t$ and $\boldsymbol{q} = (q_x, q_y, q_z)^t$ be two equivalent representations in $(\mathbf{q}'_x, \mathbf{q}'_y, \mathbf{q}'_z)$ and $(\mathbf{q}_x, \mathbf{q}_y, \mathbf{q}_z)$, respectively. Because the former system is orthonormal, we get

$$\mathbf{q} = \boldsymbol{B}\mathbf{q}', \quad \text{with} \quad \boldsymbol{B} \,\hat{=}\, \begin{pmatrix} | & | & | \\ \mathbf{q}'_x & \mathbf{q}'_y & \mathbf{q}'_z \\ | & | & | \end{pmatrix} \tag{B.0.1}$$

and we deduce from Fig. 2.4 that

$$\boldsymbol{B} \;=\; \begin{pmatrix} 1 & 0 & -\sin\theta_B \\ 0 & 1 & 0 \\ 0 & 0 & \cos\theta_B \end{pmatrix}. \tag{B.0.2}$$

As a result, the far-field reads equivalently

$$\Psi_j(\mathbf{q}) \;=\; \Psi_j(\boldsymbol{B}\mathbf{q}') \,\hat{=}\, \Psi'_j(\mathbf{q}')$$

and, by definition, the exit-field expressed in the *natural* DS system $(\mathbf{e}'_x, \mathbf{e}'_y, \mathbf{e}'_z)$ is

$$\psi'_j \hat{=} \mathcal{F}_{3D}^{-1}\, \Psi'_j \tag{B.0.3}$$

From this relation, we can write

$$\begin{aligned} \psi'_j(\mathbf{r}') \,\hat{=}\, & \int_{-\infty}^{+\infty} \Psi'_j(\mathbf{q}')\; e^{2\pi i\, \mathbf{q}'^t \mathbf{r}'} \mathrm{d}\mathbf{q}' \\ = \; & \int_{-\infty}^{+\infty} \Psi_j(\boldsymbol{B}\mathbf{q}')\; e^{2\pi i\, (\boldsymbol{B}^{-1}\mathbf{q})^t \mathbf{r}'} \mathrm{d}(\boldsymbol{B}^{-1}\mathbf{q}) \\ = \; & \int_{-\infty}^{+\infty} \Psi_j(\mathbf{q})\; e^{2\pi i \mathbf{q}^t (\boldsymbol{A}\mathbf{r}')} \mathrm{d}\mathbf{q} \times \frac{1}{\det(\boldsymbol{B})} \qquad \text{with} \quad \boldsymbol{A} \equiv (\boldsymbol{B}^{-1})^t \end{aligned}$$

which is related to the exit-field (in the DS laboratory system) ψ_j by[1]

$$\psi'_j(\mathbf{r}') \;=\; \psi_j(\boldsymbol{A}\mathbf{r}') \times \det(\boldsymbol{A}). \tag{B.0.4}$$

[1] Let us note that $\det(\boldsymbol{A}) \equiv \det(\boldsymbol{B}^{-1})^t = \det(\boldsymbol{B}^{-1}) = 1/\det(\boldsymbol{B})$.

Because we have $\psi_j \,\hat{=}\, p_j \times \rho$, the relation above also reads

$$\psi'_j(\mathbf{r}') \;=\; \big[p_j(\boldsymbol{A}\mathbf{r}') \times \det(\boldsymbol{A})\big] \times \rho(\boldsymbol{A}\mathbf{r}') \;\equiv\; p'_j(\mathbf{r}') \times \rho'(\mathbf{r}') \tag{B.0.5}$$

with

$$p'_j(\mathbf{r}') \,\hat{=}\, \det(\boldsymbol{A}) \times p_j(\mathbf{A}\boldsymbol{r}') \qquad \text{and} \qquad \rho'(\mathbf{r}') \,\hat{=}\, \rho(\mathbf{A}\boldsymbol{r}'). \tag{B.0.6}$$

Conversely, if we let

$$\mathbf{r} \;=\; \boldsymbol{A}\mathbf{r}' \quad\Leftrightarrow\quad \mathbf{r}' \;=\; \boldsymbol{A}^{-1}\mathbf{r} \tag{B.0.7}$$

the relation (B.0.4) above leads to

$$\psi_j(\mathbf{r}) \;=\; \psi'_j(\boldsymbol{A}^{-1}\mathbf{r}) \times \frac{1}{\det(\boldsymbol{A})}. \tag{B.0.8}$$

Eqn. (B.0.7) is the central relationship between the natural and laboratory DS systems[2] and the matrices $\boldsymbol{A}$ and $\boldsymbol{A}^{-1}$ are now explicitly given for the special case (B.0.2)

$$\boldsymbol{A} \;=\; \begin{pmatrix} 1 & 0 & 0 \\ 0 & 1 & 0 \\ \tan\theta_B & 0 & \frac{1}{\cos\theta_B} \end{pmatrix} \qquad \text{and} \qquad \boldsymbol{A}^{-1} \;=\; \begin{pmatrix} 1 & 0 & 0 \\ 0 & 1 & 0 \\ -\tan\theta_B \times \cos\theta_B & 0 & \cos\theta_B \end{pmatrix} \tag{B.0.9}$$

[2]For instance, these relations are used for the two interpolation steps that are discussed in Sec. 2.2.5: the relation $\mathbf{r}' \;=\; \boldsymbol{A}^{-1}\mathbf{r}$ is used for the computation of the probe function in the DS natural system, while $\mathbf{r} \;=\; \boldsymbol{A}\mathbf{r}'$ is used for the representation of the final estimate in the DS laboratory system.

Bibliography

[1] R. W. Gerchberg and W. O. Saxton, "A Practical Algorithm for the Determination of Phase from Image and Diffraction Plane Pictures," *Optik*, vol. 35, pp. 237–246, Nov. 1971.

[2] L. Feng, Z. J. Wong, R.-M. Ma, Y. Wang, and X. Zhang, "Single-mode laser by parity-time symmetry breaking," *Science*, vol. 346, pp. 968–972, Nov. 2014.

[3] S. O. Hruszkewycz, M. V. Holt, C. E. Murray, J. Bruley, J. Holt, A. Tripathi, O. G. Shpyrko, I. McNulty, M. J. Highland, and P. H. Fuoss, "Quantitative Nanoscale Imaging of Lattice Distortions in Epitaxial Semiconductor Heterostructures Using Nanofocused X-ray Bragg Projection Ptychography," *Nano Letters*, vol. 12, pp. 5148–5154, Oct. 2012.

[4] D. A. Muller, "Structure and bonding at the atomic scale by scanning transmission electron microscopy," *Nature Materials*, vol. 8, pp. 263–270, Apr. 2009.

[5] I. Robinson and R. Harder, "Coherent X-ray diffraction imaging of strain at the nanoscale," *Nature Materials*, vol. 8, pp. 291–298, Apr. 2009.

[6] H. Ade and H. Stoll, "Near-edge X-ray absorption fine-structure microscopy of organic and magnetic materials," *Nature Materials*, vol. 8, pp. 281–290, Apr. 2009.

[7] P. A. Midgley and R. E. Dunin-Borkowski, "Electron tomography and holography in materials science," *Nature Materials*, vol. 8, pp. 271–280, Apr. 2009.

[8] J. Nelson, X. Huang, J. Steinbrener, D. Shapiro, J. Kirz, S. Marchesini, A. M. Neiman, J. J. Turner, and C. Jacobsen, "High-resolution x-ray diffraction microscopy of specifically labeled yeast cells," *Proceedings of the National Academy of Sciences*, vol. 107, pp. 7235–7239, Apr. 2010.

[9] A. Talneau, C. Roblin, A. Itawi, O. Mauguin, L. Largeau, G. Beaudouin, I. Sagnes, G. Patriarche, C. Pang, and H. Benisty, "Atomic-plane-thick reconstruction across the interface during heteroepitaxial bonding of InP-clad quantum wells on silicon," *Applied Physics Letters*, vol. 102, no. 21, pp. 212101–4, 2013.

[10] B. E. Warren, *X-ray diffraction*. Dover Publications, 1990.

[11] F. P. Beer, E. R. Johnston, J. T. Dewolf, and D. F. Mazurek, *Mechanics of materials*. McGraw Hill, 2012.

[12] M. C. Newton, S. J. Leake, R. Harder, and I. K. Robinson, "Three-dimensional imaging of strain in a single ZnO nanorod," *Nature Materials*, vol. 9, pp. 120–124, feb 2010.

[13] M. Birkholz, *Thin Film Analysis by X-ray Scattering*. Wiley-VCH Verlag GmbH, 2006.

[14] J. E. M. Haverkort, B. H. P. Dorren, M. Kemerink, A. Y. Silov, and J. H. Wolter, "Design of composite InAsP/InGaAs quantum wells for a 1.55μm polarization independent semiconductor optical amplifier," *Applied Physics Letters*, vol. 75, pp. 2782–2784, Aug. 1999.

[15] J. Miao, P. Charalambous, J. Kitz, and D. Sayre, "Extending the methodology of X-ray crystallography to allow imaging of micrometre-sized non-crystalline specimens," *Nature*, vol. 400, pp. 1–3, July 1999.

[16] I. Robinson, I. Vartanyants, G. Williams, M. Pfeifer, and J. Pitney, "Reconstruction of the Shapes of Gold Nanocrystals Using Coherent X-Ray Diffraction," *Physical Review Letters*, vol. 87, pp. 195505–4, Oct. 2001.

[17] G. Williams, M. Pfeifer, I. Vartanyants, and I. Robinson, "Three-Dimensional Imaging of Microstructure in Au Nanocrystals," *Physical Review Letters*, vol. 90, pp. 175501–4, Apr. 2003.

[18] J. Stangl, C. Mocuta, V. Chamard, and D. Carbone, *Nanobeam X-Ray Scattering*. Wiley-VCH Verlag GmbH, 2014.

[19] H. A. Hauptman, "The phase problem of x-ray crystallography," *Rep. Prog. Phys.*, pp. 1427–1454, 1991.

[20] D. Sayre, "Some implications of a theorem due to Shannon," *Acta Crystallographica*, vol. 5, pp. 1–1, Nov. 1952.

[21] W. Hoppe and G. Strube, "Beugung in inhomogenen Primärstrahlenwellenfeld. II. Lichtoptische Analogieversuche zur Phasenmessung von Gitterinterferenzen," *Acta Crystallographica Section A*, vol. 25, pp. 502–507, Jul 1969.

[22] C. E. Shannon, "Communication in the presence of noise," *Proc. Institute of Radio Engineers*, vol. 37, pp. 10–21, Jan. 1949.

[23] V. Chamard, A. Diaz, J. Stangl, and S. Labat, "Structural investigation of InAs nanowires with coherent X-rays," *The Journal of Strain Analysis for Engineering Design*, vol. 44, pp. 533–542, Aug. 2009.

[24] J. Fienup, "Phase retrieval algorithms: a comparison," *Applied Optics*, vol. 21, pp. 2758–2769, Aug. 1982.

[25] J. Miao, T. Ishikawa, B. Johnson, E. Anderson, B. Lai, and K. Hodgson, "High Resolution 3D X-Ray Diffraction Microscopy," *Physical Review Letters*, vol. 89, pp. 088303–4, Aug. 2002.

[26] M. A. Pfeifer, G. J. Williams, I. A. Vartanyants, R. Harder, and I. K. Robinson, "Three-dimensional mapping of a deformation field inside a nanocrystal," *Nature*, vol. 442, pp. 63–66, July 2006.

[27] W. Yang, X. Huang, R. Harder, J. N. Clark, I. K. Robinson, and H.-k. Mao, "Coherent diffraction imaging of nanoscale strain evolution in a single crystal under high pressure," *Nature Communications*, vol. 4, pp. 1680–6, 1.

[28] A. Ulvestad, A. Singer, H.-M. Cho, J. N. Clark, R. Harder, J. Maser, Y. S. Meng, and O. G. Shpyrko, "Single Particle Nanomechanics in Operando Batteries via Lensless Strain Imaging," *Nano Letters*, vol. 14, no. 9, pp. 5123–5127, 0.

[29] J. N. Clark, L. Beitra, G. Xiong, A. Higginbotham, D. M. Fritz, H. T. Lemke, D. Zhu, M. Chollet, G. J. Williams, M. Messerschmidt, B. Abbey, R. J. Harder, A. M. Korsunsky, J. S. Wark, and I. K. Robinson, "Ultrafast Three-Dimensional Imaging of Lattice Dynamics in Individual Gold Nanocrystals," *Science*, vol. 341, pp. 56–59, July 2013.

[30] A. Minkevich, M. Gailhanou, J. S. Micha, B. Charlet, V. Chamard, and O. Thomas, "Inversion of the diffraction pattern from an inhomogeneously strained crystal using an iterative algorithm," *Physical Review B*, vol. 76, pp. 104106–5, Sept. 2007.

[31] A. A. Minkevich, M. Kohl, S. Escoubas, O. Thomas, and T. Baumbach, "Retrieval of the atomic displacements in the crystal from the coherent X-ray diffraction pattern," *J. Synchrotron Rad (2014). 21, 774-783 [doi:10.1107/S1600577514010108]*, pp. 1–10, June 2014.

[32] W. Cha, S. Song, N. C. Jeong, R. Harder, K. B. Yoon, I. K. Robinson, and H. Kim, "Exploration of crystal strains using coherent x-ray diffraction," *New Journal of Physics*, vol. 12, pp. 035022–10, Mar. 2010.

[33] A. Minkevich, T. Baumbach, M. Gailhanou, and O. Thomas, "Applicability of an iterative inversion algorithm to the diffraction patterns from inhomogeneously strained crystals," *Physical Review B*, vol. 78, pp. 174110–8, Nov. 2008.

[34] G. Strang, "Wavelets," *American Scientist*, vol. 82, p. 253, May-June 1994.

[35] A. Olivo and I. Robinson, "'Taking X-ray phase contrast imaging into mainstream applications' and its satellite workshop 'Real and reciprocal space X-ray imaging'," *Philosophical Transactions of the Royal Society A: Mathematical, Physical and Engineering Sciences*, vol. 372, pp. 20130359–20130359, Jan. 2014.

[36] S. Marchesini, H. N. Chapman, S. P. Hau-Riege, R. A. London, A. Szoke, H. He, M. R. Howells, H. Padmore, R. Rosen, J. C. H. Spence, and U. Weierstall, "Coherent X-ray diffractive imaging: applications and limitations," pp. 1–10, Sept. 2013.

[37] J. M. Rodenburg and R. H. T. Bates, "The theory of super-resolution electron microscopy via Wigner-distribution deconvolution," *Philosophical Transactions of the Royal Society A: Mathematical, Physical and Engineering Sciences*, vol. 339, pp. 521–553, 1992.

[38] H. Faulkner and J. Rodenburg, "Movable Aperture Lensless Transmission Microscopy: A Novel Phase Retrieval Algorithm," *Physical Review Letters*, vol. 93, pp. 023903–4, July 2004.

[39] P. Réfrégier, *Noise Theory and Application to Physics*. Springer, 2004.

[40] P. Godard, M. Allain, V. Chamard, and J. Rodenburg, "Noise models for low counting rate coherent diffraction imaging," *Optics Express*, pp. 1–21, Nov. 2012.

[41] J. Nocedal and S. J. Wright, *Numerical Optimization*. Springer, 1999.

[42] R. Fletcher and C. Reeves, "Function minimization by conjugate gradients," *Computer Journal*, no. 7, pp. 149–154, 1964.

[43] M. Dierolf, A. Menzel, P. Thibault, P. Schneider, C. M. Kewish, R. Wepf, O. Bunk, and F. Pfeiffer, "Ptychographic X-ray computed tomography at the nanoscale," *Nature*, vol. 467, pp. 436–439, Sept. 2010.

[44] P. Godard, G. Carbone, M. Allain, F. Mastropietro, G. Chen, L. Capello, A. Diaz, T. H. Metzger, J. Stangl, and V. Chamard, "Three-dimensional high-resolution quantitative microscopy of extended crystals," *Nature Communications*, vol. 2, pp. 568–6, 2011.

[45] P. J. McMahon, A. G. Peele, D. Paterson, K. A. Nugent, A. Snigirev, T. Weitkamp, and C. Rau, "X-ray tomographic imaging of the complex refractive index," *Applied Physics Letters*, vol. 83, no. 7, pp. 1480–4, 2003.

[46] R. Cierniak, *X-Ray Computed Tomography in Biomedical Engineering*. Springer, 2011.

[47] F. Natterer and F. Wübbeling, *Mathematical Methods in Image Reconstruction*. SIAM, Philadelphia, 2001.

[48] J. Jelínek, K. Segeth, and T. R. Overton, "Three-dimensional reconstruction from projections," *Aplikace matematiky*, vol. 30, pp. 92–109, 1985.

[49] A. C. Kak and M. Slaney, *Principles of Computerized Tomographic Imaging*. IEEE Press, 1988.

[50] V. Elser, "Phase retrieval by iterated projections," *Journal of the Optical Society of America A*, vol. 20, pp. 40–55, Jan. 2003.

[51] H. M. Quiney, A. G. Peele, Z. Cai, D. Paterson, and K. A. Nugent, "Diffractive imaging of highly focused X-ray fields," *Nature Physics*, vol. 2, pp. 101–104, Jan. 2006.

[52] F. Mastropietro, D. Carbone, A. Diaz, J. Eymery, A. Sentenac, T. H. Metzger, V. Chamard, and V. Favre-Nicolin, "Coherent x-ray wavefront reconstruction of a partially illuminated Fresnel zone plate," *Optics Express*, vol. 19, pp. 19223–19232, June 2011.

[53] S. Hönig, R. Hoppe, J. Patommel, A. Schropp, S. Stephan, S. Schöder, M. Burghammer, and C. G. Schroer, "Full optical characterization of coherent x-ray nanobeams by ptychographic imaging.," *Optics Express*, vol. 19, pp. 16324–16329, Aug. 2011.

[54] J. M. Rodenburg and H. M. L. Faulkner, "A phase retrieval algorithm for shifting illumination," *Applied Physics Letters*, vol. 85, no. 20, pp. 4795–3, 2004.

[55] J. Rodenburg, A. Hurst, A. Cullis, B. Dobson, F. Pfeiffer, O. Bunk, C. David, K. Jefimovs, and I. Johnson, "Hard-X-Ray Lensless Imaging of Extended Objects," *Physical Review Letters*, vol. 98, pp. 034801–4, Jan. 2007.

[56] J. M. Rodenburg, A. C. Hurst, and A. G. Cullis, "Transmission microscopy without lenses for objects of unlimited size," *Ultramicroscopy*, vol. 107, pp. 227–231, Feb. 2007.

[57] P. Thibault, M. Dierolf, A. Menzel, O. Bunk, C. David, and F. Pfeiffer, "High-Resolution Scanning X-ray Diffraction Microscopy," *Science*, vol. 321, pp. 379–382, July 2008.

[58] P. Thibault, M. Dierolf, O. Bunk, A. Menzel, and F. Pfeiffer, "Probe retrieval in ptychographic coherent diffractive imaging," *Ultramicroscopy*, vol. 109, pp. 338–343, Mar. 2009.

[59] A. M. Maiden, M. J. Humphry, M. C. Sarahan, B. Kraus, and J. M. Rodenburg, "An annealing algorithm to correct positioning errors in ptychography," *Ultramicroscopy*, vol. 120, pp. 64–72, Sept. 2012.

[60] F. Zhang, I. Peterson, J. Vila-Comamala, A. Diaz, F. Berenguer, R. Bean, B. Chen, A. Menzel, I. K. Robinson, and J. M. Rodenburg, "Translation position determination in ptychographic coherent diffraction imaging," *Optics Express*, vol. 21, no. 11, pp. 13592–15, 2013.

[61] P. Godard, M. Allain, and V. Chamard, "Imaging of highly inhomogeneous strain field in nanocrystals using x-ray Bragg ptychography: A numerical study," *Physical Review B*, vol. 84, pp. 144109–11, Oct. 2011.

[62] F. Berenguer, P. Godard, M. Allain, J. M. Belloir, A. Talneau, S. Ravy, and V. Chamard, "X-ray lensless microscopy from undersampled diffraction intensities," *Physical Review B*, vol. 88, pp. 144101–6, Oct. 2013.

[63] M. Dierolf, P. Thibault, A. Menzel, C. M. Kewish, K. Jefimovs, I. Schlichting, K. v. König, O. Bunk, and F. Pfeiffer, "Ptychographic coherent diffractive imaging of weakly scattering specimens," *New Journal of Physics*, vol. 12, pp. 035017–14, Mar. 2010.

[64] V. Chamard, M. Allain, P. Godard, A. Talneau, G. Patriarche, and M. Burghammer, "Strain in a silicon-on-insulator nanostructure revealed by 3D x-ray Bragg ptychography," *Scientific Reports*, vol. 5, pp. 9827–8, May 2015.

[65] Y. Takahashi, A. Suzuki, S. Furutaku, K. Yamauchi, Y. Kohmura, and T. Ishikawa, "Bragg x-ray ptychography of a silicon crystal: Visualization of the dislocation strain field and the production of a vortex beam," *Physical Review B*, vol. 87, pp. 121201–4, Mar. 2013.

[66] V. R. Almeida, C. A. Barrios, R. R. Panepucci, and M. Lipson, "All-optical control of light on a silicon chip," *Nature*, vol. 431, pp. 1081–1084, Oct. 2004.

[67] J. L. Pan, J. E. McManis, T. Osadchy, L. Grober, J. M. Woodall, and P. J. Kindlmann, "Gallium arsenide deep-level optical emitter for fibre optics," *Nature Materials*, vol. 2, pp. 375–378, May 2003.

[68] D. Liang and J. E. Bowers, "Recent progress in lasers on silicon," *Nature Publishing Group*, vol. 4, pp. 511–517, July 2010.

[69] H. Kawanami, "Heteroepitaxial technologies of iii-v on si," *Solar Energy Materials Solar Cells*, vol. 66, pp. 479–486, 2001.

[70] Y. H. Xie, K. L. Wang, and Y. C. Kao, "An investigation on surface conditions for si molecular beam epitaxial (mbe) growth.," *J. Vac. Sci. Tech. A*, vol. 3, pp. 1035–1039, 1985.

[71] K. e. a. Samonji, "Reduction of threading dislocation density in inp-on-si heteroepitaxy with strained short-period superlattices.," *Appl. Phys. Lett.*, vol. 69, pp. 100–102, 1996.

[72] Y. Masafumi, S. Mitsuru, and I. Yoshio, "Misfit stress dependence of dislocation density reduction in gaas films on si substrates grown by strained-layer superlattices.," *Appl. Phys. Lett.*, vol. 54, pp. 256–2570, 1989.

[73] K. Nozawa and Y. Horikoshi, "Low threading dislocation density gaas on si(100) with ingaas/gaas strained-layer superlattice grown by migration-enhanced epitaxy.," *Jpn. J. Appl. Phys.*, vol. 30, pp. 668–671, 1991.

[74] E. Yamaichi, T. Ueda, Q. Gao, C. Yamagishi, and M. Akiyama, "Method to obtain low-dislocation-density regions by patterning with sio_2 on gaas/si followed by annealing.," *Jpn. J. Appl. Phys.*, vol. 33, pp. 1442–1444, 1994.

[75] M. E. Groenert, A. J. Pitera, R. J. Ram, and E. A. Fitzgerald, "Improved room-temperature continuous wave gaas/algaas and ingaas/gaas/algaas lasers fabricated on si substrates via relaxed graded ge_xsi_{1-x} buffer layers.," *J. Vac. Sci. Tech. B*, vol. 21, pp. 1064–1069, 2003.

[76] L. Cerutti, J. B. Rodriguez, and E. Tournie, "Gasb-based laser monolithically grown on silicon substrate emitting at 1.55μm at room temperature.," *IEEE Photon. Tech. Lett.*, vol. 22, pp. 553–555, 2010.

[77] A. W. Fang, H. Park, Y.-H. Kuo, R. Jones, O. Cohen, D. Liang, O. Raday, M. N. Sysak, M. J. Paniccia, and J. E. Bowers, "Hybrid silicon evanescent devices," *Materials Today*, vol. 10, pp. 1–8, June 2007.

[78] K. Tanabe, K. Watanabe, and Y. Arakawa, "III-V/Si hybrid photonic devices by direct fusion bonding," *Scientific Reports*, vol. 2, pp. 1–6, Apr. 2012.

[79] J. Bowers, D. Liang, A. Fang, H. Park, R. Jones, and M. Paniccia, "Hybrid silicon lasers: the final frontier to integrated computing.," *Optics & Photonics News*, pp. 21–23, 2010.

[80] S. Adachi, *Properties of Group-IV, III-V and II-VI Semiconductors*. John Wiley & Sons, Ltd, 2005.

[81] H. Park, A. W. Fang, D. Liang, Y.-H. Kuo, H.-H. Chang, B. R. Koch, H.-W. Chen, M. N. Sysak, R. Jones, and J. E. Bowers, "Photonic Integration on the Hybrid Silicon Evanescent Device Platform," *Advances in Optical Technologies*, vol. 2008, pp. 1–17, 2008.

[82] A. Itawi, K. Pantzas, I. Sagnes, G. Patriarche, and A. Talneau, "Void-free direct bonding of inp to si: Advantages of low h-content and ozone activation," *Journal of Vacuum Science & Technology B*, vol. 32, no. 2, 2014.

[83] M. Born, "Quantenmechanik der stossvorgänge," *Zeitschrift für Physik*, vol. 38, no. 803, 1926.

[84] S. Blügek, *Scattering Theory: Born Series*. Lectures of the IFF Spring School 2012 "Scattering Methods for Condensed Matter Research: Towards Novel Applications at Future Sources", 2012.

[85] M. J. Hytch, E. Snoeck, and R. Kilaas, "Quantitative measurement of displacement and strain fields from hrem micrographs.," *Ultramicroscopy*, vol. 74, pp. 131–146, 1998.

[86] C. Riekel, M. Burghammer, and R. Davies, "Progress in micro- and nano-diffraction at the ESRF ID13 beamline," *IOP Conference Series: Materials Science and Engineering*, vol. 14, pp. 012013–10, Dec. 2010.

[87] C. Ponchut, J. M. Rigal, J. Clément, E. Papillon, A. Homs, and S. Petitdemange, "MAXIPIX, a fast readout photon-counting X-ray area detector for synchrotron applications," *Journal of Instrumentation*, vol. 6, pp. C01069–C01069, Jan. 2011.

[88] A. M. Maiden and J. M. Rodenburg, "An improved ptychographical phase retrieval algorithm for diffractive imaging," *Ultramicroscopy*, vol. 109, pp. 1256–1262, Sept. 2009.

[89] J. Fienup and C. Wackerman, "Phase-retrieval stagnation problems and solutions," *J. Opt. Soc. Am. A*, vol. 3, no. 11, pp. 1897–1907, 1986.

[90] S. Marchesini, H. He, H. N. Chapman, S. P. Hau-Riege, A. Noy, M. R. Howells, U. Weierstall, and J. C. H. Spence, "X-ray image reconstruction from a diffraction pattern alone," *Physical Review B*, vol. 68, pp. 140101–4, Oct. 2003.

[91] P. Thibault and M. Guizar-Sicairos, "Maximum-likelihood refinement for coherent diffractive imaging," *New Journal of Physics*, vol. 14, pp. 063004–20, June 2012.

[92] G. Demoment *IEEE T. Acoust. Speech*, vol. 37, no. 2024, 1989.

[93] P. C. Hansen and D. P. OLeary, "The use of the L-curve in the regularization of discrete ill-posed problems," *SIAM Journal of Scientific Computing*, vol. 14, pp. 1487–1503, Nov. 1993.

[94] M. Allain and J. P. Roques, "Imaging techniques for gamma-ray diffuse emission: application to INTEGRAL/SPI," *Astronomy and Astrophysics*, vol. 447, pp. 1175–1187, Mar. 2006.

[95] M. A. Herráez, D. R. Burton, M. J. Lalor, and M. A. Gdeisat, "Fast two-dimensional phase-unwrapping algorithm based on sorting by reliability followinga noncontinuous path," *Applied Optics*, vol. 41, pp. 7437–7444, Nov. 2002.

[96] J. L. Rouvière and E. Sarigiannidou, "Theoretical discussions on the geometrical phase analysis," *Ultramicroscopy*, vol. 106, pp. 1–17, Dec. 2005.

[97] J. Chung and L. Rabenberg, "Effects of strain gradients on strain measurements using geometrical phase analysis in the transmission electron microscope," *Ultramicroscopy*, vol. 108, pp. 1595–1602, Nov. 2008.

[98] E. Mudry, K. Belkebir, J. Girard, J. Savatier, E. Le Moal, C. Nicoletti, M. Allain, and A. Sentenac, "Structured illumination microscopy using unknown speckle patterns," *Nature Photonics*, vol. 6, pp. 312–315, Apr. 2012.

[99] V. Favre-Nicolin, S. Bos, J. E. Lorenzo, P. Bordet, W. Shepard, and J.-L. Hodeau, "Integration procedure for the quantitative analysis of dispersive anomalous diffraction," *Journal of Applied Crystallography*, vol. 33, pp. 52–63, Feb 2000.

[100] S. O. Hruszkewycz, M. Allain, M. V. Holt, C. E. Murray, J. R. Holt, P. H. Fuoss, and V. Chamard, "High resolution three dimensional structural microscopy by single angle Bragg ptychography," *arXiv*, pp. 1–16, June 2015.

[101] G. Xiong, O. Moutanabbir, M. Reiche, R. Harder, and I. Robinson, "Coherent X-Ray Diffraction Imaging and Characterization of Strain in Silicon-on-Insulator Nanostructures," *Advanced Materials*, vol. 26, pp. 7747–7763, June 2014.

[102] F. v. d. Veen and F. Pfeiffer, "Coherent x-ray scattering," *Journal of Physics: Condensed Matter*, vol. 16, pp. 5003–5030, July 2004.

[103] A. Singer and I. A. Vartanyants, "Coherence properties of focused X-ray beams at high-brilliance synchrotron sources," *Journal of Synchrotron Radiation*, vol. 21, pp. 5–15, 2014.

[104] S. J. Leake, M. C. Newton, R. Harder, and I. K. Robinson, "Longitudinal coherence function in X-ray imaging of crystals," *Optics Express*, vol. 17, pp. 15853–15859, Aug. 2009.